

**UNIVERSITA' DEGLI STUDI DI PARMA**

**Dottorato di ricerca in Scienza e Tecnologia dei Materiali  
Innovativi**

**Ciclo XXVIII (2013-2015)**

**Self-standing curved crystals for X and Gamma  
ray focusing**

**Coordinatore:  
Prof. Enrico Dalcanale**

**Tutor:  
Dott. Claudio Ferrari  
Dott.ssa Elisa Buffagni**

**Dottorando: Elisa Bonnini**

**2016**



# Contents

|  |           |
|--|-----------|
| <b>Introduction</b>  | <b>1</b>  |
| <b>1 Laue Lens Concept</b>   | <b>5</b>  |
| 1.1 Astronomical application . . . . .   | 7         |
| 1.2 Medical application . . . . .  | 9         |
| <b>2 Diffraction of X and <math>\gamma</math> ray from crystals</b>                            | <b>13</b> |
| 2.1 Fundamentals of crystallography . . . . .  | 13        |
| 2.1.1 Crystalline structure . . . . .  | 13        |
| 2.1.2 Reciprocal lattice . . . . .   | 15        |
| 2.1.3 Diffraction condition: Bragg and Laue relation . . . . .                                 | 16        |
| 2.1.4 Ewald construction . . . . .   | 18        |
| 2.1.5 Geometries of diffraction . . . . .  | 19        |
| 2.2 Diffraction from ideal crystal . . . . .   | 19        |
| 2.2.1 Thomson scattering from a free electron . . . . .  | 19        |
| 2.2.2 Scattering from an atom . . . . .  | 21        |
| 2.2.3 Diffracted intensity from a small single crystal . . . . .                               | 23        |
| 2.2.3.1 Integrated intensity from small single crystal . . . . .                               | 24        |
| 2.2.4 Limitations and corrections to the kinematical theory:<br>the dynamical theory . . . . . | 25        |
| 2.2.5 The dispersion surface . . . . .   | 26        |
| 2.2.5.1 Qualitative approach to the dynamical theory . . . . .                                 | 27        |
| 2.2.6 Integrated Intensity and reflectivity in Laue case in dy-<br>namical theory . . . . .    | 30        |
| 2.2.7 Borrmann effect . . . . .  | 35        |
| 2.2.7.1 Polarization influence . . . . .   | 35        |
| 2.3 Diffraction from mosaic crystal . . . . .  | 36        |
| 2.3.1 Darwin model . . . . .   | 36        |
| 2.4 Diffraction from crystal with curved diffracting planes . . . . .                          | 38        |

|          |  |            |
|----------|--|------------|
| <b>3</b> | <b>Diffraction efficiency of bent crystals: theoretical study</b>          | <b>43</b>  |
| 3.1      | Diffraction efficiency . . . . .   | 44         |
| 3.1.1    | Approximated calculation of integrated intensity: Lamellar model . . . . . | 45         |
| 3.1.2    | Crystal's material . . . . .   | 46         |
| 3.1.3    | Effect of crystal's thickness . . . . .                                    | 46         |
| 3.1.4    | Radius of curvature . . . . .  | 49         |
| 3.2      | Conclusion . . . . .   | 50         |
| <b>4</b> | <b>Bending technique</b>   | <b>53</b>  |
| 4.1      | Damaging technique . . . . .   | 54         |
| 4.2      | Resin deposition technique . . . . .                                       | 56         |
| 4.3      | Conclusion . . . . .   | 60         |
| <b>5</b> | <b>Experimental results</b>  | <b>65</b>  |
| 5.1      | Low energy . . . . .   | 65         |
| 5.1.1    | Preparation of thicker diffracting elements . . . . .                      | 70         |
| 5.2      | High energy . . . . .  | 73         |
| 5.3      | Conclusion . . . . .   | 75         |
| <b>6</b> | <b>LAUE Project</b>  | <b>79</b>  |
| 6.1      | Crystal selection . . . . .  | 80         |
| 6.2      | The Larix facilities . . . . .   | 82         |
| 6.2.1    | Alignment of the facility . . . . .  | 86         |
| 6.3      | Focusing effect . . . . .  | 88         |
| 6.4      | Conclusion . . . . .   | 92         |
|          | <b>Conclusions</b>   | <b>99</b>  |
| <b>A</b> | <b>Calculation of the inner lattice plane bending in bent crystals</b>     | <b>101</b> |
| <b>B</b> | <b>Origin of strain in surface damaged bent crystals</b>                   | <b>105</b> |
| B.1      | Line tension characterization . . . . .                                    | 105        |
| B.2      | Model of strain formation in surface treated crystals . . . . .            | 107        |
| B.3      | Mechanism of dislocation formation . . . . .                               | 108        |
| <b>C</b> | <b>Experimental set up</b>   | <b>111</b> |
| C.1      | ANKA Synchrotron radiation facility . . . . .                              | 111        |
| C.2      | Hard X ray Facility, ILL . . . . .   | 113        |

# Introduction

The focusing of hard X and  $\gamma$  rays in the energy range between 60 and 600 keV has important applications in astronomy to improve the sensitivity of telescopes (Frontera et al., 2005) and in nuclear medicine for in vivo diagnosis of diseases associated with organ malfunctioning, for cancer detection (Roa et al., 2005) and for focussed radiotherapy. A clear example is given by the case of scintigraphic monitoring, in which target images are currently obtained by collecting monochromatic  $\gamma$  radiation coming from specific radiopharmaceuticals, selected in the emission energy range from 80 keV (Xenon-133) to 511 keV (Fluorine-18), by means of gamma cameras based on fine multi-hole collimators and scintillators. A major drawback in such systems is the high dose distributed to the body because most of the radiation is lost by collimator absorption.

Bragg diffraction in Laue geometry is a method to focus high energy X and  $\gamma$  rays. This is the goal of a Laue lens, which is composed of a set of crystals disposed in concentric rings and properly oriented in order to concentrate the diffracted beams into a small focal point on the detector (see Chap. 1).

Crystals suitable for such a lens should be able to efficiently diffract the radiation in an angular range from a few tens of arc seconds up to some minutes of arcseconds, depending on the required lens resolution. Perfect crystals cannot be used due to their very narrow angular range of diffraction at  $\gamma$  ray energies. Instead, mosaic crystals are good candidates as optical elements for these lenses, because their angular acceptance can be directly tuned by modifying the mosaic spread and/or the size of microcrystals forming the mosaic structure during the growth process. Mosaic crystals of high diffraction efficiency at  $\gamma$  ray energies, such as Cu, Au, Ag and many others, have been proposed (Lund, 1992; Courtois et al., 2005; Barriere et al., 2009) due to their high electronic density and structure factor. Moreover, the integrated intensity  $I_{\text{int}}$  (defined as the area of the diffraction profile for a monochromatic radiation, which gives directly an indication of the diffraction efficiency of the crystal) of an ideal mosaic crystal can be two orders of magnitude larger than that of a perfect crystal, as predicted by the dynamical theory of X ray diffraction (Authier, 1998). Unfortunately the production of crystals with well-defined mosaic spread and grain size is a difficult technological task, so that the resulting diffracted intensity is often

much lower than that predicted for the ideal case. Mosaic crystals of high diffraction efficiency at  $\gamma$  ray energies, such as Cu, Au, Ag and many others, have been proposed (Lund, 1992; Courtois et al., 2005; Barriere et al., 2009) due to their high electronic density and structure factor.

An effective alternative is represented by self-standing bent crystals, in which the external curvature induces also a bending of the diffracting planes. In this case the Bragg condition is satisfied for a broad angular range according to the degree of curvature; this also causes the high angular acceptance of these crystals (Smither et al., 2005). If the curvature radius  $R$  is smaller than a critical value resulting from dynamical theory, curved diffracting plane (CDP) crystals can theoretically reach the  $I_{\text{int}}$  values obtained for ideal mosaic crystals (Malgrange, 2002).

In this thesis a theoretical study of the  $I_{\text{int}}$  of CDP crystals is presented in Chap. 3, based on dynamical theory of X and  $\gamma$  ray diffraction, described in Chap. 2. The theoretical study point out what are the best material and values for parameters, such as thickness, curvature, dimensions, and diffraction geometry to maximize the diffraction efficiency of curved crystals in the energy range of interest.

In Chap. 4, two different simple methods to obtain self-standing curved crystals with reproducible and uniform curvature are presented. The first one is based on the controlled surface damaging induced by a mechanical lapping process (Buffagni et al., 2011). A compressive strained layer of few micrometres in thickness is generated and causes the convex curvature of the damaged side of the crystal (Buffagni et al., 2012; Buffagni et al., 2013). This technique allows to obtain external radii of curvature  $R$  down to 2 m in crystals with thickness up to 2 mm in the direction perpendicular to the damaged surface. The diffraction profile of CDPs, parallel to the damaged surface, is close to that of an ideal bent crystal curved by elastic deformation (Ferrari et al., 2014).

Another innovative and simple bending technique presented for the first time in this work is based on the shrinking of resins during a polymerization process, as it is well known in wood and mechanical industry. The process consists on a film deposition of selected bi-component epoxy resin on one side of crystals with thickness uniformity guaranteed by means of a spin-coater. During the polymerization, the resin induces a tensile strain that causes the bending of the substrate, with concave curvature on the side of the resin deposition.

In order to verify the theoretical results obtained about the crystal diffraction efficiency, detailed characterizations at low and high X ray energies are performed on flat and bent crystals obtained with the damaging and the resin deposition techniques, Chap. 5. Thanks to the access to the European facilities, as ILL and ANKA synchrotron, it was possible to perform a quantitative study of the diffraction efficiency of crystals with different thickness at different geometries, in the energy range of interest.

To complete this work, the study of the focusing effect of GaAs curved crystals realized with the damaging technique are shown in Chap. 6. The contest is a project founded by the Italian Space Agency (ASI), called **LAUE project**, that was devoted to create a technology to build a Laue lens with long focal length ( $f = 20$  m) able to focus photons in the  $70 \div 300$  keV energy range. The lens is assumed to be made of petals constituted by a large number of crystals tiles disposed in concentric rings and properly oriented in order to diffract an incident beam parallel to the lens axis in the focal point of the lens. In this case, curved crystals are directly used as focusing optical elements.





# Chapter 1

## Laue Lens Concept

Diffraction lenses are based on the interference between the X and  $\gamma$  radiation and the periodic structure of matter in a crystal. In a Laue lens, an incoming beam with wavelength  $\lambda$ , passing through the whole volume of crystals, can be diffracted if it satisfies the Bragg condition (see sec. 2 ),

$$2d_{hkl} \sin \theta = n\lambda \quad (1.0.1)$$

With  $d_{hkl}$  the spacing of a chosen set of planes ( $hkl$ ). The Bragg condition can occur in two different geometries (reflection and transmission), illustrated in Figure 1.0.1 and explained in detail in sec (2.1.3).

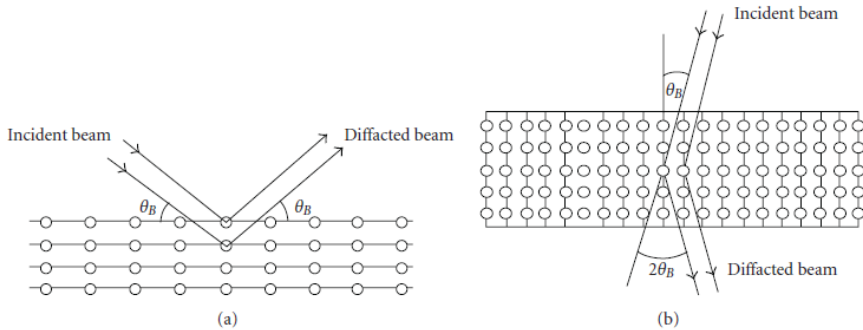


Figure 1.0.1: The Bragg condition for constructive interference of an X and  $\gamma$  ray with the atoms of a given crystalline plane. (a) Bragg diffraction in reflection configuration (Bragg geometry). (b) Bragg diffraction in transmission configuration (Laue geometry), (Frontera and von Ballmoos, 2010)

A Laue lens is made of a large number of crystals disposed in concentric rings (Figure 1.0.2 *Left*) properly oriented in order to diffract, in Laue geometry, the incident radiation into a common focal point (see Figure 1.0.2 *Right*). The lens has a shape of a spherical cup, with a radius of curvature  $R$ , covered with

crystal tiles having their diffracting planes perpendicular to the surface of the sphere. The focal spot falls on the detector placed on the lens axis at a distance  $f = R/2$  from the cup, where  $f$  is called the *focal length*.

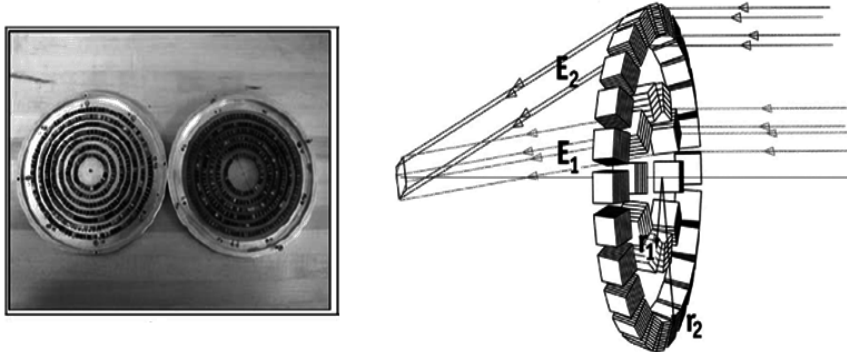


Figure 1.0.2: *Left*: Scheme of the disposition of crystals in concentric rings on a Laue lens. *Right*: Concentric rings at a given ring  $r$  concentrate a defined energy  $E$  into the focal point (Frontera and von Ballmoos, 2010).

Considering the Bragg equation 1.0.1, for the first diffraction order ( $n = 1$ ); the energy  $E$  of an incident beam diffracted by a set of crystals disposed in a ring at distance  $r$  ( $r_{min} \leq r \leq r_{max}$ ) from the lens axis, is:

$$E = \frac{hc}{2d_{hkl} \sin \left[ \frac{1}{2} \arctan \left( \frac{f}{r} \right) \right]} \approx \frac{hcf}{d_{hkl}r} \quad (1.0.2)$$

Assuming that chosen diffracting planes ( $hkl$ ) of all the crystals that compose the lens are the same; the energy of the photons diffracted from all the crystals in the ring will be centered on  $E$ . A Laue lens can diffract photons over a certain energy passband ( $E_{min}, E_{max}$ ):

$$\begin{cases} E_{min} \approx \frac{hcf}{d_{hkl}r_{max}} \\ E_{max} \approx \frac{hcf}{d_{hkl}r_{min}} \end{cases} \quad (1.0.3)$$

The energy passbands of the diffracted photons by contiguous crystal rings have to overlap each other in the focal point.

Suitable crystals must be selected as optical elements for a Laue lens. The angular acceptance  $\alpha$  of a perfect crystal, represented as the full width at half maximum (FWHM) of the diffracted profile (known as the Darwin width), is extremely narrow (fractions of an arcsec to a few arcsec depending on the photon wavelength, see (Zachariasen, 1945)), whereas angular acceptances of

## 1.1. Astronomical application

---

several tens of hundredth arcsecond are desirable; therefore perfect crystals are not suitable for Laue lenses. In order to increase the angular acceptance or the energy passband of individual crystals, mosaic crystals or curved crystals must be used. For astronomical applications, crystals with mosaicity or total bending angles ranging from a few tens of arcseconds to a few arcminutes are of interest.

The focal length  $f$  has a key importance in the case of Laue lenses. Indeed from the expression of the energy passband ( $E_{min}$ ,  $E_{max}$ ) of a lens, it results that the lens radii ( $r_{min}$ ,  $r_{max}$ ) depend linearly on  $f$  :

$$\begin{aligned} r_{min} &\approx \frac{hcf}{d_{hkl}E_{max}} \\ r_{max} &\approx \frac{hcf}{d_{hkl}E_{min}} \end{aligned} \quad (1.0.4)$$

High energy photons are diffracted by the inner part of the lens so, to get a lens with a defined inner area, the focal length must be increased. It is important to note that the lens area approximately increases with  $f^2$ . An X and  $\gamma$  ray lens with a broad coverage from 300 keV to 1.5 MeV was proposed by Lund (Lund, 1992, Lund, 2005). He assumed the lens constituted by mosaic crystals of Copper and Gold. In order to achieve a significant effective area at high energies (350 cm<sup>2</sup> at 300 keV and 25 cm<sup>2</sup> at 1.3 MeV), the focal length proposed was 60 m.

## 1.1 Astronomical application

Broad band X and  $\gamma$  ray missions, like BeppoSAX, and INTEGRAL, have shown that, in order to better understand the physics underlying several classes of galactic and extra-galactic sources, two main requirements on the instrumentation are crucial (Frontera et al., 2012):

1. to be able to cover a broad energy band: from a fraction to several hundred of keV;
2. to achieve a high spectrum sensitivity.

The current experimental scenario is the following:

- low energy X ray (0.1÷10 keV) telescopes are available and are well tested in space;
- medium energy X ray (up to 70/80 keV) telescopes, based on multilayer mirrors, are mature and will be tested in space in the next future;
- high energy X ray (>70/100 keV) telescopes are under development.

To take full advantage of the extraordinary potential of hard X and soft  $\gamma$  ray astronomy, a new generation of focusing telescopes is needed.

With Laue lenses, a big leap in both flux sensitivity and angular resolution is expected. In particular, for the sensitivity the expected increase is by a factor of 10 – 100 with respect to the best non-focusing instruments of the current generation. Concerning the angular resolution, the increase is expected to be more than a factor 10 (from  $\sim 15$  arcmin of the telescopes like INTEGRAL IBIS to less than 1 arcmin), (Frontera and von Ballmoos, 2010).

The astrophysical issues that are expected to be solved with the advent of these telescopes are many and of fundamental importance. A thorough discussion of the science case has been carried out in the context of the mission proposal *Gamma Ray Imager* (GRI), submitted to ESA in response to the first AO of the *Cosmic Vision 2015–2025* plan (Knödlseeder et al., 2009; Frontera et al., 2005; Knödlseeder, 2006).

Some of these astrophysical issues are:

- I. *Deep study of high energy emission physics in the presence of super-strong magnetic fields (magnetars);* soft Gamma Ray Repeaters (SGRs) and Anomalous X ray Pulsars (AXPs) have raised many questions related to the role of their strong magnetic field in the high energy emission ( $> 100$  keV). Furthermore, also the belonging of these two types of source to the same class can be understood.
- II. *Deep study of high-energy emission physics in compact galactic objects and Active Galactic Nucleus (AGNs);* high energy emission in compact galactic objects and AGNs is also not well understood. The emission region can be investigated measuring the high energy cutoff and its relation to the power-law photon index of the energy spectrum. Furthermore, AGNs physics is in the focus of astrophysicists also to establish the origin of Cosmic X ray Background.
- III. *Positron Astrophysics;* positron production occurs in a variety of cosmic explosion and acceleration sites, and the observation of the characteristic 511 keV annihilation line provides a powerful tool to probe plasma composition, temperature, density and ionization degree. Compact objects, both galactic and extra-galactic, are believed to release a significant number of positrons.
- IV. *Establishing the precise role of non-thermal mechanisms in extended objects like galaxy clusters*
- V. *Origin of cosmic hard X/soft  $\gamma$ -ray diffuse background*
- VI. *Physics of supernova explosions*

## 1.2. Medical application

---

For a detailed description of these issue see [Frontera and von Ballmoos, 2010], and the references therein.

In this perspective, Italian Space Agency funded the **Laue project**, with the aim to develop a new technology for building a Laue lens with a broad energy band ( $70 \div 300$  keV) and long focal length (20 m), for astrophysics observations. This work is in part devoted to realize suitable optical elements, based on curved crystals, to be used as focusing elements in this lens (see Chap. 6 ).

## 1.2 Medical application

On the basis of a know-how developed during the Laue project, another important project is funded by SPINNER (Emilia Romagna Region) with the aim of developing an innovative in-vivo medical imaging tool for tomography in nuclear medicine. This thesis is completely included in that project.

The term medical imaging indicates a group of techniques allowing to take images of inside of the human body (parts, tissues, or organs) for use in clinical diagnosis, treatment and disease monitoring; it certainly represented a revolution in the world of medicine. Medical imaging shows a great versatility and it finds so various applications.

It emerges the need to identify more advanced solutions in the field of medical imaging technology with the goal to provide always more effective and high resolution images in order to achieve the most truthful diagnosis and accordingly making the best medical decision. This means not only the giving to patients of the best therapy, but also to avoid unnecessary procedures often caused by false positives or overestimated disease severity and prognosis.

Typically, the identification and monitoring of neoplastic diseases is performed by administering to the patient a specific radiopharmaceutical (biological compounds containing a radioactive isotope) to locate physiological abnormalities in the body. These isotopes are typically  $\gamma$  ray emitters of  $\sim 100 \div 200$  keV in energy and with half-lives  $T_{1/2}$  on the order of a few hours (see Table 1.1).

The basic process for nuclear imaging involves introduction of a radiopharmaceutical into the patient (usually by intravenous injection) which subsequently accumulates in the target site or biological process of interest. Higher concentrations of the radiopharmaceutical yield a higher  $\gamma$  ray emission rate relative to surrounding tissues and background. These  $\gamma$  rays are generally captured by means of gamma cameras that subsequently send the data to a computerized system that generates a two or three dimensional image (Adler et al., 2003) see (Figure 1.2.1).

Currently, most nuclear medicine imaging systems have limited spatial resolution that ranges from 7 to 15 mm [Roa et al., 2005]. For example the latest di-

| Nuclide | $T_{1/2}$ | $\gamma$ ray energy (keV) | Purpose                       |
|---------|-----------|---------------------------|-------------------------------|
| Cr-51   | 28 d      | 320                       | red cell volume               |
| Ga-67   | 79.2 h    | 93, 185, 300, 393         | tumor location e inflammation |
| I-123   | 13 h      | 159                       | imaging of thyroid            |
| In-111  | 67 h      | 171, 245                  | labeling white blood cell     |
| Tc-99m  | 6.02 h    | 140.5                     | Multi-purpose imaging         |
| Tl-201  | 73 h      | 135, 166                  | Myocardial imaging            |
| Xe-133  | 5.3 h     | 81                        | Ventilation imaging           |
| F-18    | 1.83 h    | 511                       | Tumor imaging                 |

Table 1.1: Typical radiopharmaceuticals used in nuclear diagnostic medicine.



Figure 1.2.1: Patient undergoing a scan using a gamma camera. Administration of a radiopharmaceutical (upper left display) [Roa et al., 2005] .

agnostic system in nuclear medicine, the Positron emitted Tomography (PET), can achieve resolutions of 4/5 mm at best. Furthermore, because the radiopharmaceuticals needed for PET imaging have significantly short half-lives (at most two hours), relatively large radiopharmaceutical doses must be prepared to leave enough activity to image the patient. In addition, most PET centers must be located in close proximity to a cyclotron facility, in order to minimize the transport time of the radiopharmaceutical from the preparation laboratory to the imaging room.

The possibility to obtain more defined, and therefore more accurate, images of the examined area depends on the ability of focusing radiations, and more precisely, of the lens interposed between the patient ( $\gamma$  ray source) and the radiation detector. A Laue lens can increase, with respect to other diffracting instruments, the focusing power. The application of this new system is envi-

## 1.2. Medical application

---

sioned to scan the patient's body and, after a software elaboration, to produce 2D or 3D images with a spatial resolution of  $\leq 2$  mm. If a patient has undergone a full-body scan and the data suggest the presence of a tumor or suspicious process (e.g., ischemia), a localized scan of that region could be performed with this imaging system without the need of injecting more radiopharmaceutical in the patient. This system may be better able to provide additional information to the size of the tumor or suspicious process and to define its location more accurately .

The SPINNER project proposes to realize a new type of engineered Laue lens realized with curved crystals as optical elements. Curved crystals, in this case are not used as focusing optical elements, because the geometry of the lens is designed in order to focalize the incident X and  $\gamma$  beam into a focal point. Curved crystal are used to increase the angular acceptance of the lens and so to diffract the most part of the photons that come from the radiopharmaceutical injected in the patient (Fig. 1.2.2).

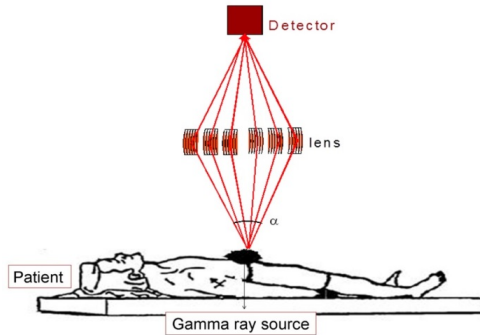


Figure 1.2.2: Schematic diagram of a single lens constituted of curved crystals with its corresponding detector.

This method of  $\gamma$  ray focusing and subsequent detection eliminates the need for high-spatial resolution collimators typically used in gamma cameras which causes significant reduction in sensitivity (Chandra, 1999). Moreover, this photon diffraction imaging system can be tuned to diffract a specific  $\gamma$  ray energy (within  $\sim 100 - 200$  keV) by simply adjusting the source-to-lens and lens-to-detector distance such that the lens remains equidistant between the source and detector. This adjustment changes the Bragg angle to match the defined  $\gamma$  ray energy.





## Chapter 2

# Diffraction of X and $\gamma$ ray from crystals

In this chapter the theory of X and  $\gamma$  ray diffraction from real crystals is outlined, starting from the simplest case: the kinematical theory from ideal crystals. Since for thick and real crystals this theory is limited, the dynamical theory of diffraction is adopted. Dynamical theory allows to understand and to describe the diffraction from mosaic and curved diffracting planes (CDP) crystals, permitting also to predict their diffraction efficiency.

Basic and useful notions of crystallography are also introduced.

## 2.1 Fundamentals of crystallography

### 2.1.1 Crystalline structure

An ideal crystal is constituted by periodical repetition, in the three dimensions of the space, of a single or a group of atoms. The group of atoms constitutes the **cell** and it may have a very complex structure. The repetition of the cell can precisely cover the whole space, without superposition or vacancies, through infinite translations. The **primitive cell** is the smallest cell that contains all the structural and symmetry informations to build-up the structure of the lattice by translations. The periodical repetition of the primitive cell is called **Bravais lattice**. It is built by three vectors not coplanar and linearly independent **a**, **b** and **c** called **primitive vectors**; the primitive cell is the parallelepipedon, with volume  $V_c$ , defined by primitive vectors:

$$V_c = |\mathbf{a} \cdot \mathbf{b} \times \mathbf{c}| \quad (2.1.1)$$

The choice of these three vectors is not unique, so also the choice of the primitive cell is unlimited. A generic lattice vector **t** can be written as  $t = n_1\mathbf{a} + n_2\mathbf{b} + n_3\mathbf{c}$

where  $n_1, n_2, n_3$  are integers.

The primitive cell and the Bravais lattice determine univocally and totally the structure of the crystal.

The classification of the crystal's structure is done by lattice translations and the symmetry operations, constituted by all rigid operations that convert the lattice in itself, leaving it unchanged. In three dimensions there are 14 Bravais lattices divided in 7 categories marked by given symmetry operations, Fig.2.1.1, .

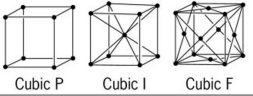
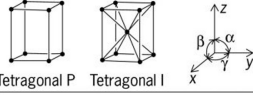
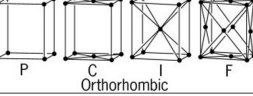
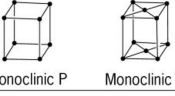



| Bravais lattice cells  | Axes and interaxial angles   | Examples   |
|--|--|--|
|  <p>Cubic P    Cubic I    Cubic F</p>     | <p>Three axes at right angles;<br/>all equal:<br/><math>a = b = c; \alpha = \beta = \gamma = 90^\circ</math></p>   | <p>Copper (Cu), silver (Ag),<br/>sodium chloride (NaCl)</p>  |
|  <p>Tetragonal P    Tetragonal I</p>      | <p>Three axes at right angles;<br/>two equal:<br/><math>a = b \neq c; \alpha = \beta = \gamma = 90^\circ</math></p>  | <p>White tin (Sn), rutile (<math>\text{TiO}_2</math>),<br/><math>\beta</math>-spodumene (<math>\text{LiAlSi}_2\text{O}_6</math>)</p> |
|  <p>P    C    I    F<br/>Orthorhombic</p> | <p>Three axes at right angles;<br/>all unequal:<br/><math>a \neq b \neq c; \alpha = \beta = \gamma = 90^\circ</math></p>   | <p>Gallium (Ga), perovskite (<math>\text{CaTiO}_3</math>)</p>  |
|  <p>Monoclinic P    Monoclinic C</p>      | <p>Three axes, one pair not<br/>at right angles, of any lengths:<br/><math>a \neq b \neq c; \alpha = \gamma = 90^\circ \neq \beta</math></p>   | <p>Gypsum (<math>\text{CaSO}_4 \cdot 2\text{H}_2\text{O}</math>)</p>   |
|  <p>Triclinic P</p>                     | <p>Three axes not at right angles,<br/>of any lengths:<br/><math>a \neq b \neq c; \alpha \neq \beta \neq \gamma \neq 90^\circ</math></p>   | <p>Potassium chromate (<math>\text{K}_2\text{CrO}_7</math>)</p>  |
|  <p>Trigonal R (rhombohedral)</p>       | <p>Rhombohedral: three axes equally inclined,<br/>not at right angles; all equal:<br/><math>a = b = c; \alpha = \beta = \gamma \neq 90^\circ</math></p>  | <p>Calcite (<math>\text{CaCO}_3</math>), arsenic (As),<br/>bismuth (Bi)</p>  |
|  <p>Trigonal and hexagonal C (or P)</p> | <p>Hexagonal: three equal axes coplanar at<br/><math>120^\circ</math>, fourth axis at right angles to these:<br/><math>a_1 = a_2 = a_3 \neq c;</math><br/><math>\alpha = \beta = 90^\circ, \gamma = 120^\circ</math></p> | <p>Zinc (Zn), cadmium (Cd),<br/>quartz (<math>\text{SiO}_2</math>) [P]</p>   |

Figure 2.1.1: The 14 Bravais lattices in the three dimensions. The  $\alpha, \beta,$  and  $\gamma$  are the angles between  $\mathbf{a}, \mathbf{b}$  and  $\mathbf{c}$  respectively.

X-ray diffraction from crystals is concerned with the scattering from atoms that may be thought as lying within families of planes called **Miller indexes** ( $h,k,l$ ). For a given family of planes, the Miller indexes are defined such that plane closest to the origin (but not including the origin) with the intercepts  $(\frac{a}{h}, \frac{b}{k}, \frac{c}{l})$  on the axes ( $\mathbf{a}, \mathbf{b}, \mathbf{c}$ ). The most important features of Miller indices are:

## 2.1. Fundamentals of crystallography

1. by convention, a negative intercept is represented by writing a bar over the correspondent Miller index;
2. the triplet  $hkl$  can be placed in parentheses, when it refers to a specific plane, and in accolades, when it refers to all crystallographic planes described by the same indices;
3. for a given family, the planes are equally spaced so it is possible to define the distance  $d_{hkl}$  between two sets of planes. In the simplest case of a cubic lattice, the  $d$  spacing is given by  $d_{hkl} = \frac{a}{\sqrt{h^2+k^2+l^2}}$  where  $a$  is the lattice parameter.

In Fig. 2.1.2 some examples of lattice planes in a cubic cell are represented.

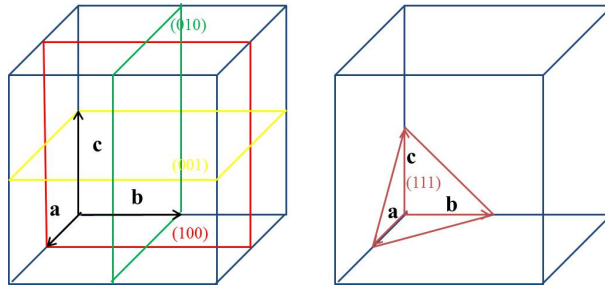


Figure 2.1.2: Examples of lattice planes of a cubic cell.

### 2.1.2 Reciprocal lattice

In crystallography turn out to be useful consider another lattice called **reciprocal lattice**. It is a pure mathematical concept (introduced by[Ewald, 1921]) that hasn't a physical meaning of a structural lattice, but it allows to represent more easily the crystallographic planes.

Starting from the direct lattice characterized by the primitive vectors  $(\mathbf{a}, \mathbf{b}, \mathbf{c})$ , it is possible to built-up a lattice of imaginary points that have a precise relation with the starting lattice. The basis of the reciprocal lattice is a triplet of vectors  $(\mathbf{a}^*, \mathbf{b}^*, \mathbf{c}^*)$ :

$$\mathbf{a}^* = \frac{\mathbf{b} \times \mathbf{c}}{V_c}, \quad \mathbf{b}^* = \frac{\mathbf{c} \times \mathbf{a}}{V_c}, \quad \mathbf{c}^* = \frac{\mathbf{a} \times \mathbf{b}}{V_c} \quad (2.1.2)$$

The relation that links the primitive vectors in real space with that ones in reciprocal space is deducible by eq 2.1.2:

$$\mathbf{a}^* \cdot \mathbf{a} = 2\pi \quad (2.1.3)$$

The volume of the primitive cell in reciprocal lattice is  $V_c^*$  related with direct lattice by  $V_c \cdot V_c^* = 1$ . As in the real space, the distances between two sets of planes is  $d_{hkl}^*$  and its value is  $d_{hkl}^* = \frac{1}{d_{hkl}}$ .

### 2.1.3 Diffraction condition: Bragg and Laue relation

The diffraction depends on the crystal's structure and on the wavelength of the incident radiation, indeed when the wavelength is comparable with or smaller than the lattice parameters a diffraction can occurs. Crystals are natural lattice diffraction for X rays due to their periodic structure, with the periodicity of the order of the Angstrom. W. L. Bragg in 1912 gave an interpretation of the experiments on X ray diffraction as the reflection of the X rays on families of lattice planes and he formulated the Bragg's relations in 1913 (Bragg and Bragg, 1913).

The simplest approach to study X ray diffraction from crystals is to treat it as an interference of rays scattered by a multitude of equidistant lattice planes. The maximum of constructive interference occurs when the path difference between scattered waves is an integer multiple of the wavelength  $\lambda$ . For an incident ray making an angle  $\vartheta$  with the scattering lattice planes spaced  $d$ , the difference path between the incoming and the scattered ray is given by  $2d \sin\vartheta$ , see Fig 2.1.3. The formula to find the maximum of the corresponding interference pattern known as Bragg's law is:

$$m\lambda = 2d_{hkl} \sin \theta \quad (2.1.4)$$

where  $m$  has an integer value and it is known as the order of the corresponding reflection.

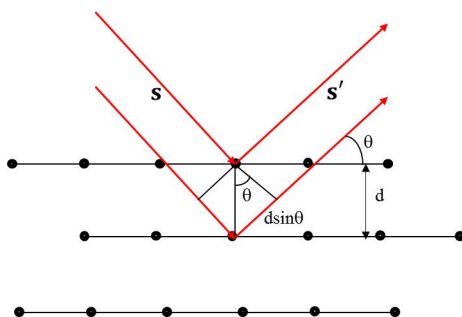


Figure 2.1.3: In panel A: Bragg reflection from a particular family of lattice planes, separated by distance  $d$ . The unit vectors  $s$  and  $s'$  represent the incident and diffracted waves. The difference path of diffracted beam from two atoms is also shown

If a beam impinges on a crystal, each atom within the crystal can scatter the radiation in all directions. Diffracted peaks are observed only in that di-

## 2.1. Fundamentals of crystallography

---

rections and wavelengths for which the scattered rays interfere constructively. To find this condition, two scatterers separated by a displacement vector  $\mathbf{d}$  are considered, Fig.2.1.3 . The incident beam has a direction of propagation described by the unit vector  $\mathbf{s}$ , a wavelength  $\lambda$  and a wavevector  $\mathbf{k}$ . A scattered ray will be observed in direction  $\mathbf{s}'$  with the same wavelength  $\lambda$  of the incident beam and with wavevector  $\mathbf{k}'$ , provided that the path difference between the rays scattered by each atoms is an integral number of wavelengths.

From Figure 2.1.3 B the path difference is  $\mathbf{d} \cdot (\mathbf{s} - \mathbf{s}')$ . The condition for constructive interference is that the path difference is a multiple of  $\lambda$ ; expressing it in wavevectors:

$$\mathbf{d} \cdot (\mathbf{k} - \mathbf{k}') = 2\pi m. \quad (2.1.5)$$

Because the reciprocal lattice is a Bravais lattice, if  $\mathbf{k}$  and  $\mathbf{k}'$  are reciprocal lattice vectors, so is  $(\mathbf{k} - \mathbf{k}') = \mathbf{G}$  (**Laue condition**), where  $\mathbf{G} = h\mathbf{a}^* + k\mathbf{b}^* + l\mathbf{c}^*$  is called **scattering vector**. It will be demonstrated that the Laue condition is equivalent to the Bragg relation expressed in eq. 2.1.4.

Assuming that the Laue condition is satisfied and that  $\mathbf{k}$  and  $\mathbf{k}'$  make an angle  $\theta$  with the planes perpendicular to  $\mathbf{G}$ , see Fig. 2.1.4

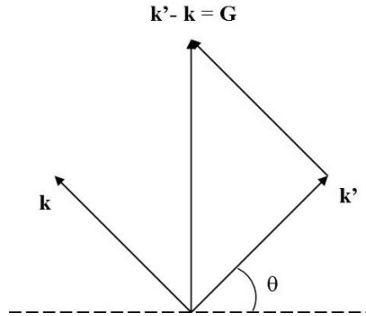


Figure 2.1.4: Scheme of Laue condition. The scattering vector  $\mathbf{G}$  is represented.

The distance between successive planes in a family must satisfy:

$$|\mathbf{G}| = \frac{2\pi m}{d} \quad (2.1.6)$$

and from the Fig. 2.1.4 is possible to obtain:

$$|\mathbf{G}| = 2|\mathbf{k}| \sin \theta \quad (2.1.7)$$

So from eq. 2.1.6 and eq. 2.1.7 and considering the definition of  $k$  as  $k = \frac{2\pi}{\lambda}$ , the Bragg condition  $n\lambda = 2d \sin \theta$  is found.

### 2.1.4 Ewald construction

PP. Ewald proposed in 1913 a simple and graphic construction, exhibited in Fig. 2.1.5 that may helps to visualize the diffraction condition in three dimensions.

Draw a sphere in reciprocal space centered on the tip of the incident wavevector  $\mathbf{k}$  and with radius  $k$  (so that it passed through the origin). The wavevector  $\mathbf{k}'$  satisfies the Laue condition if and only if a reciprocal lattice point lies on the sphere's surface and the directions of  $\mathbf{k}'$  is the one joining the center of the sphere with the point on her. In this case there will be a Bragg reflection from the family of real lattice planes perpendicular to that reciprocal lattice vectors.

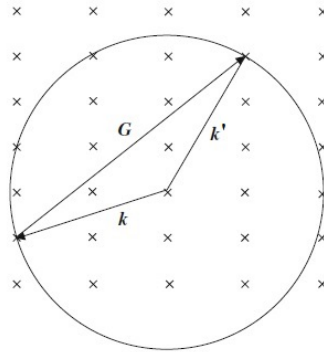


Figure 2.1.5: The Ewald construction. The crosses represent the reciprocal lattice points of the crystal. Given the incident wavevector  $\mathbf{k}$  and a sphere of radius  $k$ , diffraction beam  $\mathbf{k}'$  is produced whenever a reciprocal lattice point lies on the surface of the sphere.

The Ewald construction confirms that for a generic incident wave there will be no Bragg peaks. This constrain can be relaxed by the following experimental method:

1. **Laue method.** Fix the orientation of the single crystal and use a white X ray incident beam containing wavelengths from  $\lambda_1$  to  $\lambda_0$ . The Ewald sphere is considered as the region contained between the two spheres determined by  $\mathbf{k}$  and  $\mathbf{k}'$ . The Bragg peaks will be observed corresponding to any reciprocal lattice vectors laying within this region.
2. **Rotating crystal method.** A monochromatic beam is fixed in direction while the crystal rotates around the same fixed axis. As the crystal rotates, the reciprocal lattice rotates by the same amount. Thus the Ewald sphere (which is determined by the fixed incident vector  $\mathbf{k}$ ) is fixed while the reciprocal lattice rotates around the axis of rotation of the crystal. For each reciprocal lattice point that traverses the circle during the rotation, the Bragg condition is satisfied and a diffracted beam occurs.

### 2.1.5 Geometries of diffraction

The X and  $\gamma$  rays diffraction from crystals can be realized in two different geometries: the *Bragg geometry* in which the reflected beam rises from the same face in which the incident beam impinges, and the *Laue geometry* where the diffracted beam comes from the opposite side of the crystal, in Fig 2.1.6 both geometries are represented. At high energies ( $E > 60$  keV) the angle of diffraction is very small (generally less than one degree), so to get diffraction in Bragg geometry it's necessary a crystal with a large area. On the other hand the Laue geometry can be successfully adopted.

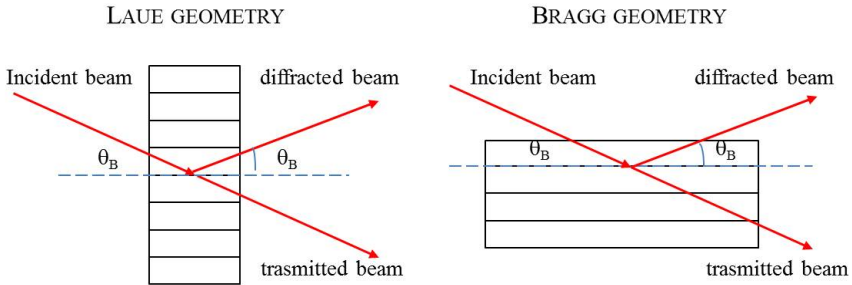


Figure 2.1.6: Laue and Bragg geometries. The lines inside of crystals represent the lattice planes. The angle  $\theta_B$  satisfies the Bragg relation

## 2.2 Diffraction from ideal crystal

In this section the study of the diffraction of X ray from a perfect crystal is presented, with an intuitive approach given by the geometrical diffraction theory, called also kinematical theory.

### 2.2.1 Thomson scattering from a free electron

An electron of mass  $m_e$  and charge  $e$  is positioned on the origin of a coordinate system in which the x axes represents the propagation direction of an electromagnetic wave, with a wavevector  $\mathbf{k}$ , that invests the charge. This wave is characterized by an electric field  $\mathbf{E} = E_0 e^{2\pi i(kx - \nu t)}$ , with  $E_0$  amplitude of the wave. The electron is supposed free and the field exercises on it a force  $\mathbf{F} = e\mathbf{E}$  that produces a oscillation with an acceleration  $\mathbf{a} = \frac{eE}{m_e}$  and a frequency  $n$ , accordingly with that of electric field. From the classical theory of electromagnetism, an electric charge accelerated emits radiation. Thomson has demonstrates that the field produced by charge in a generic point Q at distance  $\mathbf{R}$  from the origin of the axes is :

$$\mathbf{E}(\mathbf{x}, t) = -\frac{1}{4\pi\epsilon_0} \frac{e^2}{m_e c^2} \frac{\sin \psi}{\mathbf{R}} E_0 e^{2\pi i(\mathbf{k}\mathbf{R} - \nu(t - \frac{\mathbf{R}}{c}) - \phi)} \quad (2.2.1)$$

with:

$\psi$  angle between the direction of the electron's acceleration and the direction of the observer,

$\phi$  the phase shift introduced by the process of re-injection of the wave by electron. It is possible to demonstrate that  $\phi = \pi$ ,

$\frac{1}{4\pi\epsilon_0} \frac{e^2}{m_e c^2}$  the *length of diffusion* or *classical electron radius*  $r_e$ . It has a dimension of a length.  $r_e \approx 2.8179 \cdot 10^{-15} \text{m}$ .

It lies in the (x,y) planes as show in Fig. 2.2.1

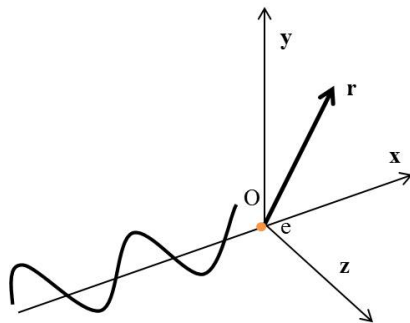


Figure 2.2.1: Scheme of Thomson diffusion. The electron is in the origin O of the reference system.

In terms of intensity:

$$I_p = \left( \frac{1}{4\pi\epsilon_0} \frac{e^2}{m_e c^2} \frac{\sin \psi}{\mathbf{R}} E_0 \right)^2 = I_0 \left( \frac{r_e}{\mathbf{R}} \right)^2 \sin^2 \psi \quad (2.2.2)$$

with  $I_0$  value of incident intensity. This intensity  $I_p$  is inversely proportional to the square of the mass of the electron. This means that the particles heavier than it, as example the proton, contribute at the intensity 1837<sup>2</sup> times less than the electron.

Suppose now that the incident beam is polarized:

- along z axes:  $I_p = I_0 \frac{1}{4\pi\epsilon_0} \left( \frac{r_e}{\mathbf{R}} \right)^2$
- along y axes:  $I_p = I_0 \frac{1}{4\pi\epsilon_0} \left( \frac{r_e}{\mathbf{R}} \right)^2 \cos^2 2\theta$  with  $2\theta$  the angle between the incident beam and the direction of observation.



## 2.2. Diffraction from ideal crystal

In general is necessary to decompose the incident beam in two components, one parallel and the other one perpendicular to the plane that belongs the direct beam and the direction of observation. In this case the intensity  $I_p$  becomes:

$$I_p = I_0 \left( \frac{r_e}{R} \right)^2 P \quad (2.2.3)$$

where  $P$  is called *polarization factor* and it's value is:

$$P = \begin{cases} 1 & \sigma\text{-polarization} \\ \cos^2 2\theta & \pi\text{-polarization} \\ \frac{1+\cos^2 2\theta}{2} & \text{random polarization} \end{cases} \quad (2.2.4)$$

In the diffraction from hard X and  $\gamma$  rays, the diffraction involves very small angles, generally less that one degree. So the value of the three polarizations can be assumed as  $\approx 1$  and in term of intensity this parameter can be neglected.

The Thomson scattering is a coherent scattering because there is a precise relation between the frequency of incident and diffuse beam.

### 2.2.2 Scattering from an atom

Classical scattering from a group of electrons confined to a small volume are discussed (Warren, 1969) and a scheme is represented in Fig. 2.2.2 A. The incident beam, of amplitude  $E_0$ , has a propagation direction represented by the unit vector  $\mathbf{s}$ . The electrons  $n$  are distributed around point  $O$  at  $\mathbf{r}$  position. The scattering are studied in point  $Q$  at a large distance  $R$  from the electrons in a direction given by a unit vector  $\mathbf{s}'$ .

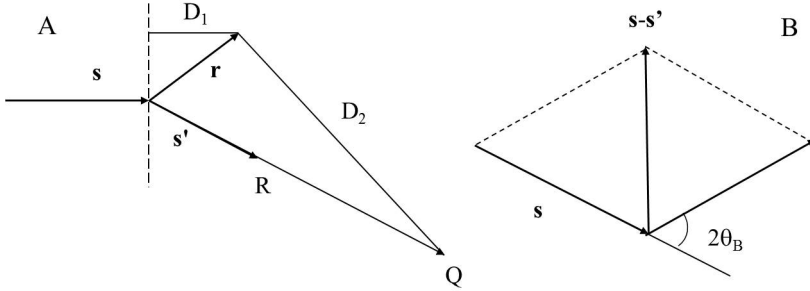


Figure 2.2.2: Panel A: Scattering from a group of electron at distance  $\mathbf{r}$  from the origin. The point  $Q$  is the point of observation. Panel B: relation between the vector of the incident  $\mathbf{s}$  and scattered direction  $\mathbf{s}'$  with vector position  $\mathbf{r}$

The value of the incident electric field in point  $Q$  is given by

$$E = E_0 \frac{r_e}{D_2} \cos \left( 2\pi\nu t - \frac{2\pi}{\lambda} (D_1 + D_2) \right)$$

Considering that the distance of the source and the R are both very big compared to  $\mathbf{r}$ , it is possible to write  $D_2$  as R and:

$$D_1 + D_2 = R - (\mathbf{s} - \mathbf{s}') \cdot \mathbf{r} = R - \Delta \mathbf{S} \cdot \mathbf{r}$$

Expressed in terms of the complex exponential, the diffuse electric field at distance R is the sum over the electron n:

$$\mathbf{E} = E_0 \frac{r_e}{R} e^{2\pi i(\nu t - \frac{R}{\lambda})} \sum_n e^{2\pi i/\lambda \Delta \mathbf{S} \cdot \mathbf{r}} \quad (2.2.5)$$

To calculate the coherent scattering from an atom, each electron can be considered spread out into a diffuse cloud of negative charge, characterized by a charge density  $\rho(\mathbf{r})$ . The quantity  $\rho(\mathbf{r})d\mathbf{r}$  is the ratio of the charge in volume  $d\mathbf{r}$  centered on  $\mathbf{r}$  position, so that for each electron  $\int \rho(\mathbf{r})d\mathbf{r} = 1$ . The wave mechanical treatment says that the amplitude of scattering from the element  $\rho(\mathbf{r})d\mathbf{r}$  is equal to  $\rho d\mathbf{r}$  times the amplitude of classical scattering from a single electron. The total amplitude of scattering is calculated considering that instead of electrons at positions  $\mathbf{r}$ , we have charge elements  $\rho dV$  at positions  $\mathbf{r}$ , and by replacing the sum by an integral the eq. 2.2.5 can be written as:

$$\mathbf{E} = E_0 \frac{r_e}{R} e^{2\pi i(\nu t - \frac{R}{\lambda})} \int e^{2\pi i/\lambda \Delta \mathbf{S} \cdot \mathbf{r}} \rho(\mathbf{r})d\mathbf{r} \quad (2.2.6)$$

The integral  $\int e^{2\pi i/\lambda \Delta \mathbf{S} \cdot \mathbf{r}} \rho(\mathbf{r})d\mathbf{r} = f_e$  is called the *scattering factor per electron* and it represents the scattering amplitude per electron, expressed in electron units. Assuming a spherical symmetry for the charge distribution  $\rho(\mathbf{r})$ , the terms  $\Delta \mathbf{S} \cdot \mathbf{r}$  can be written in polar coordinates as  $2r \sin \theta \cos \phi$  (see Fig.2.2.2B) and with the abbreviation  $k = 4\pi \sin \theta / \lambda$  the  $f_e$  can be simplified as:

$$f_e = \int_{r=0}^{\infty} \int_{\phi=0}^{\infty} e^{ikr \cos \phi} \rho(\mathbf{r}) 2\pi r^2 \sin \phi d\phi dr \quad (2.2.7)$$

The integration with respect to  $\phi$  is readily performed, so

$$f_e = \int_0^{\infty} 2\pi r^2 \rho(\mathbf{r}) \frac{\sin kr}{kr} dr$$

As the same for electric field, the intensity of the *scattering per atom*  $f$  is the sum of the intensities of the scattering from the electrons:

$$f = \sum_n f_e \quad (2.2.8)$$

### 2.2.3 Diffracted intensity from a small single crystal

Based on the Thomson scattering described above, the scattering from a more complicated objects such as crystals is now considered. The details of this study is developed by many authors from which Warren (Warren, 1969).

A monochromatic beam, of intensity  $I_0$ , wavelength  $\lambda$ , and with a direction represented by the unit vector  $\mathbf{s}$ , falls on a small crystal. The crystal is at the origin O and the position of the atoms  $m$  in unit cell  $n_1n_2n_3$  are given by  $\mathbf{R}_n^m = n_1\mathbf{a} + n_2\mathbf{b} + n_3\mathbf{c} + \mathbf{r}_m$ . The intensity of the scattering from the crystal is studied at a generic point of observation Q, in a direction specified by a unit vector  $\mathbf{s}'$  and at a distance R. The conditions are very similar to that illustrated in Fig. 2.2.2 where  $\mathbf{r}$  can be substituted by  $\mathbf{R}_n^m$ . Following the treatment of par. 2.2.2, the instantaneous value of the electric field at the point Q from the atom (m, n) is given by

$$\mathbf{E} = E_0 \frac{r_e}{R} f_m e^{i2\pi\nu t - \left(\frac{2\pi i}{\lambda}\right) [\mathbf{R} - \Delta\mathbf{S} \cdot (n_1\mathbf{a} + n_2\mathbf{b} + n_3\mathbf{c} + \mathbf{r}_m)]} \quad (2.2.9)$$

The total value of electric field at Q is due to all the atoms in the crystal, so it is obtained by summing over m to include all the atoms in a unit cell, and summing over  $n_1n_2n_3$  to include all the unit cells. It is possible to approximate the crystal as a parallelepipedon with  $N_1$  number of cells along the axis a,  $N_2$  along the axis b and  $N_3$  along c so that  $N_1N_2N_3 = N$  is the number of unit cells in the crystal. Separating the summations, the instantaneous field in Q is expressed by

$$\mathbf{E} = E_0 \frac{r_e}{R} e^{i2\pi\nu t} \sum_m f_m e^{\frac{2\pi i}{\lambda} \Delta\mathbf{S} \cdot \mathbf{r}_m} \sum_{n_1=0}^{N_1-1} \sum_{n_2=0}^{N_2-1} \sum_{n_3=0}^{N_3-1} e^{\frac{2\pi i}{\lambda} \Delta\mathbf{S} \cdot (n_1\mathbf{a} + n_2\mathbf{b} + n_3\mathbf{c})} \quad (2.2.10)$$

The summation over m involves the positions  $\mathbf{r}_m$  of the different atoms in the unit cell and it varies from one structure to another. It is called the *structure factor* F and it is defined as:

$$F_{hkl} = \sum_m f_m e^{\frac{2\pi i}{\lambda} \Delta\mathbf{S} \cdot \mathbf{r}_m} \quad (2.2.11)$$

The quantity  $F_{hkl}$  plays an important role in the diffraction theory. If  $\Delta S = 0$ , the structure factor F is simply  $F = \sum_m f_m$ , so F approaches the atomic number Z. This means that the structure factor gives immediately an estimation of the number of scatters in the atom.

The summations over  $n_1, n_2, n_3$  in eq. 2.2.10 have the form of geometric progressions and they can be rewritten as:  $\frac{e^{\frac{2\pi i}{\lambda} \Delta\mathbf{S} \cdot N_1\mathbf{a}} - 1}{e^{\frac{2\pi i}{\lambda} \Delta\mathbf{S} \cdot \mathbf{a}} - 1}$

So the value of the electric field in Q is:

$$E = E_0 \frac{r_e}{R} e^{i(2\pi\nu t - \frac{2\pi}{\lambda})} F_{hkl} \frac{e^{\frac{2\pi i}{\lambda} \Delta \mathbf{S} \cdot N_1 \mathbf{a}} - 1}{e^{\frac{2\pi i}{\lambda} \Delta \mathbf{S} \cdot \mathbf{a}} - 1} \times \frac{e^{\frac{2\pi i}{\lambda} \Delta \mathbf{S} \cdot N_2 \mathbf{b}} - 1}{e^{\frac{2\pi i}{\lambda} \Delta \mathbf{S} \cdot \mathbf{b}} - 1} \times \frac{e^{\frac{2\pi i}{\lambda} \Delta \mathbf{S} \cdot N_3 \mathbf{c}} - 1}{e^{\frac{2\pi i}{\lambda} \Delta \mathbf{S} \cdot \mathbf{c}} - 1} \quad (2.2.12)$$

To find the intensity of the electric field  $I_p$  in Q it is required to calculate  $EE^*$  and express it in a simplest form. In particular it is possible to develop the three exponential expression in a geometrical form:

$$\left( \frac{e^{iN_x} - 1}{e^{ix} - 1} \right) \left( \frac{e^{-iN_x} - 1}{e^{-ix} - 1} \right) = \frac{\sin^2 \frac{Nx}{2}}{\sin^2 \frac{x}{2}} \quad (2.2.13)$$

So the intensity of the electric field is:

$$I_p = I_0 \left( \frac{r_e}{R} \right)^2 PF_{hkl}^2 \frac{\sin^2 \left( \frac{\pi}{\lambda} \right) \Delta \mathbf{S} \cdot N_1 \mathbf{a}}{\sin^2 \left( \frac{\pi}{\lambda} \right) \Delta \mathbf{S} \cdot \mathbf{a}} \times \frac{\sin^2 \left( \frac{\pi}{\lambda} \right) \Delta \mathbf{S} \cdot N_2 \mathbf{b}}{\sin^2 \left( \frac{\pi}{\lambda} \right) \Delta \mathbf{S} \cdot \mathbf{b}} \times \frac{\sin^2 \left( \frac{\pi}{\lambda} \right) \Delta \mathbf{S} \cdot N_3 \mathbf{c}}{\sin^2 \left( \frac{\pi}{\lambda} \right) \Delta \mathbf{S} \cdot \mathbf{c}} \quad (2.2.14)$$

The three equations  $y = \frac{\sin^2 Nx}{\sin^2 x}$  called *Laue equation* determine the intensity. The function  $y$  is essentially zero everywhere except in proximity of  $x = n\pi$ , where the function reaches the maximum value. So the diffracted intensity  $I_p$  is essentially zero while it can achieve a maximum when the three quotients are simultaneously close to zero:

$$\begin{aligned} \Delta \mathbf{S} \cdot \mathbf{a} &= h\lambda \\ \Delta \mathbf{S} \cdot \mathbf{b} &= k\lambda \\ \Delta \mathbf{S} \cdot \mathbf{c} &= l\lambda \end{aligned} \quad (2.2.15)$$

These three equations together are equivalent to the Bragg law.

### 2.2.3.1 Integrated intensity from small single crystal

The most useful quantity which can be both calculated and measured is the "integrated intensity" and which gives directly information of the diffraction efficiency of the measured crystal.

Lets consider a collimated incident beam impinging on a small single crystal at the Bragg angle  $\theta_B$  for the set of planes  $(hkl)$ . The diffracted beam falls normally upon a receiving surface at distance  $R$  from the crystal where it is detected.

Since intensity is energy per unit area per unit time, the integrated intensity  $I_i$  is the total energy obtained by integrating  $I_p$  over time and over the area of the detector. It is convenient to represent the three Laue conditions in eq. 2.2.15 as a vector in reciprocal space  $\Delta \mathbf{S} \cdot \mathbf{c} = \lambda = \lambda (p_1 \mathbf{b}_1 + p_2 \mathbf{b}_2 + p_3 \mathbf{b}_3)$  with  $\mathbf{b}_1 \mathbf{b}_2 \mathbf{b}_3$  reciprocal vectors and  $p_1 p_2 p_3$  integer coefficients. So the value  $I_i$  in a volume in the reciprocal space  $dV = \sin 2\theta d\alpha d\beta d\gamma$  becomes:

$$I_i = I_p \frac{R^2}{\sin^2 2\theta} F_{\text{hkl}}^2 \int \int \int \frac{\sin^2 \pi \cdot N_1 p_1}{\sin^2 \pi p_1} \frac{\sin^2 \pi \cdot N_2 p_2}{\sin^2 \pi p_2} \frac{\sin^2 \pi \cdot N_3 p_3}{\sin^2 \pi p_3} dV \quad (2.2.16)$$

Developing the three integral in all reciprocal space and reminding that  $N_1 N_2 N_3 = N$ , the final expression for the total *integrated energy* can be obtained:

$$I_i = I_0 \frac{r_e^2 \lambda^3 V}{V_c \sin^2 2\theta} F_{\text{hkl}}^2 P \quad (2.2.17)$$

where  $V$  is the volume of the small crystal and  $V_c$  is the volume of the unit cell.

Introducing a parameter  $\Lambda$  as  $\Lambda = \frac{\pi V_c}{r_e \lambda |F_{\text{hkl}}|}$  called *extinction length* the  $I_i$  can be written as:

$$I_{i,\text{kin}} = I_0 \frac{\pi^2 \lambda}{\Lambda^2 \sin^2 2\theta} \frac{t}{\cos \theta} P \quad (2.2.18)$$

where the volume of the crystal crossed by the beam can be considered as the thickness  $t$  divided by  $\cos \theta$ . The subscript *kin* helps to remind that this results is valid for the kinematical theory

It is possible to introduce the *integrated reflectivity*  $R_{i,\text{kin}}$  as the ratio between integrated intensity and the incident intensity:

$$R_{i,\text{kin}} = \frac{I_{i,\text{kin}}}{I_0} \quad (2.2.19)$$

This treatment is true for a non absorbing crystal while for absorbing crystal the eq. 2.2.18 becomes:

$$R_{i,\text{kin}} = \frac{\pi^2 \lambda}{\Lambda^2 \sin^2 2\theta} \frac{t}{\cos \theta} P e^{-\frac{\mu t}{\cos \theta}} \quad (2.2.20)$$

### 2.2.4 Limitations and corrections to the kinematical theory: the dynamical theory

As previously said, the kinematical diffraction theory is not the correct treatment for a complete and exhaustive description of diffraction by crystals. Indeed it is based on some approximations:

1. the interference between incident and diffracted beam is not considered, as also the interference that occurs between the scattered beams from crystals (multiple scattering),
2. the thickness of the crystal is small enough to consider the absorption negligible,

3. the refraction index of the crystal is very close to the refraction index of the environment. This assumption is always valid for X and  $\gamma$  rays.
4. The principle of energy conservation is violated: in eq. 2.2.18 the integrated intensity diffracted by a crystal is proportional to its thickness, so the integrated intensity tends to infinity when the thickness goes to infinity. This happens because the diffusive centers in deeper layers receive an incident beam that is considered with the same amplitude of that received in the surface layers. This ignores the interaction of the wave with matter.

Darwin (*Darwin, 1914*) was the first to mark the kinematical theory as incorrect. He introduces the concept of the wavefield: he describes the incident electric field that propagates in the crystal as a sum of plane waves with wavevector that differs from each other by a reciprocal lattice (Bloch waves). The aim of this theory is to determine the possible positions for the tiepoint and so to describe the wavefield that propagates in the crystal. It will be shown that the results of the dynamical theory tend asymptotically to those of the kinematical theory when the crystal thickness is much smaller than a quantity defined by the extinction length, that is inversely proportional to the structure factor  $F_{hkl}$  and to the wavelength  $\lambda$ .

In this thesis the details of the dynamical theory will not be investigated because of their complexity, but the most important results will be exposed, to better understand the problem to obtain crystals for a Laue lens. The reader can find a much more complete treatment of the dynamical theory in Authier (Authier et al., 1996)

### 2.2.5 The dispersion surface

Is possible to represent this concept starting from the Ewald construction. Fig. 2.2.3 shows how one passes from the Ewald sphere to the representation of the Bragg condition. The *Laue point*  $L_a$  is the center of the Ewald sphere, it is situated on the intersection of the two spheres centered at the reciprocal lattice nodes O and H with a radius of curvature  $k = \frac{1}{\lambda}$ ; the position of  $L_a$  exactly satisfies the Bragg condition.

The waves propagating in the medium interact with matter characterized by an index of refraction  $n$ . For X and  $\gamma$  rays this index is slightly less than one so the wave number of waves propagating in the crystal is  $nk < k$  and another two spheres of radius  $nk$  can be drawn inside the other ones; now the point representing the Bragg condition is on the intersection of the two spheres, called *Lorentz point*  $L_o$ , see Fig. 2.2.4 . The distance between the Lorentz and the Laue point is  $L_oL_a = k(1-n)/\cos\theta_b$ . The wave propagating in the incident direction is called *refracted wave*.

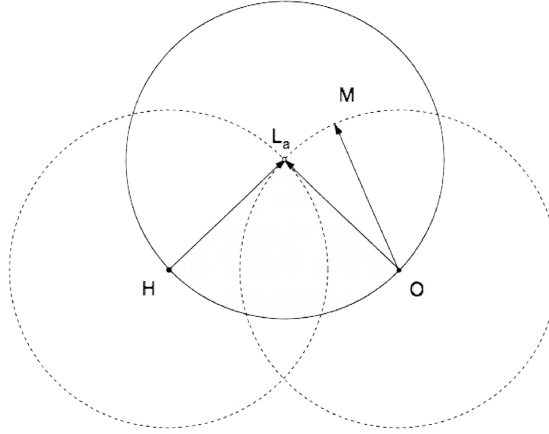


Figure 2.2.3: Diffraction condition according to the kinematical theory from a reciprocal space.  $\overrightarrow{OH}$  is a vector of reciprocal space,  $L_a$  is the Laue point that satisfies the Bragg condition,  $\mathbf{OL}_a = \mathbf{k}_0$  and  $\mathbf{HL}_a = \mathbf{k}_h$  are the wavevector of incident and reflected beam respectively, ( $\|\mathbf{OL}_a\| = \|\mathbf{HL}_a\| = 1/\lambda$ ).  $\mathbf{OM}$  is a wavevector that don't satisfies the Bragg's condition. Both the dotted spheres have a radius of  $k$ .

Contrary to kinematical theory, in a semi-infinite crystal (ideal case) the reflection can occur for an angular range in which the Bragg condition is satisfied, called *reflection domain*. So, for every position within the reflection domain, there is a refracted beam, of wavevector  $\mathbf{k}_0 = \mathbf{OP}$  coexisting with the reflected wave  $\mathbf{k}_h = \mathbf{HP}$ , Fig. 2.2.5. For reason of symmetry, P don't lie on either of the two sphere but on a connecting surface between them, called the *dispersion surface*. In this case there are two coexisting waves, with wavenumbers differing from  $nk$  and closely linked to form a wavefield; to stress this concept Ewald called the point P *tiepoint*. The position of P determines the direction of propagation of the wavefield.

The angular width of the reflection domain is represented in reciprocal space by the size of the dispersion surface, which diameter is proportional to  $F_{hkl}$ . So the larger is the structure factor, so is the reflection domain and the stronger is the interaction. The dispersion surface is constituted by two hyperbolae in the proximity of  $L_o$ , with a distance from it given by the inverse of the extinction length, indeed the distance of Lorentz point to the dispersion surface is shorter than the distance of the Lorentz point to the Laue point.

### 2.2.5.1 Qualitative approach to the dynamical theory

The wavenumber of the wave propagating in the vacuum in the incident or reflected direction is  $k$  and the common extremity  $M$  of their wavevector  $\mathbf{OM} = \mathbf{k}_0$  and  $\mathbf{HM} = \mathbf{k}_h$  lies on the sphere of radius  $k$  and centered in  $O$  and  $H$

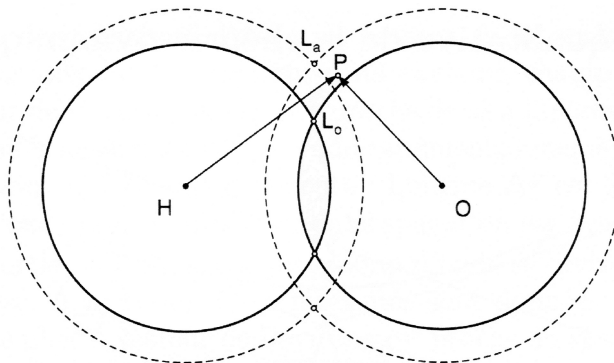


Figure 2.2.4: Influence of the index refraction on the Ewald construction. The Bragg's condition is now satisfied in the the Lorentz point  $L_o$  that lies in the intersection of the spheres of radius  $nk$  (solid line). The vector  $\mathbf{OP}$  is the refracted wave and  $\mathbf{HP}$  the reflected wave.

respectively, passing through the Laue point  $L_a$ . The intersections of these spheres with the plane of incidence are two circles which can be approximated by their tangent  $T'_o$  and  $T'_h$ , and the distance  $L_a M$  is  $k\Delta\theta$  where  $\Delta\theta$  is the angle between  $\mathbf{OM}$  and the direction that satisfies the Bragg condition. In the crystal, the incident wave  $\mathbf{OM}$  excites two wavefields, characterized by the tiepoints  $P_1$  and  $P_2$  that are the projections of  $M$  on the two branches of the dispersion surface along the normal of the surface of the crystal, see Fig. 2.2.6

In the crystal the wavefield propagates on straight line parallel with the Poynting's vectors  $\mathbf{S}_1$  and  $\mathbf{S}_2$ , respectively normal to the dispersion surface in  $P_1$  and  $P_2$  and symmetric with respect to the diffracting planes. The Poynting's vectors are proportional to

$$\mathbf{S}_i \propto \mathbf{E}_0^2 + \mathbf{E}_h^2 = \mathbf{s}_0 |E_0|^2 + \mathbf{s}_h |E_h|^2$$

where  $E_0$  and  $E_h$  are the amplitudes of the waves that constituted the wavefield  $i$ , and  $\mathbf{s}_0$  and  $\mathbf{s}_h$  are respectively the unit vectors indicating the incident and reflected directions.

The separation of the intensity between wavefield  $i$  at the entrance surface results from boundary conditions applied to the electric field vectors. The intensity is higher in the wavefield with Poynting vector closer to  $\mathbf{s}_0$  and the ratio of the two wavefield intensities increases with increasing the angle between the Poynting vector and the reflecting planes. At the exit surface of the crystal, the wavefield splits into a reflected and a transmitted wave. Their intensities are again given through boundary conditions and one finds that the as Poynting vector is closer to  $\mathbf{s}_h$  the reflected intensity is higher (or inversely if the



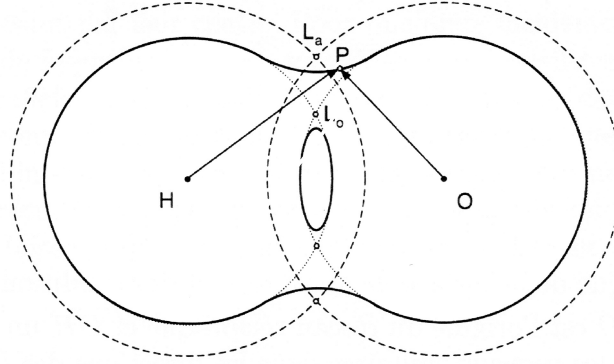


Figure 2.2.5: Representation of the refracted **OP** and reflected wave **HP** that are coexisting. The surface dispersion (solid line) is the surface that connect the two sphere and P is the tiepoint.

Poynting's vector is much closer to  $\mathbf{s}_0$  the transmitted intensity is higher).

When the crystal rotates, the point M moves along the tangent  $T_0$  and crosses the Laue point, which corresponds to the exact Bragg condition. The tiepoints  $P_1$  and  $P_2$  move along the dispersion surface through its center. For an incident wave far from the Bragg condition, the Poynting vectors  $\mathbf{S}_1$  and  $\mathbf{S}_2$  are almost parallel to  $\mathbf{s}_0$  and  $\mathbf{s}_h$  on one side of the Bragg peak, and to  $\mathbf{s}_h$  and  $\mathbf{s}_0$  on the other side. In both cases, all the intensity is transferred to the wavefield parallel to  $\mathbf{s}_0$ , the Poynting vector is parallel to  $\mathbf{s}_0$  and at the exit surface there is only a transmitted wave. This is expected since, far from Bragg incidence, the beam passes straight through the crystal that is only affected by normal absorption (Keitel et al., 1997).

Some important parameters can be deduced by the geometrical construction of the dispersion surface, and they can help to express the reflectivity and the integrated intensity in the dynamical theory.

The asymmetry ratio: Let  $\gamma_0 = \cos \psi - \theta_B$  and  $\gamma_h = \cos \psi + \theta_B$  be the cosine of the angles between the normal to the surface of the crystal and the incident and reflected beam ( $\psi$  is called *asymmetry angle*), respectively. Their ratio  $\gamma$  is so defined:

$$\gamma = \frac{\gamma_0}{\gamma_h} = \frac{\cos(\psi - \theta_B)}{\cos(\psi + \theta_B)} \quad (2.2.21)$$

The Darwin width  $\delta_w$  is the full width at half maximum (FWHM) of the rocking curve in the Laue geometry and the width of the total reflection domain in the Bragg geometry. It is expressed by:

$$\delta_w = \frac{d_{hkl}}{\Lambda} = \frac{\lambda}{\Lambda} \frac{|\gamma_h|}{\sin 2\theta_B} \quad (2.2.22)$$

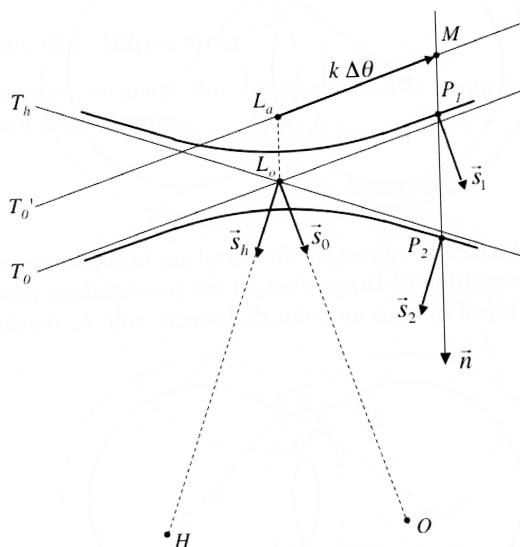


Figure 2.2.6: Scheme of the dispersion surface and of the boundary conditions in the Laue geometry.  $O$  is the origin of reciprocal lattice and  $\mathbf{OH}$  is a reciprocal vector.  $\mathbf{s}_0$  and  $\mathbf{s}_h$  are respectively the unit vector of the incident and reflected directions.  $\mathbf{MO}$  is a wavevector of the incident wave,  $L_a$  and  $L_o$  the Laue and Lorentz points.  $\mathbf{S}_1$  and  $\mathbf{S}_2$  are the Poynting' vector and  $P_1$  and  $P_2$  the tiepoint on the dispersion surface.  $T'_0$  is the tangent of the circle of radius  $k$ ,  $T_0$  and  $T_h$  are the tangent of the circle of radius  $nk$  centered in  $O$  and  $H$  respectively [Authier et al., 1996]

where  $\Lambda$  is the Pendellösung distance in the Laue geometry and the extinction length in the Bragg geometry defined in par. 2.2.3.1.

The deviation parameter  $\eta$  in the Laue geometry is:

$$\eta = \frac{\Delta\theta}{\delta_w} \quad (2.2.23)$$

where  $\Delta\theta$  is the deviation from the exact Bragg condition.

## 2.2.6 Integrated Intensity and reflectivity in Laue case in dynamical theory

The integrated intensity  $I_i$  is the area under the diffraction profile. In dynamical theory the expression for the integrated reflectivity by a non absorbing crystal is:

$$R_{i,\text{dyn}} = \frac{\pi^2 P}{2 \sin 2\theta_B} \frac{\lambda}{\Lambda} B_0(2A) \quad (2.2.24)$$

## 2.2. Diffraction from ideal crystal

where  $A = \frac{\pi t}{\Lambda}$ ,  $B_0(2A) = \int_0^{2A} J_0(z) dz$  and  $J_0(z)$  is the Bessel function of 0 order.

The Fig. 2.2.7 represents the variation of  $B_0(2A)$  as a function of the thickness  $t/\Lambda$ . The value oscillates around 1 when the thickness of the crystal increases and becomes 1 when the thickness goes to infinite. This oscillation, called *Pendellösung effect* is due to the interference of the refracted and reflected waves [Haloïn and Bastie, 2005]. The periodicity of the oscillation is the same of the extinction length, with a minimum in correspondence of it. If the crystal is absorbing the oscillation is quickly smoothed .

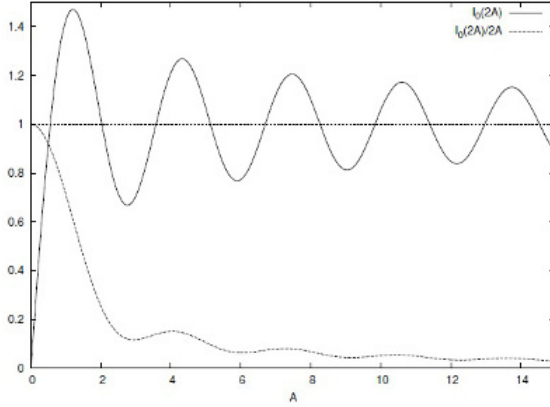


Figure 2.2.7: Variations of the integrated reflectivity with the thickness in case of absorbing non absorbing crystals.

When  $A$  tends to 0, i.e.  $t \ll \Lambda$ , the function  $B_0(2A)$  tends to  $2A$ . In this condition one can find that:

$$I_{i,kin} = I_{i,dyn}$$

So this mean that the kynematical theory can be considered the limit of the dynamical theory for small crystals. The transition between the two theory is leaded by the extinction length. When  $t \ll \Lambda$  the kinematical theory can be applied whereas  $t \gg \Lambda$  the crystal is thick and the dynamical theory can be adopted.

On the basis of the dynamical theory, W. H. Zachariasen (Zachariasen, 1945) presents the theory in a form which enables a direct quantitative comparison with experiment. It is possible to calculate the intensity of reflection and transmission of a parallel monochromatic X ray beam as a function of the angle of incidence to the reflecting planes. The reflectivity  $R$  and the transmittivity  $T$  are obtained from the ratio of the diffracted and transmitted beam respectively with the incident one (Hirsch, 1951) :

$$R = \frac{I_d}{I_0} = |b| \frac{|q|}{|q+z^2|} e^{-\mu t} (\sin^2 av + \sinh^2 a\omega) \quad (2.2.25)$$

$$\begin{aligned} T = \frac{I_T}{I_0} = & \frac{e^{-\mu t}}{|q+z^2|} \left\{ (|q+z^2| + (|q+z^2| + |z^2|) \sinh^2 a\omega \right. \\ & - (|q+z^2| - |z^2|) \sin^2 av \\ & \left. \pm \frac{1}{2} \left| (|q+z^2| + |z^2|)^2 - |q|^2 \right|^{\frac{1}{2}} \right. \\ & \left. \pm \frac{1}{2} \left| (|q+z^2| - |z^2|)^2 - |q|^2 \right|^{\frac{1}{2}} \sin^2 av \right\} \end{aligned} \quad (2.2.26)$$

with:

$$\begin{aligned} q &= Pb\chi_H\chi_{\bar{H}} \\ \chi_H &= -\frac{r_e\lambda^2 F_H}{\pi V_c} \\ z &= \frac{1}{2}(1-b)\chi_0 + \frac{1}{2}b\alpha \\ a &= \frac{\pi t}{\lambda\gamma_0} \\ b &= \frac{y_0}{\gamma_H} \\ \alpha &= 2(\theta_B - \theta) \sin 2\theta_B \end{aligned}$$

where  $\gamma_0$  and  $\gamma_H$  are defined in eq. 2.2.21 and  $t_0$  is the nominal value of the crystal's thickness. The Fig. 2.2.8 compares diffraction profiles as a function of the incidence angle (rocking curve) (eq. 2.2.25) of a silicon crystal (100) oriented for a parallel and monochromatic beam of energy 17 keV. The two profiles represent a crystal with the same thickness of extinction length and a crystal with the same thickness of half extinction length. In the first case the central peak can reach a reflectivity of about 100%. The oscillations are due to the Pendellösung effect.

In Fig. 2.2.9 The diffracted and transmitted profiles of a Si (100) with the same thickness of extinction length are calculated on the basis of eq. 2.2.25 and 2.2.26.

Considering in eq. 2.2.25 and 2.2.26 the thickness  $t_0 \approx 10^{-3}$ cm, the oscillation caused by  $\sin av$  becomes very rapid and is very difficult to observe it in experiments. So it's possible to simplify the previous equations replacing  $\sin^2 av$  with his average value, obtaining:

$$R = \frac{I_d}{I_0} = \frac{1}{2} \frac{|b| |q|}{|q+z^2|} e^{-\mu t} \cosh 2a\omega \quad (2.2.27)$$

$$\begin{aligned} T = \frac{I_T}{I_0} = & \frac{1}{2} \frac{e^{-\mu t}}{|q+z^2|} \left\{ (|q+z^2| + |z^2|) \cosh^2 a\omega \right. \\ & \left. \pm \sqrt{|(q+z^2| + |z^2|)^2 - |q|^2|} \sinh^2 a\omega \right\} \end{aligned} \quad (2.2.28)$$

## 2.2. Diffraction from ideal crystal

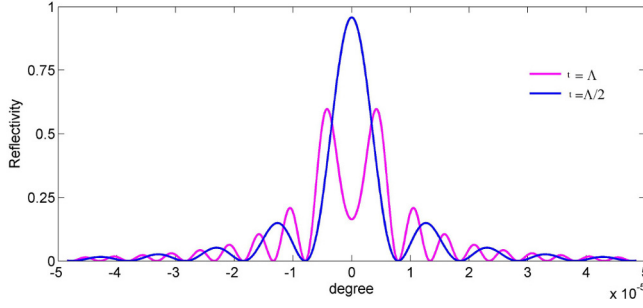


Figure 2.2.8: Rocking curves of a Si (100) crystal with thickness equal to  $\Lambda$  and  $\Lambda/2$  at energy 17 keV.

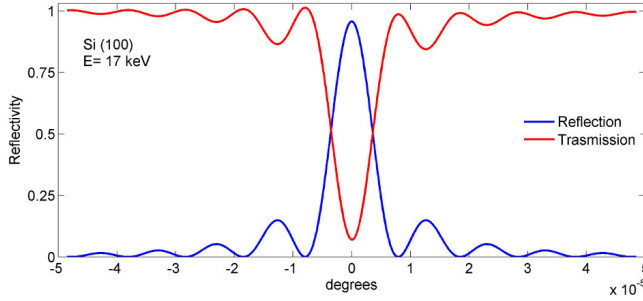


Figure 2.2.9: Diffracted and transmitted profile of Si (100) at energy 17 keV. The thickness is assumed to be the same as the extinction length.

These equations are used in this work to simulate the diffracted and transmitted profiles to compare with that obtained in experiments.

Owing to the complexity of equations 2.2.27 and 2.2.26 it is not possible to do an analytical integration to get the expression and the value of integrated intensity, however it is possible to rewrite the equations in a approximated form that allows to use them more easily with thick crystals:

$$R = \frac{1}{2} \frac{e^{-\mu t}}{1+y^2} \cosh \frac{\mu t \epsilon}{\sqrt{1+y^2}} \quad (2.2.29)$$

$$T = \frac{1}{2} \frac{e^{-\mu t}}{1+y^2} \cosh \left( \frac{\mu t \epsilon}{\sqrt{1+y^2}} + \chi \right) \quad (2.2.30)$$

with

$$\begin{aligned}
 y &= \left( \sqrt{b} \pi \alpha \right) / \left( P r_e \lambda^2 N |F_H| \right) \\
 \cosh \chi &= 1 + 2y^2 \\
 \mu &= \frac{2\pi}{\Lambda} \Gamma F_0'' \\
 \Gamma &= \frac{r_e \lambda^2}{\pi V_c} \\
 \epsilon &= K \frac{F_H}{F_0''}
 \end{aligned}$$

and with  $N = 1/V_c$  number of cell for unit volume and  $P$  assumed to be 1. The change of the sign in the cosh function in eq. 2.2.30 occurs when  $y = 0$  that is the Bragg condition. These equations are used in this work to get the diffraction and transmission profiles without the Pendellösung effect to do a comparison with the experimental profiles.

As an example in Fig.2.2.10 experimental diffracted and transmitted profiles are compared with that ones calculated with equations 2.2.29 and 2.2.30 for a Si (100) crystal of 0.75 mm in thickness with diffracting planes (202) at energy 17 keV. It is important to note that simulated profiles follow very well the experimental profiles, moreover it was found that the value of the experimental integrated intensity  $0.47 \pm 0.2$  arcsec is comparable with that calculated of 0.50 arcsec (Bonnini, 2012). The experimental integrated intensity is obtained by direct integration of the diffraction profile. This demonstrates the validity of the theory adopted based on eq. 2.2.29 and 2.2.30 .

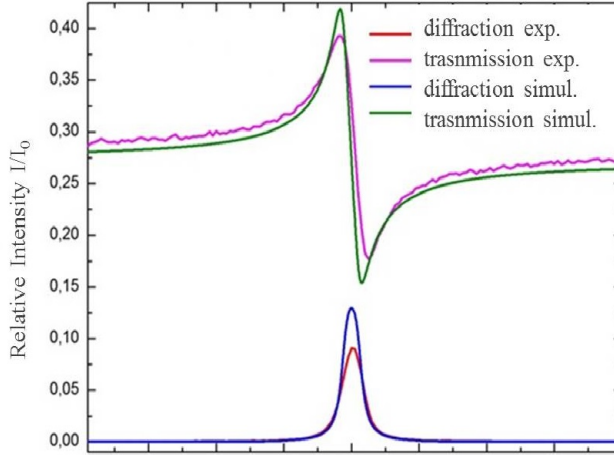


Figure 2.2.10: Comparison between diffracted and transmitted profiles simulated (blue and green lines respectively) and experimental (red and pink lines respectively) for a crystal Si (100) of thickness 0.75 mm at energy 17 keV.

The phenomenon called Borrmann effect is the anomalous increase of the intensity before the expected decrease in correspondence of the diffraction peak.

It will be discussed in the following section.

### 2.2.7 Borrmann effect

The Laue diffraction geometry illustrated in Fig. 2.1.6, in which the asymmetry angle of the diffracting planes is zero, is called *symmetrical geometry*. In condition of real and thin crystals a transmitted peak in correspondence of a reflected is expected.

Suppose now that the crystal is perfect and rather thick. As an example let  $\mu t = 20$ , where  $\mu$  is the linear absorption coefficient and  $t$  is the thickness of the crystal. Under these conditions it is not expected to observe either a reflected or transmitted beam because of the absorption factor  $e^{-\mu t}$ . However at the Bragg condition the reflected and transmitted peaks are simultaneously observed with the same intensity. This means that closer to the Bragg condition there is a slightly reduction of the absorption of the crystal. This surprising experimental fact is called the "*Borrmann effect*", and it was observed for the first time by Borrmann (Borrmann, 1950), or sometimes the "*anomalous transmission effect*". The other characteristic of this effect is that for both beams the point of emergence from the crystal is directly opposite the entrance point, suggesting that the effective combination of the two beams has traveled through the crystal parallel to the diffracting planes, see Fig. 2.2.11.

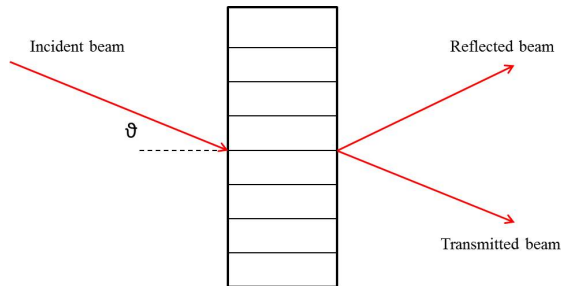


Figure 2.2.11: Emergence of the reflected and transmitted beams at a point directly opposite the entrance position for symmetrical Laue reflection in a thick perfect crystal. The angle  $\vartheta$  satisfies the Bragg condition for that set of diffracting planes.

#### 2.2.7.1 Polarization influence

The effect of polarization is considered in the polarization parameter  $P$  in the expression of integrated intensity 2.2.24; it assumes different values in function of different type of polarization (eq. 2.2.4). This factor affects also in the extinction length, but at high energies, more than 100 keV, the difference between the  $\pi$  and  $\sigma$  polarization becomes completely negligible. So the polarization of

the incident wave at high energies has no considerable effect on the integrated intensity.

## 2.3 Diffraction from mosaic crystal

The theory introduced describes the diffraction of X rays by perfect crystals. These crystals are not suitable for the Laue lens (Chap. 1 ) because they can diffract a very narrow energy band, limited by the Darwin width of the diffraction profile, which also decreases as a function of energy. A suitable crystal should be able to diffract efficiently X ray energies and X ray beams in an angular range relatively large, depending on the lens resolution. For this reason, mosaic crystals are a possible solution.

### 2.3.1 Darwin model

Darwin in 1914 (Darwin, 1914) propose a relatively simple model to describes real crystals as an assembly of tiny identical small perfect crystals, the crystallites, each slightly misaligned with respect to the others according to an angular distribution usually taken as Gaussian, Fig.2.3.1. These are called *mosaic crystals*. In the Darwin's model the integrated reflectivity of a mosaic crystal is much bigger of that for perfect crystal, predicted by the dynamical theory. Indeed each crystallite diffracts a portion of the incident beam (an angular portion if the beam is monochromatic and divergent and a portion of the energy spectrum if the incident beam is polichromatic and parallel) without a phase relation with the beam diffracted from adjacent crystallites; each crystallite can be considered as an independent crystal. The intensity of the diffracted peak in this case is the sum of the intensities of each diffracted beam from crystallites.

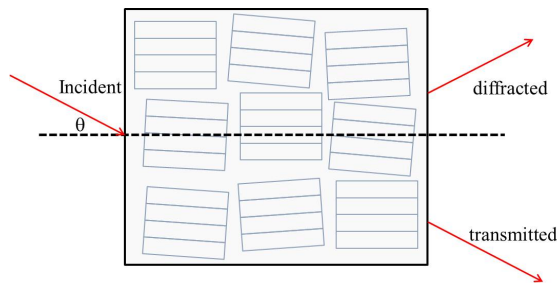


Figure 2.3.1: Scheme of a mosaic crystal in the Darwin model

The angular distribution of the crystallite orientation  $W$  is a gaussian distribution that can be expressed as:



$$W(\theta) = \frac{1}{\sqrt{2\pi}\eta} e^{-\frac{\Delta\theta^2}{2\eta^2}} = 2\sqrt{\frac{\ln 2}{\pi}} \frac{1}{\Omega} e^{-\ln(2)\left(\frac{\Delta\theta}{\Omega/2}\right)^2} \quad (2.3.1)$$

where  $\Omega$ , called *mosaicity* or *mosaic spread*, is the full width at half-maximum (FWHM) of this distribution and:

$$\Omega = 2\sqrt{2\ln 2}\eta \quad (2.3.2)$$

This model is based on these assumptions:

1. the number of the crystallites crossed by the incident beam is big enough to be considered a continue function,
2. the distribution of crystallites has a gaussian symmetry,
3. the crystallites are so small that their absorption can be neglected  $\mu t \ll 1$ .

When the thickness of crystallites are more than  $\sim \Lambda/10$  the kinematical theory is not valid and it is necessary to consider the dynamical theory. In the dynamical theory the interaction between incident and diffracted theory (Pendellösung effect) causes the extinction of the reflected beam; this effect is called *primary extinction*. In the Darwin model the intensity of the diffraction is the coherent sum of the diffracted beam of each single cristallite. However if two nearby crystallites have about a parallel orientation, the first can remove the intensity that will arrive on the consecutive crystallites; this effect is called *secondary extinction*. The *ideally imperfect* crystals are mosaic crystal in which the crystallites are small enough to permit to apply the geometrical theory.

The treatment of the Laue diffraction in symmetrical geometry by a mosaic crystal was studied in detail by Zachariasen (Zachariasen, 1945). The crystal is considered as a slice with parallel surfaces, thickness  $T_0$  and lateral infinite extension.

The reflectivity of a mosaic crystal in the Darwin model is found to be:

$$R_{\text{mos}} = \frac{1}{2} (1 - e^{-\sigma T_0}) e^{-\mu \frac{T_0}{\gamma_0}} \quad (2.3.3)$$

where  $\sigma$  gives the probability per unit length that fotons of direct beam will be reflected by the crystal. It depends on the structure of the crystals and on the distribution of crystallites:

$$\sigma(E, \theta) = W(\theta) \left( \frac{r_e}{V_c} \right)^2 \frac{\lambda^3 P}{\sin 2\theta}$$

The FWHM of the reflected curve is:

$$\Delta u = 2\sqrt{\frac{-\ln\left(-\frac{1}{\sigma}\ln\left(\frac{1}{2}(1+e^{-\sigma})\right)\right)}{\ln 2}}$$

The integrated reflectivity can be approximated as the product of the FWHM of the reflected profile with the value at the top of the peak:

$$R_{\text{int,mos}} = (1 - e^{-\alpha T_0}) \sqrt{\frac{-\ln\left(-\frac{1}{\sigma}\ln\left(\frac{1}{2}(1+e^{-\sigma})\right)\right)}{\ln 2}} e^{-\mu\frac{T_0}{\gamma_0}} \quad (2.3.4)$$

From the Bragg relation (2.1.4) it is easy to find that, when a polychromatic beam impinges on mosaic crystal with an average angle  $\vartheta$  that satisfies the Bragg condition, thanks to the mosaicity, photons with an energy included in a energy range  $\Delta E$  will be reflected:

$$\Delta E = \frac{E\Omega}{\tan \theta} \quad (2.3.5)$$

From eq. 2.3.5 it is evident that the mosaicity defines directly the angular acceptance of the crystals.

Nevertheless, the measurements performed on real crystals of thickness  $T_0$  can't be explained either by the kinematical or by the dynamical model of a perfect crystal. Actually, the angular (or energy) acceptance can be relatively large (up to a few degrees), and the integrated reflectivity is much higher than expected from a perfect crystal:

$$R_{\text{int,kin}} < R_{\text{int,mos}} < R_{\text{int,dyn}}$$

## 2.4 Diffraction from crystal with curved diffracting planes

The main problem in the use of mosaic crystals is the difficulty to grow crystals with defined mosaic spread. Bent crystals with curved diffracting planes (CDP) represent an important alternative to obtain a diffracted energy band bigger with respect to that of perfect crystals. Bent crystals show, in some diffracting geometry and for certain set of diffracting planes, a cylindrical or spherical curvature, depending on the bending technique. The value of this internal curvature is directly linked to the external curvature and it allows to diffract a wide portion, in terms of energy or angle, of the incident beam, so increasing the angular acceptance.

This section is based on the works of (Malgrange, 2002) and (Keitel et al., 1997) based on the dynamical theory in distorted crystals (Authier, 2001).

Penning and Polder in (Penning and Polder, 1961) and Kato in (Kato, 1964) develop simultaneously a theory based on optical geometrical to describe the propagation of X rays in curved crystals, and they reach the same results. These theories are merged in one called theory PPK. They demonstrate that the wavefield, that propagates in straight line in perfect crystals, follows curved path in curved crystals as the light does in a medium with a gradient of refractive index. The geometrical theory no longer applies when the strain gradient is too high. An important contribute to the model arrives from Authir and Balibar in 1970 (Authier et al., 1970). They first introduced the variation of the angle of incidence  $\vartheta$  on the reflecting planes (h,k,l):

$$\partial\theta = \frac{1}{k \sin 2\theta_B} \frac{\partial}{\partial s_h} (\mathbf{u} \cdot \mathbf{h}) \quad (2.4.1)$$

where  $s_0$  and  $s_h$  are the unit vectors of incident and reflected directions respectively,  $\mathbf{h}$  the reciprocal lattice vector of the reflection,  $\mathbf{u}$  the displacement vector and  $k$  the wavevector.

Authier and Balibar introduce the condition written as:

$$\frac{1}{k \sin 2\theta_B} \frac{\partial^2}{\partial s_h \partial s_0} (\mathbf{u} \cdot \mathbf{h}) \ll \frac{\delta_w}{\Lambda} \quad (2.4.2)$$

where  $\delta_w$  is the Darwin width already introduced in eq. 2.2.22 for the application of the dynamical theory to the distorted crystals.

Kato introduces a parameter  $\beta$  that describes the deformation of the reflected planes:

$$\beta = \frac{\Lambda}{\cos^2 \theta_B} \frac{\partial^2}{\partial s_h \partial s_0} (\mathbf{u} \cdot \mathbf{h}) \quad (2.4.3)$$

It is important to point out that the parameter  $\beta$ , which describes the effective distortion of the crystal, is proportional to the extinction length, i.e. proportional to the energy of incident beam. So, a crystal almost perfect at a defined energy may behave like a highly deformed crystal at higher energies; this effect will be observed during some experiment show in the next chapters.

The condition for the application of dynamical theory (*small deformed crystal*, so small strain gradient) becomes (neglecting an unimportant factor  $\cos\vartheta/2$ )

$$\beta\Lambda \ll 1 \quad (2.4.4)$$

where each wavefield propagates following a curved beam path.

Whereas on the contrary for *strongly deformed crystals*

$$\beta\Lambda \gg 1 \quad (2.4.5)$$

the wavefield tie point can jump from one branch to the other, creating a new wavefield.

Let consider the case of a small strain gradient (2.4.4) and the Laue geometry. When a plane wave beam impinges onto a crystal with an angle that satisfies the Bragg condition, it propagates along two beam paths. These beam paths which are straight lines in a perfect crystal (Fig. 2.4.1 a) became curved and follow hyperbolic paths (Fig. 2.4.1 b) due to the distortion of the lattice planes. The tie point moves along the dispersion surface as the angle of incidence varies on the reflecting planes. The curvature of the beam path are proportional to the strain. For very large strain gradients the tie point jumps from one branch to the other; the new wavefield is created in this area and follows a normal propagation, which becomes very rapidly a straight line Fig. 2.4.1 c.

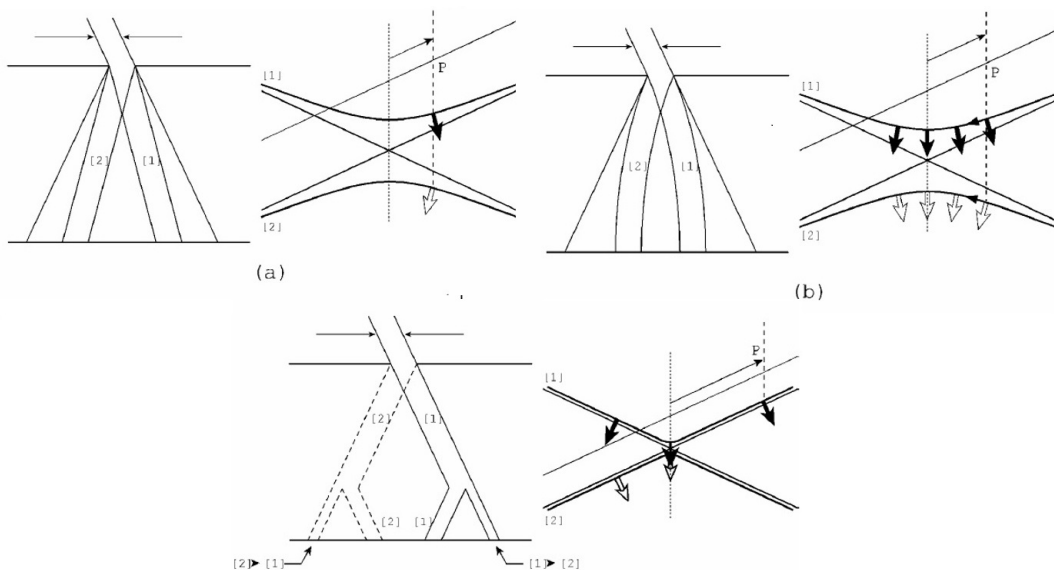


Figure 2.4.1: Propagation of a parallel incident beam in a symmetric Laue diffraction and the corresponding dispersion hyperbola: a) Perfect crystal; b) Reflecting planes slightly curved ( $\beta\Lambda \ll 1$ ); c) Reflecting planes strongly curved ( $\beta\Lambda \gg 1$ ). In this last case wavefield 2 is drawn with a dashed line to evidence its negligible intensity.

The fraction of the intensity for wavefield which is transferred into this new wavefield is  $\exp\left(-\frac{\pi^2}{\beta\Lambda}\right)$  and tends to zero for  $\beta\Lambda \ll 1$ .

Consequently, two beams appear: one in the transmitted direction issued from the new wavefield, and one in the reflected direction whose intensity is reduced by the intensity transferred into the new wavefield. Due to the very short fraction of the beam path that corresponds to tiepoints in the domain of reflection, the Borrmann effect is negligible and the intensity is reduced by normal absorption.

## 2.4. Diffraction from crystal with curved diffracting planes

---

In condition of strongly bent crystals the expression for the diffracted peak is:

$$I_{p,ben} = I_0 e^{-\mu t} \left[ 1 - e^{-\frac{\pi^2}{\beta \Lambda}} \right] \quad (2.4.6)$$

The integrated reflectivity  $R_{int,ben} = I_{int}/I_0$  is considered here, rather than the mere peak reflectivity, as the most relevant parameter characterizing the diffraction efficiency of the crystal. In fact, the peak intensity alone does not take into account the width of the rocking curve, which is strongly influenced by crystal features (mosaicity or curvature). Furthermore the rocking curve has a top flat shape with a width  $\omega$  of the plateau equal to  $\omega = \frac{t\delta\beta}{2}$ . So the the integrated intensity for strongly bent crystals can be given approximately by  $I_{p,ben}\omega$  and, taking into account equation 2.4.6, can be written as

$$I_{int,ben} = I_0 e^{-\mu t} \frac{t\delta\beta}{2} \left[ 1 - e^{-\frac{\pi^2}{\beta \Lambda}} \right] \quad (2.4.7)$$

Now, a more strictly condition may occurs. For  $\beta \Lambda \gg \pi^2$  the  $I_{int,ben}$  can be approximated with:

$$I_{int,ben} = I_0 e^{-\mu t} \frac{t\delta\pi^2}{2\Lambda} \quad (2.4.8)$$

So  $I_{int,ben}$  corresponds to the maximum value of integrated intensity for CDP crystals. It does not depend anymore on crystal curvature, and coincides with the  $I_{int,mos}$  of an ideal mosaic crystal.

The discussion of this results will be show in chapter 3.



## Chapter 3

# Diffraction efficiency of bent crystals: theoretical study

The efficiency of a Laue lens for X and  $\gamma$  ray focusing in the energy range  $60 \div 600$  keV is closely linked to the diffraction efficiency of its optical elements.

Both mosaic and CDP crystals can be used for a Laue lens, if they can be produced with the needed angular spread.

Mosaic crystals are good candidates because their angular acceptance can be tuned by modifying the mosaic spread and/or the size of the microcrystals forming the mosaic structure during the growth process. The production of mosaic crystals with a well defined mosaic spread and grain size is a difficult technological task, so that the resulting diffracted intensity is often much lower than that predicted for the ideal case. In addition the peak intensity of mosaic crystals is limited to 50% and they exhibit a non-uniform (typically Gaussian) passband with a width proportional to the mosaicity.

On the other hand in CDP crystals, due to continuous change of the incidence angle of an X ray trajectory on the crystalline planes, re-diffraction within the crystal is prevented so the 50%-limit overcome and they can reach in principle a peak efficiency of 100% (Bellucci et al., 2011). Moreover CDP crystals have a rectangular diffraction profile with width strictly bound up to its curvature, so they have a uniform distribution of the energy passband.

For all these reasons CDP crystals are considered the best candidates for the realization of X and  $\gamma$  focusing system.

In this chapter a comparison of the efficiency between CDP and mosaic crystals was performed on the basis of dynamical theory of X ray diffraction described in Chap. 2. Moreover, some crystal's properties as material, curvature, dimensions, and diffraction geometry will be discussed in order to maximize the efficiency of the crystals, and so the efficiency of the lens.

### 3.1 Diffraction efficiency

Let rewrite some parameters to facilitate the calculation of the integrated reflectivity in order to obtain the maximum diffraction efficiency in bent crystal.

Considering the deformation parameter  $\beta$  in eq. 2.4.3, it can be written as:

$$\beta = \frac{2\Delta\theta}{l\theta} \quad (3.1.1)$$

where  $\delta$  is the Darwin width of the diffraction defined as the full width at half maximum (FWHM) of the rocking curve for a perfect non absorbing crystal and  $l$  is the optical path of the beam along the crystal thickness  $t$ , related by  $l = t/\cos\theta_B$ . Since at high energy the Bragg angle  $\theta_B$  is very small, it is possible to assume  $l = t$ .

The quantity  $\Delta\theta$  is the variation of the Bragg condition along the direction of incident beam direction across the sample thickness. It consists of three terms that consider the lattice bending, the variation of the lattice parameter and the lattice deformation (see for the detail App. A). For a spherical deformation the variation  $\Delta\theta$  is given by (Erola et al., 1990), modified for a spherical curvature):

$$\Delta\theta = \frac{t}{R} \left[ \tan(\phi \mp \theta_B) + \frac{\sin 2\varphi}{2} \frac{c_{11} + 2c_{12}}{c_{11}} \pm \tan \theta_B \left( \cos^2 \phi - \frac{2c_{12}}{c_{11}} \sin^2 \phi \right) \right] \quad (3.1.2)$$

where  $c_{11}$  and  $c_{12}$  are the elastic constants for cubic crystals and  $\varphi$  is the inclination of lattice plane with respect to the surface normal. The signs  $\mp$  and  $\pm$  refer to the condition of angle of incidence lower (first sign) or larger (second sign) than the asymmetry angle  $\phi$ . It is worth noting that for symmetrical Laue diffraction ( $\phi=0^\circ$ ) and in the approximation of isotropic material or high symmetry directions, the  $\Delta\theta$  is zero even if the corresponding lattice planes are bent (Kalman and Weissmann, 1979; Ferrari et al., 2013). The function  $\Delta\theta \cdot \frac{R}{t}$  reported in Fig. 3.1.1 for Bragg angles of  $1^\circ$  (high energy X rays),  $10.6^\circ$  (E=17 keV and Si 220 planes) and  $30^\circ$  represents the “effective curvature” of the lattice in the direction of the incident beam. The variation  $\Delta\theta$  is related to the crystal external curvature radii  $R$  by  $R = t/\Delta\theta$ , so the FWHM of the diffracting profile is proportional to it.

Now, considering the expression of the Darwin width  $\delta$ ,

$$\delta = \frac{2r_e P F_H \lambda^2}{\pi V \sin(2\theta_B)} \quad (3.1.3)$$

the approximated expression of the integrated intensity in eq. 2.4.8 valid for strongly bent crystals, is:

$$I_{\text{int,ben}} = I_0 \left( \frac{r_e F_H P}{V} \right)^2 \frac{t\lambda^3}{\sin 2\theta_B \cos \theta_B} e^{-\mu t} \quad (3.1.4)$$



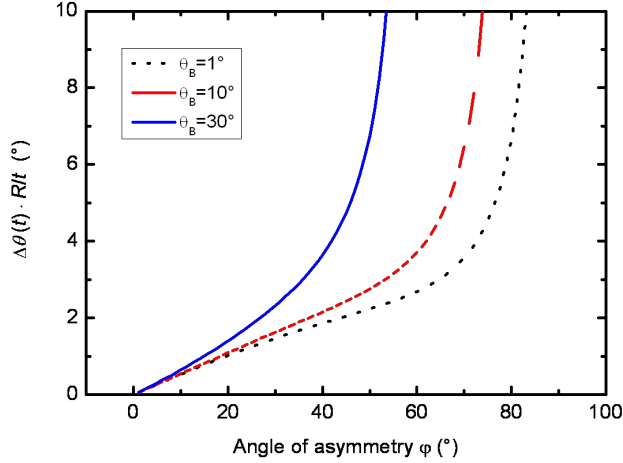


Figure 3.1.1: The function  $\Delta\theta \cdot \frac{R}{t}$  as a function of angle asymmetry and Bragg angles  $1^\circ$ ,  $10^\circ$ ,  $30^\circ$ . We have considered the second sign in Eq. 3.1.2

The integrated reflectivity that has to be optimized is:

$$R_{\text{int,ben}} = \left( \frac{r_e F_{\text{HWP}}}{V} \right)^2 \frac{t \lambda^3}{\sin 2\theta_B \cos \theta_B} e^{-\mu t} \quad (3.1.5)$$

### 3.1.1 Approximated calculation of integrated intensity: Lamellar model

X ray integrated reflectivity of bent crystals is calculated from a model developed in (Erola et al., 1990) where curved crystals can be approximated by a stack of perfect-crystal lamellae which have a gradually increasing tilt angle corresponding to the bending of the crystals. The reflectivity of the crystal is the sum of partial reflections in the lamellae. The thickness of the lamellae is taken such that angles between two successive lamellae is equal to the Darwin width of the reflection.

Considering the variation of the Bragg conditions along the diffracting planes  $\Delta\theta$  in eq. 3.1.2, can be written as:

$$\Delta\theta = \frac{t}{R} [\gamma_0 B(\theta, \phi)]^{-1} \quad (3.1.6)$$

Introducing  $A$  as the reflecting thickness in the units of the extinction length  $\Lambda$  for a lamellae of thickness  $T$

$$A = RB \frac{\lambda}{A^2 \sin 2\theta} \quad (3.1.7)$$

it is possible to obtain the trend of the integrated reflectivity of curved crystals as a function of the curvature of crystals.

$$R_{\text{int}}(A) = \frac{\tanh A}{A} R_{\text{int,ben}} \quad (3.1.8)$$

The trend of the integrated reflectivity can be studied, studying the behavior of  $\tanh A$ :

$$\begin{aligned} \lim_{A \rightarrow \infty} \tanh A &= 1 \\ \lim_{A \rightarrow 0} \tanh A &= A \end{aligned} \quad (3.1.9)$$

### 3.1.2 Crystal's material

The material of the crystals is the first important parameter to be considered in order to optimize the integrated reflectivity 3.1.5, indeed it is mandatory to establish a list of materials fulfilling basic requirements: the material must exist in a crystalline state at room temperature and must have a good diffraction efficiency, it must be easily bent but not be ductile, and it must not be radioactive. Crystals composed of different atoms tend to have larger lattice parameters than pure materials, which dramatically decreases their diffraction efficiency. So, the choice is limited to pure materials and bi-component crystals.

The integrated reflectivity depends on the square of the ratio  $F_H/V$  which is proportional to the atomic density  $N$ . The value of  $N$  as a function of the element atomic number  $Z$  is shown in Fig. 3.1.2 reported in (Barriere et al., 2009).

As can be seen, for single-element materials, the density peaks are evident in correspondence of the  $Z = 5, 13, 28, 45,$  and  $78$ . Common materials like Al, Si, Cu, Ge, Mo, Rh, Ag and Au are good candidates to be used for Laue lenses and should be preferred to other elements if they are available as crystals with the requested properties. Also double-element crystal materials can be used for Laue lenses. Several of them, developed for other applications, are already available, like GaAs, InAs and CdTe. With some improvements, these crystal materials can be used for Laue lenses [Barriere et al., 2010]. Due to the high energies involved, the choice of high- $Z$  mosaic crystals such as Cu, Au and Ag is preferred (Haloïn and Bastie, 2005; Lund, 2005).

### 3.1.3 Effect of crystal's thickness

The crystal thickness  $t$  traversed by the beam is therefore a crucial parameter that must be optimized to achieve the maximum of integrated reflectivity in

### 3.1. Diffraction efficiency

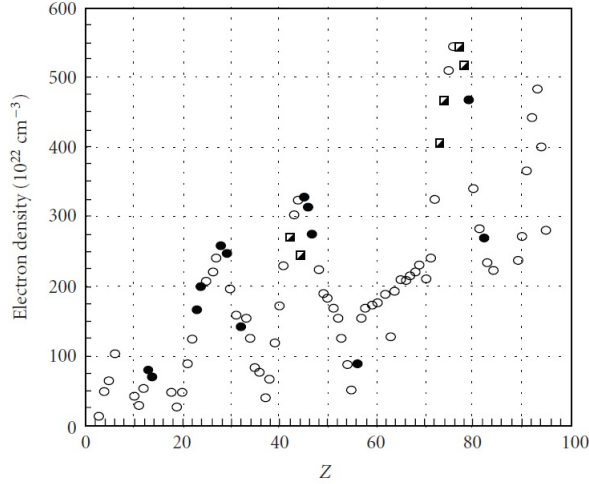


Figure 3.1.2: Density of a crystal unit cell versus element atomic number.

mosaic and CDP crystals.

The thickness which maximizes the diffraction efficiency, can be obtained from the partial derivative of  $R_{\text{int,ben}}$  in eq. 3.1.5 with respect to  $t$  and putting it equal to zero:

$$\frac{\partial R_{\text{int,ben}}}{\partial t} = 0 \quad (3.1.10)$$

The values of thickness that optimize the integrated reflectivity is  $t_{\text{max}} = \frac{1}{\mu}$  as in the case of symmetrical Laue diffraction for mosaic crystals (Authier and Malgrange, 1998). Fig.3.1.3 reports  $t_{\text{max}}$  for ideal mosaic (Cu and Au) and CDP (Si and GaAs) crystals in the energy range of interest; the curve of Ge overlaps that of GaAs due to the equivalent crystal density. It is important to note that  $t_{\text{max}}$  depends only by the absorption and it is almost independent of the reflection geometry; a high absorption coefficient implies a low crystal thickness for efficiency optimization.

Now replacing  $t$  with  $t_{\text{max}} = \frac{1}{\mu}$  in eq. 3.1.5, the formula that expresses the maximum integrated intensity with respect to thickness for ideal mosaic and CDP crystals can be obtained, (Bonnini et al., 2015):

$$R_{\text{int,max}} = \left( \frac{r_e F_{\text{HP}}}{V} \right)^2 \frac{\lambda^3}{e\mu \sin 2\theta_B \cos \theta_B} \quad (3.1.11)$$

Fig.3.1.4 shows the maximized integrated reflectivity  $R_{\text{int,max}}$  calculated from eq.3.1.11 for GaAs, Si, and high-density materials such as Cu and Au usually proposed as X and  $\gamma$  ray lens elements; the diffraction geometries with

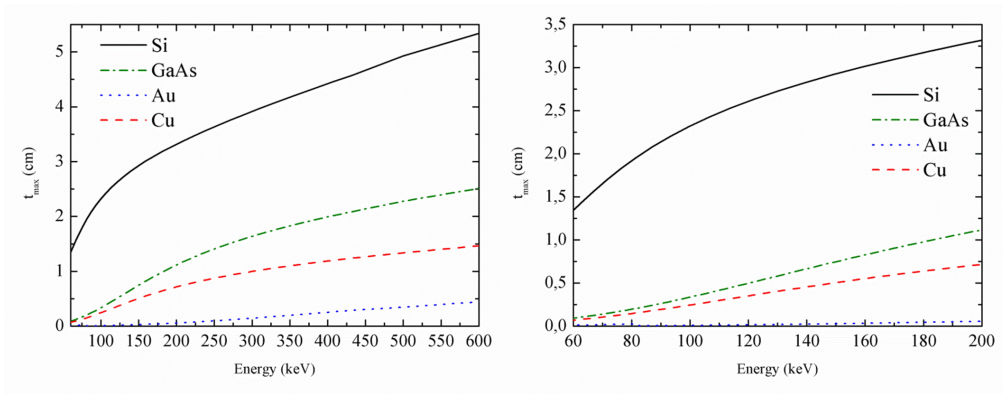


Figure 3.1.3: *Left*: The crystal thickness  $t_{\max}$ , maximizing the integrated reflectivity for CDP crystals (Si, Ge and GaAs) and mosaic crystals (Cu and Au) in the energy range  $60 \div 600$  keV. *Right*: A zoom of  $t_{\max}$  in the energy range  $60 \div 200$  keV.

the highest values of  $F_H$  for face-centred cubic crystals are considered, i.e. the 111 and 220 reflections.

Data concerning the absorption coefficients of the materials considered have been taken from the NIST database (<http://www.nist.gov/pml/data/index.cfm>).

In the range between 80 and 400 keV in the (111) diffraction geometry (Fig. 3.1.4 *bottom*) Cu mosaic crystals provide the higher efficiency, being nearly 2 times larger than that of GaAs and Ge. This is not true for the (220) geometry (Fig. 3.1.4 *upper*), in which GaAs and Ge provide a 30% higher intensity than Cu crystals, thus confirming that a higher Z number does not always correspond to a higher efficiency.

As an example, the integrated reflectivity as a function of the thickness calculated by equation 3.1.11 was studied at a fixed energy  $E = 140.5$  keV, (Roa et al., 2005), Fig. 3.1.5. As expected the integrated intensity increases until it reaches a maximum and thereafter decreases due to the absorption of radiation in the crystal. This calculation is made for different materials as Si, GaAs and Cu at (220) and (111) reflections.

By combining the results of Fig. 3.1.3 and Fig. 3.1.4 it is possible to conclude that even relatively light materials, under the condition of optimal length  $t_{\max}$ , reach an integrated reflectivity comparable or better than high Z crystals in the energy range  $60 \div 600$  keV.

This can considerably increase the real possibility to realize a Laue lens, reducing the huge economical effort that is requested to produce Au and Cu mosaic crystals and also the weight of the system that is a critical point for astronomical applications.

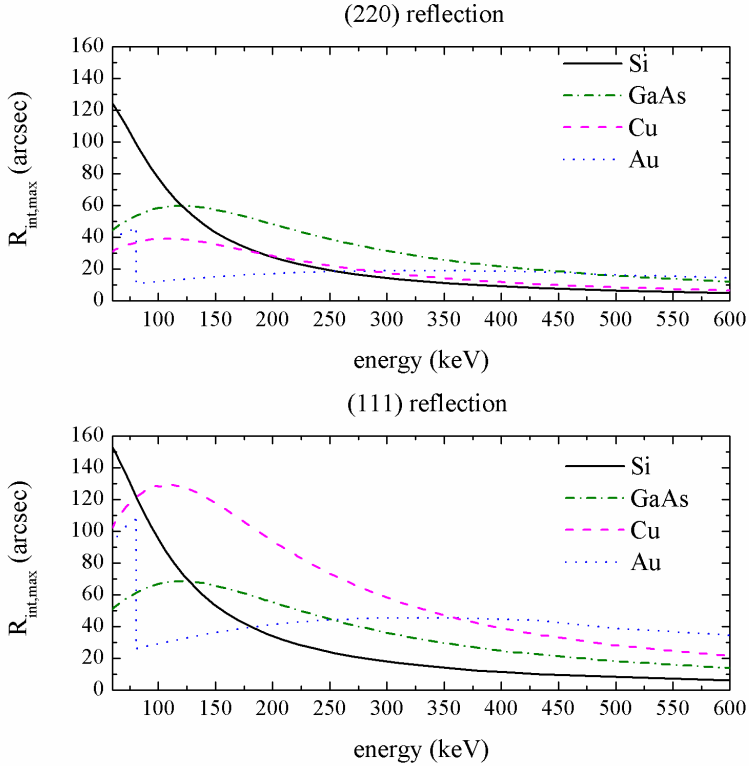


Figure 3.1.4: The calculated integrated reflectivity as a function of energy for Si and GaAs CDPs and for Cu and Au mosaic crystals in the 220 and 111 reflections (top and bottom panels, respectively). The thickness of the crystals was tuned to obtain the maximum integrated reflectivity at each energy.

### 3.1.4 Radius of curvature

Another parameter that must be optimized in order to obtain the maximum of  $R_{\text{int}}$  is the radius of curvature of bent crystals.

As discussed in sec. 2.4 the eq.  $\beta\Lambda = 1$  defines the critical condition for which crystals can be considered *slightly curved* ( $\beta\Lambda \ll 1$ ) or *strongly curved* ( $\beta\Lambda \gg 1$ ). It is possible to define  $R_{c1}$  as the critical radius of curvature associated with the critical condition, so when  $R \ll R_{c1}$  the crystals can be considered strongly bent (Malgrange, 2002). On the basis of the dynamical theory of diffraction, the radius  $R_{c1}$  has been calculated as a function of energy over the range of interest in CDP Si and GaAs crystals (Fig. 3.1.6) in (220) and (111) reflections. This shows that the condition of strong curvature occurs for radii of several tens of metres, which are easy to obtain by the lapping process ( Chap. 4).

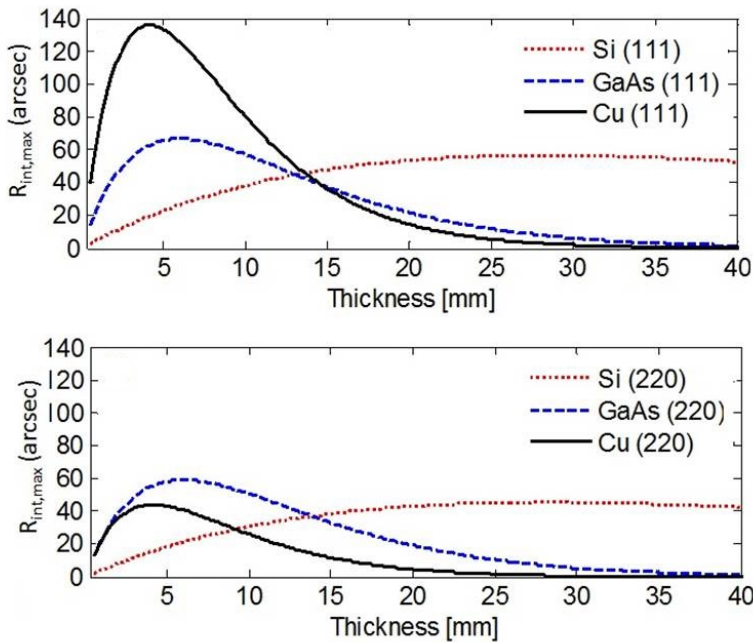


Figure 3.1.5: Integrated reflectivity as a function of the crystal thickness for  $E=140.5$  keV calculated for diffraction (111) and (220) for different materials of interest (top and bottom panels, respectively).

The condition  $\beta\Lambda = \pi^2$  gives a new critical value  $R_{c2}$  (see Fig. ) for which crystals achieve the maximum efficiency. Indeed, for radii of curvature  $R \ll R_{c2}$  the integrated intensity in equation 2.4.7 can be approximated with eq. 2.4.8 that corresponds to the maximum integrated intensity for CDP crystals. It no longer depends on the crystal curvature and coincides with the  $I_{\text{int}}$  of an ideal mosaic crystal.

## 3.2 Conclusion

It was found that CDP crystals with radii of curvature of several tens of meters can be considered as strongly bent crystals for X ray energies between 60 and 600 keV. In this case, a simplified approach for calculating the integrated reflectivity of the crystals is applied. Under this approximation, the maximum value of the integrated intensity is given by a crystal thickness  $t_{\text{max}} = \frac{1}{\mu}$ , as in the case of ideal mosaic crystals. Then, taking into account the absorption factor, it is found that Si, Ge and GaAs crystals with optimized thicknesses show a comparable or superior diffraction efficiency with respect to the heavier materials proposed previously. This is because the higher structure factor in

### 3.2. Conclusion

---

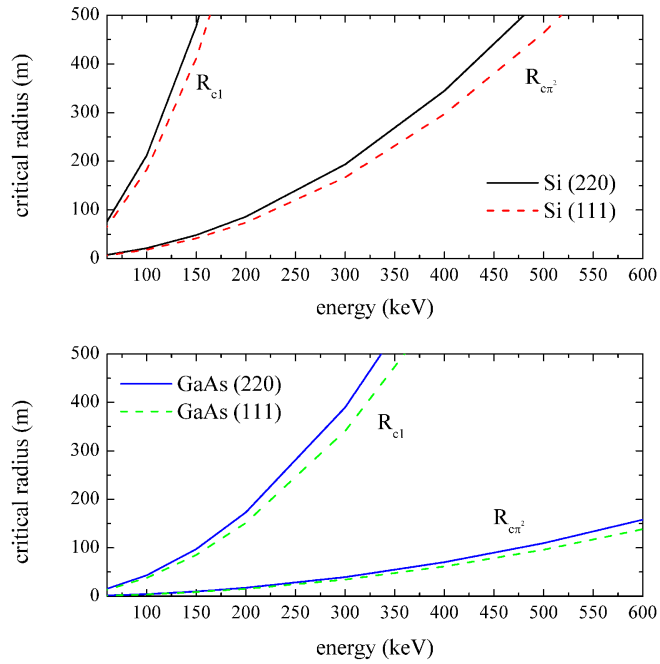


Figure 3.1.6: Critical radii of curvature  $R_{c1}$  and  $R_{c2}$  calculated as a function of energy for Si and GaAs (top and bottom panels, respectively), in the case of the (111) and (220) reflections.

heavier crystals is compensated by the larger values of optimized thickness in the Si, Ge and GaAs crystals.





## Chapter 4

# Bending technique

The use of bent crystals for X and  $\gamma$  rays energy applications has been extensively studied in the last decades. The manufacture of self-standing bent crystalline plates is a technological problem yet to be solved in a reliable way. To realize a Laue lens a huge number of bent crystals, with a uniform and well defined curvature is required. Mechanical holders are generally used for bending single crystals (Carassiti et al., 2010) but due to the weight and the space occupied, this technique is not suitable for settings with a large number of crystals. Thermal gradients (Smither et al., 2005), pressing crystals between curved surfaces (Smither et al., 2005), or strained film deposition (Virgilli et al., 2015) are others methods but in general they are too expensive in energy and material requirement. Malgrange *et al.* realized curved crystals by composition gradient in GeSi alloy crystals (Malgrange, 2002; Abrosimov 2005) but a large production can suffers by the difficulty in the crystal growth and the yield rate. Quite recently Guidi (Guidi et al., 2011) obtained curved crystals by grooving Si (111) wafers by a precise dicing saw. A diffraction efficiency of 88% for 150 keV photons is also reported (Barriere et al., 2010). The method is reproducible and the curvature can be established with accuracy, depending on the wafer thickness, density and depth of grooves. On the other hand the presence of a deep indentations removes a big volume of the crystal, reducing the hardness and the real thickness of the crystal causing the reduction of their diffraction efficiency. In this work the bending of crystals is realized by a controlled surface damaging (Buffagni et al., 2011), which introduces defects in a superficial layer of few tens nanometers in thickness causing an highly compressive strain. On the basis of results discussed in Chap. 3 , Si, GaAs and Ge are chosen as the best materials to get high diffraction efficiency. The GaAs crystals were grown by the Liquid Encapsulated Czochralski method, as described in (Ferrari et al., 2008). The slices are cut from the ingots perpendicularly to the growth direction and saw damaging were removed by a chemical etching with a HCl/HNO<sub>3</sub> 1:1 solution. The GaAs crystals are characterized by spontaneous formation of

"cellular structures" with dislocations distribution at the boundaries between perfect zones of the crystal. Because of the presence of cellular structures due to the Czochralsky growth, GaAs shows a natural degree of mosaicity with mosaic spread of 20-25 arcseconds measured at 8 keV. The Si and Ge crystals are commercial wafers. Moreover an innovative method of curving crystals has been developed during this work. It consists on a deposition of resin on one side of the wafer. During the polymerization, the resin induces a tensile strain on the substrate, causing the elastic bending of the slice. The lapping and the resin bending processes are described in details in this chapter.

## 4.1 Damaging technique

A simple method to obtain self-standing crystals with a reproducible and uniform curvature is based on controlled surface damage induced by a mechanical lapping process. Scratches, inclusions, and dislocations due to the treatment introduce defects in a superficial layer of the sample, causing an expansion of the crystal lattice and the bending of the sample, with convex curvature on the damaged surface. The polishing machine is a Buelher Ecomec 4 which allows to produce different deformations by changing some parameters as: the grit of the sandpaper, the pressure per unit area applied on the samples, the rotation speed of the sandpaper plate and the duration of the treatment. The independent rotation on two different axes of the sandpapers plates guarantee an uniform abrasion on the entire surface of the wafers. To evaluate the local and the mean curvature induced in the crystals, high resolution X ray diffraction measurements are performed in Bragg geometry by means of a X'Pert PRO Philips diffractometer, where the  $\text{CuK}\alpha_1$  radiation ( $\lambda=0.15405$  nm) is selected by four 220 reflections in germanium monochromators. The rocking curve peak shift as a function of the measurement position on the sample gives a direct measure of the sample curvature radius, as Fig. 4.1.1 reports.

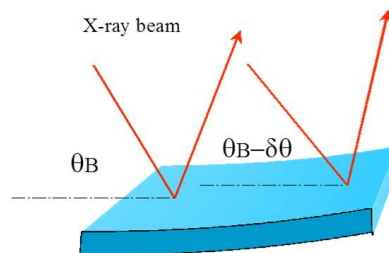


Figure 4.1.1: Scheme of the measurements for calculate the radius of curvature of crystal tiles. The Bragg condition varies along different positions on the samples.

Figure 4.1.2 shows the 004 Bragg diffraction profiles measured before and

#### 4.1. Damaging technique

after a treatment of 180 minutes with sandpaper P400, represented in the same scale for comparison. The mean curvature radius changes from about 480 m to 63 m, demonstrating the work of surface damaging process. The regularity of the peak shift means that the curvature is almost uniform along the sample.

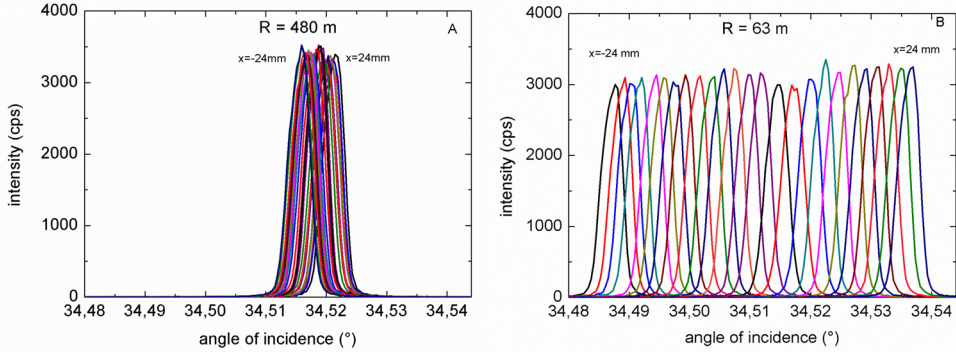


Figure 4.1.2: Si (100) sample. 004 Bragg diffraction peaks measured at 8 keV along a diameter of the sample. Rocking curves measured before (panel A) and after (panel B) a treatment 180 minutes long with sandpaper P400 on the same positions on the sample.

If the peaks position are shown as a function of the measurement positions, the uniformity of the curvature is immediately evident and the slope of the line represent the value of the radius of curvature. The 004 Bragg diffraction profiles have been collected with incident beam in different sample positions, along two directions perpendicular to each other and parallel to the wafer flats (x and y directions) for a Si (100) sample. The superposition of the measurements along the x e y directions means that the bending is practically spherical (Figure 4.1.3 *Left*). Moreover measurements performed impinging with the X ray beam on the front and rear surfaces of the same Si wafer (Figure 4.1.3 , *Right*) showed the curvatures are almost the same with opposite convexity. This confirms the curvature is a bulk property of the treated material.

For GaAs the values differ considerably along the different directions and in particular the value of the curvature at  $45^\circ$  is intermediate between the values at  $0^\circ$  and  $90^\circ$  directions, Fig. 4.1.4.

All analyzed GaAs samples presented similar behaviors, so it is possible to conclude that in GaAs samples the curvature seems elliptical. This effect is probably due to the elastic anisotropy characteristic of the GaAs crystals. To confirm the results, Ge (100) samples are bent with damaging technique and characterized during this work. The measurements performed along  $0^\circ$ ,  $45^\circ$  and  $90^\circ$  direction are superposed, underlining the spherical shape of curvature, see Fig. 4.1.5.

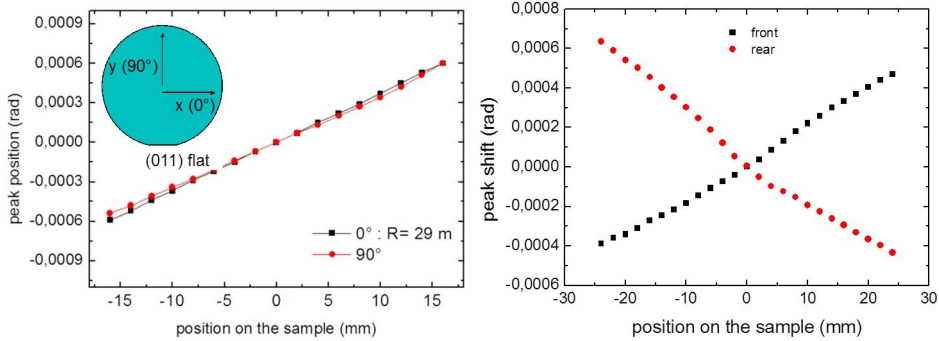


Figure 4.1.3: 004 diffraction peak shifts as derived from rocking curves measured in different points on the Si(100) sample. Measurements were performed along two different directions: x and y directions are along  $\langle 110 \rangle$  crystallographic directions (*Left*) and along the opposite sides of the slice (*Right*).

These results confirm that for Si and Ge, which have isotropic behavior, the curvature is spherical, while for GaAs it is elliptical. The study of the lapping curved samples in term of stress and line tension are reported in (Buffagni et al., 2011). The most important results are:

- fixed the grain size of the sandpaper, the line tension as a function of the treatment duration remains almost constant in a time range between 30 sec to 5 min. This means that the strain is induced in the crystals in the first tenths of seconds of the lapping process. On the other hand, the curvature radius increases due to the substrate thickness reduction;
- fixed the time of the treatment for 1 min, the samples were treated with different sandpapers (from P180 to P4000), corresponding to different grain dimensions. The radius of curvature decrease increasing the grain dimension of the sandpaper.

## 4.2 Resin deposition technique

For the first time an innovative and simple method to realize self-standing curved crystals is presented in this work. The capacity of the resins to bent substrates of some materials is well known in particular in wood and mechanical industry. The bending process developed is based on the idea to take advance of this capacity of the resin and try to maximize this effect. Some epoxy resins are chosen and texted because their characteristic. They allow to obtain a layer resistant to external mechanical strains and they have a good adherence to different materials as metallic or organic substrate. The process consists on a

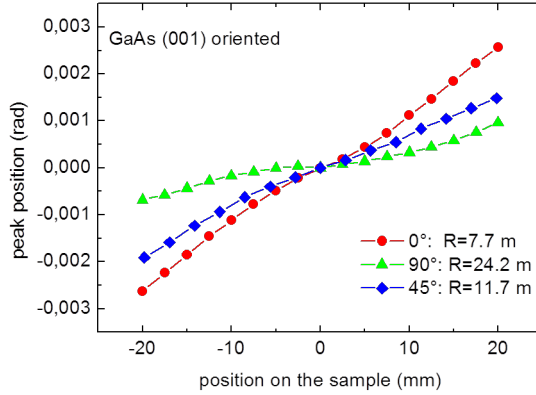


Figure 4.1.4: 004 and 404 peaks reflection as a function of a GaAs (100) sample position along  $0^\circ$ ,  $45^\circ$  and  $90^\circ$  directions. The value of curvature along the different directions are reported.

film deposition of selected bi-component epoxy resin on one side of crystals (Fig. 4.2.1 *Left*) and it is made rather uniform by mean of a spin-coater. During the polymerization, the resin induces tensile strain that can cause the bending of the substrate, with concave curvature on the side of the resin deposition (Fig. 4.2.1 *Right*).

Several Si and GaAs samples with different thicknesses were treated to study the effect of this new technique. High resolution X ray diffraction measurements were performed in Bragg geometry by means of a X'Pert PRO Philips diffractometer to evaluate the local and the mean curvature induced. The 004 Bragg diffraction profiles have been collected with radiation beam incident in different sample position, along two directions perpendicular to each other and parallel to the wafer flats (x and y directions), before and after the treatment. Fig. 4.2.2 shows the rocking curves measured on a Si sample before (*Right*) and after a treatment (*Left*). The shift of the Bragg peak as a function of the position of the sample means a change in curvature radius from about 400 m to 3 m, demonstrating that the glue process is effective to bend crystals. Systematic studies of the effects of the spin coater speed at a fixed time are carried out on one series of 10x10 mm<sup>2</sup> of Si (100) 0.75 mm thick.

The speed of the spin-coater determines the thickness of the film of glue and the effect on the radius of curvature is evident, see Tab. 4.1.

It is possible to represent the radius of curvature by the relation of the shift of the Bragg peak as a function of the positions on the sample in which the measurements are performed, Fig 4.2.3 *Right* reports this measurements for the samples reported in the Tab. 4.1. It is evident the changes in the value of the

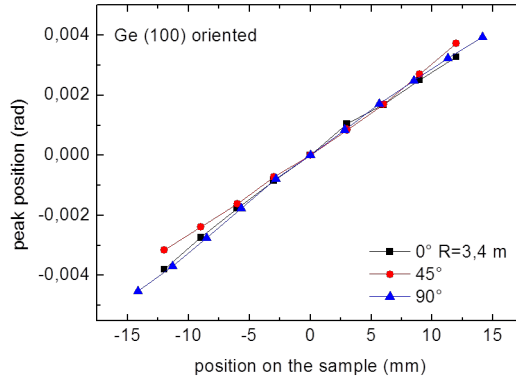


Figure 4.1.5: 004 and 404 peak shift as a function of a Ge(100) sample position along 0°, 45° and 90° directions. The value of curvature along the different directions are reported.

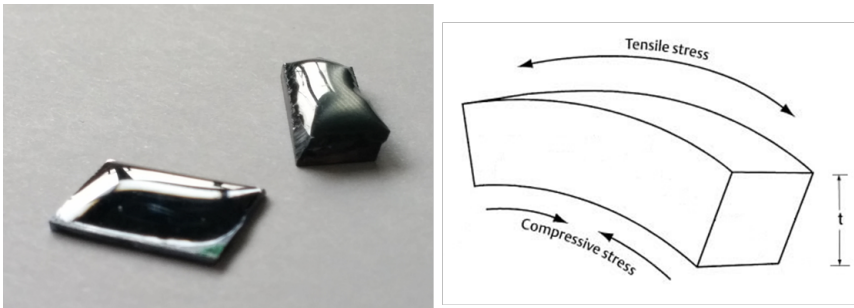


Figure 4.2.1: *Left*: Two tiles of Si of 0.75mm and 2 mm treated with glue deposition. *Right*: Scheme of substrate bending

radius of curvature, changing the slope of the function. In Fig. 4.2.3 *Left* the dependence of the radius of curvature with the spin-coater speed is represented.

As for the damaging technique, the 004 diffraction peaks were collected along two perpendicular directions (called x and y) to check the shape of the curvature. Measurements performed on a Si(100) sample showed a uniform and spherical bending (Figure 4.2.4 *Left*). Moreover measurements performed impinging with the X ray beam on the front and rear surfaces of the same Si wafer (Figure 4.2.4 *Right*) showed the curvatures are almost the same with opposite convexity, confirming that the curvature is a bulk property of the crystals.

As already discussed in Chap. 3, the optimization of the thickness of crystal is important in order to maximize the reflectivity efficiency. So one of the most important characteristic for a suitable bending process is the capability of

## 4.2. Resin deposition technique

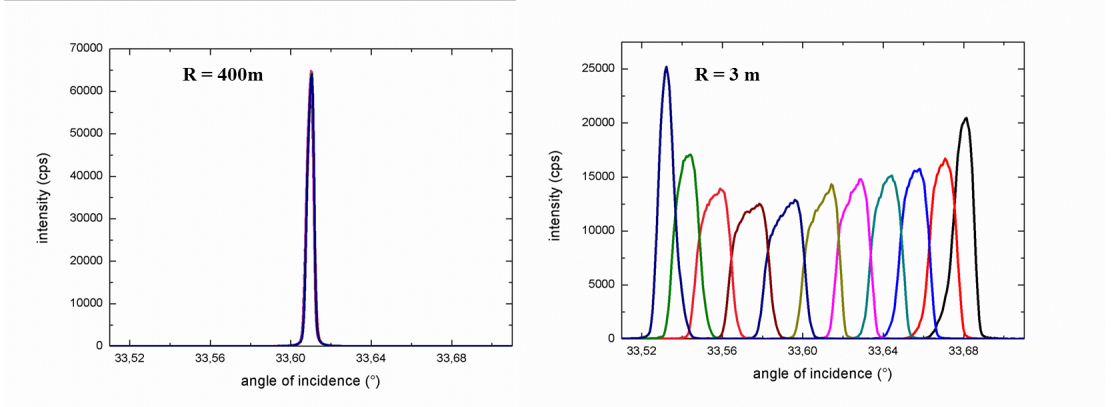


Figure 4.2.2: Rocking curves measured on a Si(100) sample before (*Left*) and after the resin deposition (*Right*).

| Spin-coater speed (rpm) | Radius of curvature (m) |
|-------------------------|-------------------------|
| 4800                    | flat                    |
| 4000                    | 250                     |
| 2000                    | 120                     |
| 1100                    | 65                      |
| 500                     | 13                      |

Table 4.1: speed of spinning and the curvature radii as derived from the 004 diffraction peak positions (unless differently specified) are reported in the columns 1 and 2 respectively. Several Si (100) of 0.75mm in thickness and with an area of 1x1 cm<sup>2</sup> are treated.

bending thick crystals. This is nowadays an open issue. To test this capacity of the resins deposition technique, some 2 mm thick Si (100) samples are treated and characterized. Fig. 4.2.5 reports the 004 peak shift as a function of sample position measured along two perpendicular directions (*Left*) and on opposite sides of a treated Si crystals (*Right*); the radius of curvature is  $\sim 14 \text{ m} \pm 0.5 \text{ m}$  along the x e y direction and in front and rear side.

These results confirms that the resins technique is a good process to realize self-standing curved crystals also rather thick, with uniform curvature along the whole area of the sample. Rocking curves as a function of the measurement position were collected also for several GaAs samples with 2 mm thickness. Examples of the peak shift are reported in Figure 4.2.6: the 004 diffraction peaks were measured along the x and y directions of a GaAs sample to check the shape and the uniformity of the curvature. The curvature radii derived are equal within the experimental error, so the curvature has a spherical shape. This means that resin process is suitable to bent GaAs sample and that it is

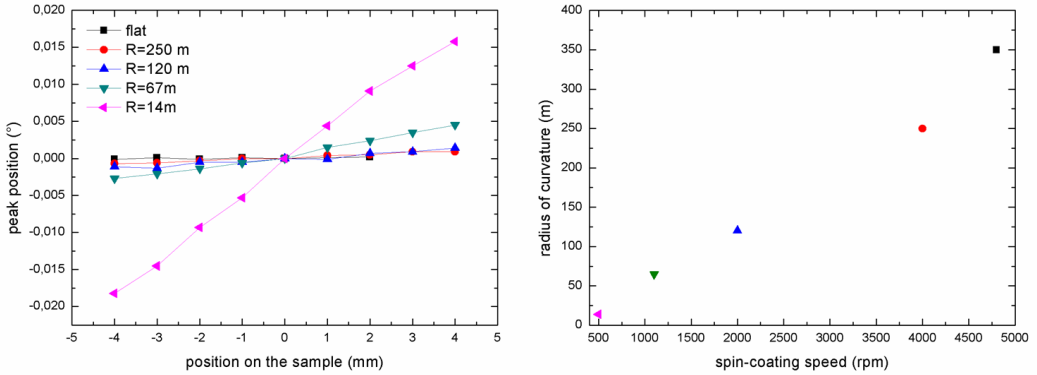


Figure 4.2.3: *Left*: peak shift as a function of a Si (100) samples treated with glue deposition, changing the speed of spun-coating. *Right*: The values of curvature as a function of spin-coating speed are reported.

possible to achieve also a spherical curvature.

In order to achieve a stronger curvature in thick ( $>2$  mm) crystals, some GaAs samples with  $t=2$  mm are treated with a combination of these 2 process. First GaAs crystals were lapped for 5 min with sandpaper P80 and then a film of epoxy resins is deposited with spin-coater speed of 1000 (rpm). The result is illustrated in Fig. 4.2.7: a change in the radius of curvature from about 60 m to 6 m along x direction and from 120 to 7 m along y direction is evident. It is important to note that starting from an elliptical curvature in GaAs induced by the damaging technique, the resin technique can bent the sample achieving a spherical curvature shape. This result suggests the idea that is possible to combine the two process to get strongly bent crystal rather thick.

To check the stability of the curvature in time, the characterization of the samples' curvature are performed after 1 month. In Fig. 4.2.8 the radius of curvature changes from 5 m to 24 m but the spherical curvature, confirmed by a good superposition in x e y direction of the 004 measurements, remains.

This result suggest a relaxation of the force that the film induces on the substrate, causing the reduction of curvature. To optimize the resin deposition process and the combination of it with the damaging technique, other test and studies are necessary.

### 4.3 Conclusion

In this chapter the damaging bending technique mainly used during my work is described. It consist in introducing an in plane surface strain by damaging one side of the crystal with sandpapers of different grain sizes. The damage and the strain introduced by the surface treatment are reproducible, uniform



### 4.3. Conclusion

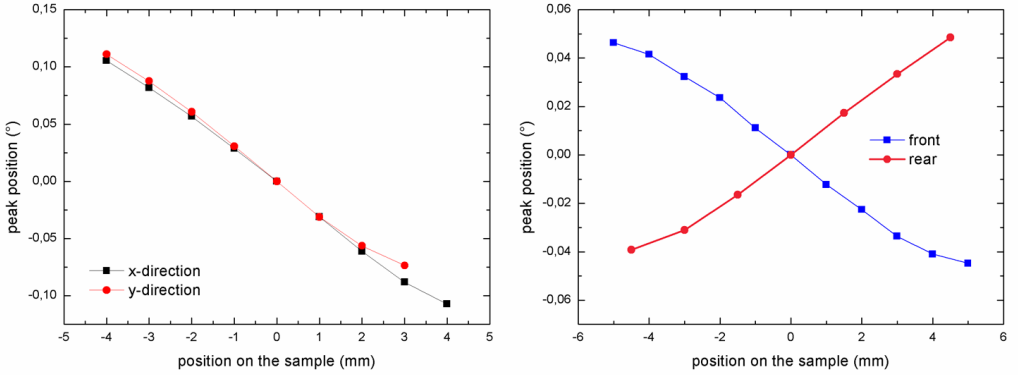


Figure 4.2.4: 004 diffraction peak shifts as derived from rocking curves measured in different points on the Si(100) sample of 0.75 mm thick treated with the resin deposition. Measurements were performed along two different directions:  $0^\circ$  and  $90^\circ$  directions (called x and y direction) are along  $\langle 110 \rangle$  crystallographic directions (*Left*) and along the opposite sides of the slice (*Right*).

and depend mainly on the type of used paper, i.e. larger grains introduce a larger stress and a lower curvature radius. Another new bending technique is developed and the main results are shown. The process consists on a film deposition of a selected bi-component epoxy resin on one side of crystal, made uniform in thickness by mean of a spin-coater. During the polymerization, the resin induces a tensile strain that causes the bending of the substrate, with concave curvature on the side of the resin deposition. It was demonstrated that choosing the speed of spin-coating, so changing the thickness of the film, a control of radius of curvature can be obtained. Measurements performed on curved Si(100) and GaAs(100) samples with 0.75 mm and 2mm thick, along two perpendicular directions show a spherical and uniform curvature. Moreover measurements performed on the front and rear surfaces of the same Si wafer showed the curvatures are almost the same with opposite convexity, confirming that the curvature is a bulk property of the treated material. Finally it was demonstrated the possibility to combine the two bending technique to obtain curved crystal with a stronger curvature in rather thick crystals. These results lead to the conclusion that the resin deposition technique is a suitable process to realize curved crystal that can be used as optical focusing element for X and  $\gamma$  ray applications.

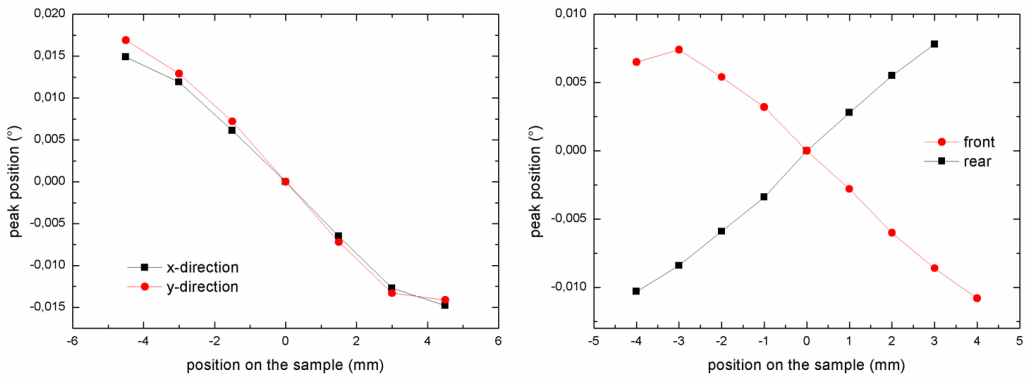


Figure 4.2.5: 004 diffraction peak shifts as derived from rocking curves measured in different points on the Si(100) sample 2 mm thick treated with the resin deposition. Measurements were performed along two different directions:  $0^\circ$  and  $90^\circ$  directions (called x and y direction) are along  $\langle 110 \rangle$  crystallographic directions (*Left*) and along the opposite sides of the slice (*Right*).

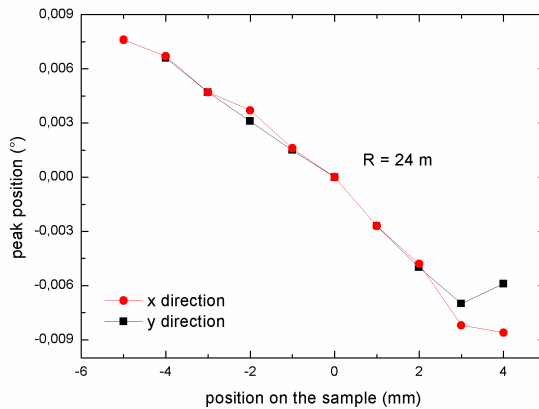


Figure 4.2.6: 004 peak shift as a function of sample's position measured along two perpendicular directions called x e y, for a GaAs crystal with 2 mm in thickness.

### 4.3. Conclusion

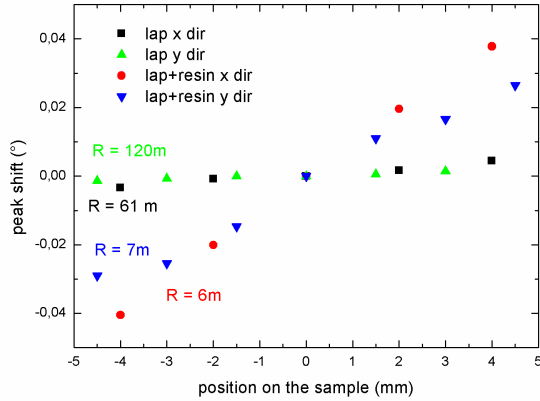


Figure 4.2.7: 004 peak shift as a function of sample's position measured on a GaAs crystal with 2 mm in thickness. The sample is curved with damaging technique (black and green points) and after treated with resin deposition (blue and red points).

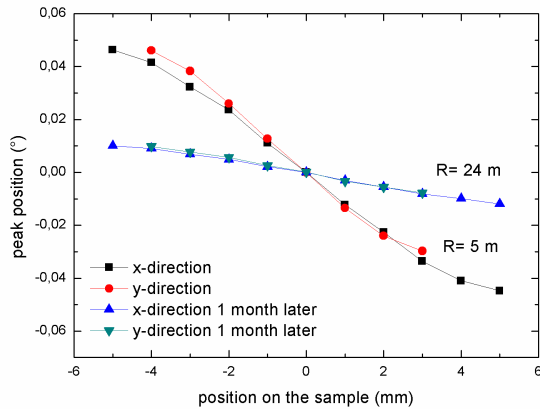


Figure 4.2.8: 004 diffraction peak shifts measured in different points on the Si(100) sample treated with the resin deposition. Measurements were performed along two different directions: (called x and y direction) at 1 month distance.



# Chapter 5

## Experimental results

In order to verify the results of simulations of the crystal diffraction efficiency in Chap. 3, detailed characterization at low and high X ray energies are performed on flat and bent crystals obtained with the damaging and the resin deposition technique, described in Chap. 4. Thanks to the access at the European facilities as ILL and ANKA synchrotron, it was possible to perform a quantitative study of the diffraction efficiency of crystals with different thickness at different geometries, in the energy range of interest. The description of the facilities are reported in App. C.

### 5.1 Low energy

Several GaAs and Si curved with damaging and flat crystals were measured in Laue and Bragg geometry at energies of 17, 19, 22.5 and 59 keV. Laue 220 symmetrical and 202, 111 asymmetrical diffraction profiles (see Fig. 5.1.1 for the measurement schemes) in Si crystals have been measured with the MoK $\alpha$  radiation (E=17 keV) in a double crystal diffractometer (Si (220) monochromator) in non-dispersive configuration (see App. C for the detailed description). The line source of a fine focus Mo tube was selected so that the beam cross section in the scattering plane was approximately 50  $\mu\text{m}$ . Diffracted and transmitted X ray diffraction profiles in Laue geometry have been also calculated on the basis of the dynamical theory for comparison (Hirsch 1952). The 220 symmetrical Laue profiles of (001) oriented Si and GaAs samples were also measured at the LARIX facility of the Physics Department of Ferrara University using the W K line (E = 59 keV). Owing to the lack of a monochromator crystal, only the integrated intensity could be measured. Moreover the 220, 202 and 111 reflection in Si 0.75mm thick flat and bent are studied in detail at 19 and 22.5 keV at ANKA synchrotron facility.

The 220 symmetrical reflectivity and transmissivity diffraction profiles of a

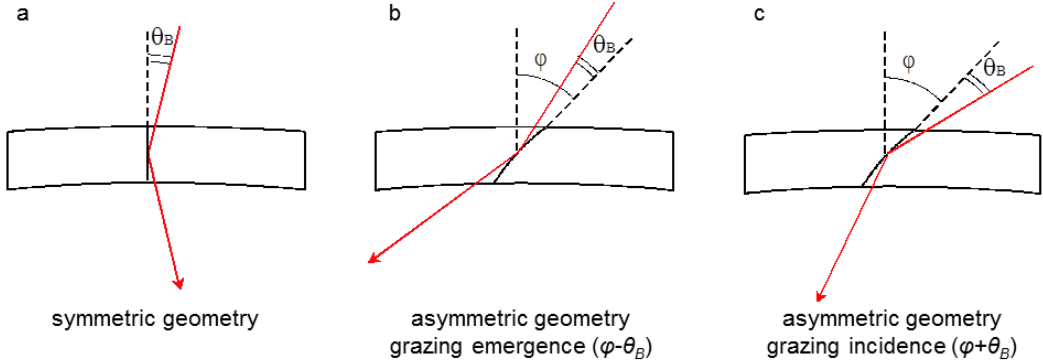


Figure 5.1.1: Geometry of the Laue diffraction with symmetric (a) and curved asymmetric (b and c) diffracting planes. In the last case the incidence angle is  $\varphi - \theta_B$  (grazing emergence, panel b) or  $\varphi + \theta_B$  (grazing incidence, panel c)

Silicon (001) oriented flat crystal of  $750\ \mu\text{m}$  in thickness at  $E = 17\ \text{keV}$  (MoK $\alpha$ 1 line) are reported in Fig. 2 *Left* and compared to the simulated profiles from the dynamical theory of X ray diffraction. The integrated reflectivity agrees within 7% with the value calculated from theoretical profile, confirming the validity of the model. A well pronounced Borrmann effect (par. 2.2.7) is observed in the transmission profile as an indication of the crystal perfection.

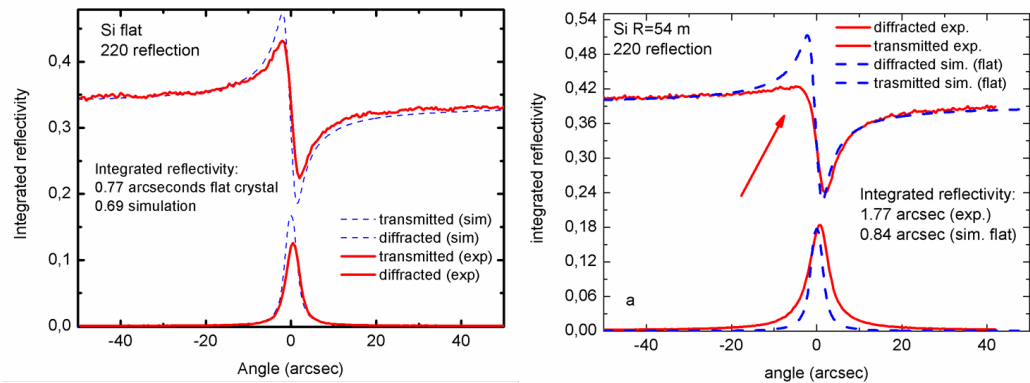


Figure 5.1.2: MoK $\alpha$  220 reflection for flat (*Left*) and bent crystals with  $R = 54\text{m}$  (*Right*) diffraction and transmission profiles (red solid curves) for a  $750\ \mu\text{m}$  thick Si crystal. Theoretical profiles (dashed blue lines) calculated for a flat crystal on the basis of the dynamical theory (see par. 2.2.6) are added for comparison. The experimental and calculated integrated reflectivity are reported.

In Fig. 5.1.2 the (220) symmetrical Laue transmission and diffraction profiles of a bent Si crystal, with a radius of curvature of 54 m are compared with flat simulated profiles. Contrary to what is expected in perfect slightly bent

crystals, in which the excited Bloch wave at the Bragg condition follows the curvature of the lattice planes (Authier, 2001), in the 54 m curved Si sample the Borrmann effect is almost completely quenched (Fig. 5.1.2 *Right*). Moreover, we observe an increase of the integrated reflectivity of more than two times with respect to that of the perfect crystal, in contrast to the results reported by (Kalman and Weissmann, 1979) and the vanishing Bragg angle variation  $\Delta\theta$  as calculated from formula (3.1.2) in the case of Laue symmetrical geometry on elastically bent Si (001)-oriented crystals. The calculated broadening of the diffraction profile due to the beam cross section ( $\sim 0.19$  arcseconds) is almost negligible with respect to the observed peak width.

The increase of the diffracted intensity in symmetric Laue geometry has been observed in curved crystals with specific surface orientations, such as 111 Laue diffraction in  $(1\bar{1}0)$  oriented Si surfaces (Janacek et al., 1978) or 422 diffraction in  $(\bar{1}11)$  oriented samples (Kalman and Weissmann, 1983). In fact, because of the elastic deformations along these non-symmetric crystallographic directions, a secondary curvature is induced in the lattice planes perpendicular to the sample surface. A possible origin of the increase of the integrated intensity in symmetric Laue geometries for surface-damaged crystals may be in the irregular elastic field at the sample surface, due to the surface damage. 004 Bragg reflection measurements performed in a double-crystal arrangement in the non-dispersive setting on both the damaged and the perfect side of the curved sample (Fig. 5.1.3) confirm this hypothesis, with a much larger diffracted intensity obtained from the damaged side. The peak broadening and the peak splitting seen in the profile measured on the perfect side are due to the curvature of the sample and the larger beam footprint in the Bragg geometry, leading to a shift of the Bragg condition of the Mo K1 and Mo K2 lines. This does not affect the integrated reflectivity measurement. A similar result in term of an increased integrated intensity was found in as-cut Cu crystals for neutron monochromators (Courtois et al., 2005) in Laue diffraction geometry. In the present case the observed peak broadening and increase of the diffraction efficiency is not detrimental for the Laue lens application for focusing hard X rays.

In Fig. 5.1.4 the 202 asymmetrical Laue transmission and diffraction experimental profiles corresponding to an angle of incidence  $\varphi - \theta_B = 45^\circ - 10.63^\circ$  is reported. Due to the lattice plane bending an increase of 3.3 times of the diffracted integrated intensity and a FWHM of the diffraction peak of nearly 6 arcseconds with respect to the flat crystals is observed as expected from theory due to the curvature of diffracting planes.

In the case of weak bending ( $\beta\Lambda < 1$ ) as in the case of a bent crystal with a radius of curvature  $R=54$  m at  $E=17$  keV the integrated reflectivity  $R_{int}$  of the diffracted profile of bent perfect crystals is proportional to  $1/R$  following the slope (Kalman and Weissmann, 1983; Erola et al., 1990)

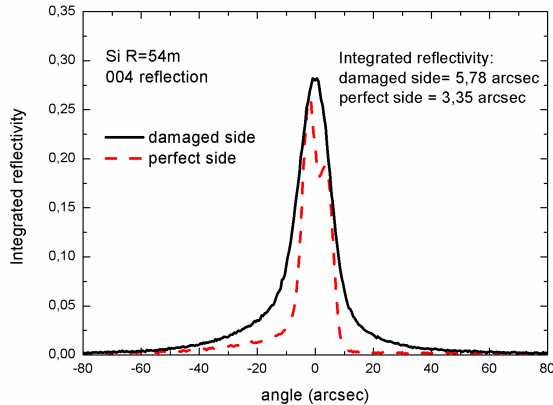


Figure 5.1.3: Comparison between 004 Bragg diffraction profiles measured on the perfect (dashed line) and damaged side (solid line) of an Si crystal with a curvature radius of 54 m.

$$R_{\text{int}} \propto \frac{1}{R} \frac{\left( e^{-\frac{\mu t}{\gamma_g}} - e^{-\frac{\mu t}{\gamma_0}} \right)}{\mu \left( 1 - \frac{\gamma_0}{\gamma_g} \right)} \quad (5.1.1)$$

where  $\mu$  is the linear attenuation coefficient,  $\gamma_0$  and  $\gamma_g$  are the director cosines of incident and diffracted beams with respect to the surface normal directed inside the crystal, respectively. It is worth noting that for symmetrical geometry  $\gamma_0 = \gamma_g$  so that  $R_{\text{int}}$  is independent from curvature, as expected from theory. The dependence of the experimental integrated reflectivity as a function of  $1/R$  are reported in Fig. 5.1.5 *Left* and compared with the expected dependence valid for weak curvatures, eq.5.1.1. Flat and bent crystals ( $R= 54$  m and  $R = 29$  m) are measured. In all the measurements performed, included those in symmetrical Laue geometry, the integrated reflectivity follows a linear dependence with curvature but with larger values than the expected theoretical.

The 220 measurements on the same crystals are performed also at 59 keV at Larix facility. Figure 5.1.5 *Right* shows the integrated reflectivity as a function of the radius of curvature in the case of Si samples ( $E=59$  keV). Also in this case the experimental values exceed the theoretical ones.

To better understand the trend of the diffraction efficiency of bent crystals in the region of weak and strong bending, a detailed study was realized at beamline PDIFF in ANKA synchrotron facility. Five Si (100) samples are measured (1 flat and 4 bent crystals with a radius of curvature from 54 m to 2 m obtained with damaging technique) in 220 symmetrical geometry and 202, 111 asymmetrical geometry at 19 and 22.5 keV. Due to some technical



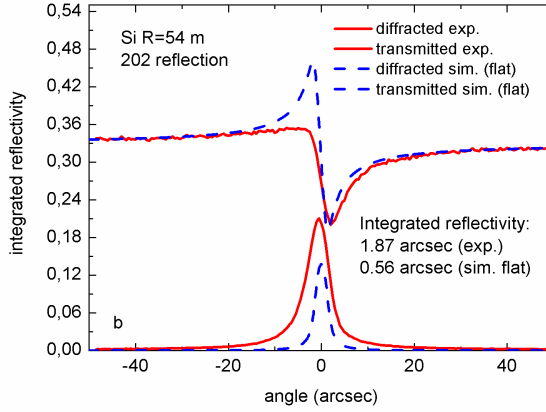


Figure 5.1.4: 202 diffraction and transmission (red solid curves) profiles measured on a  $670\ \mu\text{m}$  thick and bent ( $R=54\ \text{m}$ ) Si crystal with MoK $\alpha$ 1 line. Theoretical profiles (dashed blue lines) calculated for a flat crystal on the basis of the dynamical theory are added for comparison. The experimental and calculated integrated reflectivity are reported.

problems it was not possible to measure the incident beam intensity, so it is not possible to compare the experimental values with theory but it is only possible to observe the dependence of integrated intensity with radius of curvature. Fig. 5.1.6 reports the slope of the integrated intensity with  $1/R$ . A good agreement between the measurements (red dots) and the theoretical behavior (blue line) is observed.

The three different bending regions are evident : in the first one the integrated intensity increases linearly with the curvature corresponding to the weak bending region ( $\beta\Lambda < 1$ ) and achieving a maximum in region of strong curvature. The region of strong curvature is the most interesting because for energies  $E > 100\ \text{keV}$  a crystal with moderate bending  $R < 50\ \text{m}$  can be considered as strongly bent. Moreover for bent crystals with a radius of curvature above a critical value, the integrated efficiency is almost constant.

Thanks to these measurements it is possible to conclude that the damaging bent crystals can be described as ideally bent.

The increase of the integrated intensity in the 220 geometry is also evident in the measurements at 19 and 22.5 keV, confirming the idea that this effect does not depend on the experimental set up, but is an intrinsic phenomenon of surface damaged bent crystals.

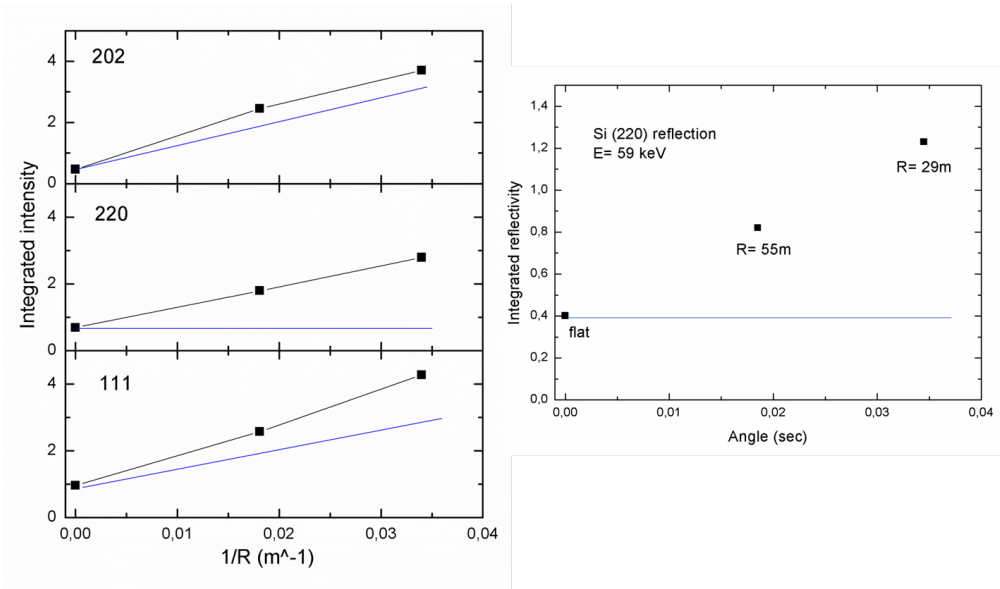


Figure 5.1.5: *Left*: Experimental integrated reflectivity of a flat and two surface damaged weakly bent Si crystals ( $R = 29$  and  $55$  m) measured at  $E = 17$  keV in (202), (220) and (111) geometry. *Right*: The values are reported as a function of crystal curvature  $1/R$  compared to the linear increase given by formula 5.1.1 (blue lines) at  $E = 59$  KeV.

### 5.1.1 Preparation of thicker diffracting elements

The efficiency of a Laue lens for X and  $\gamma$  ray focusing is closely linked to the diffraction efficiency of the single crystals composing the lens. As already discussed in Chap. 3, a fundamental parameter in order to increase the performances of the lens, is the thickness of optical elements. In the surface damaging process, due to the limited value of the strain and of the thickness of the damaged zone obtained, the dimension  $h$  (see a schematic representation in Fig. 5.1.7) of the crystal plate cannot exceed few millimeters for radius of curvature down to  $50$  m.

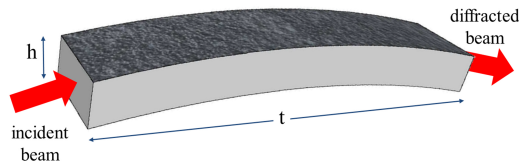


Figure 5.1.7: A schematic diagram of a bent crystal in the Laue diffraction geometry. The damaged surface is the upper one, parallel to the CDPs and perpendicular to  $R$ .

## 5.1. Low energy

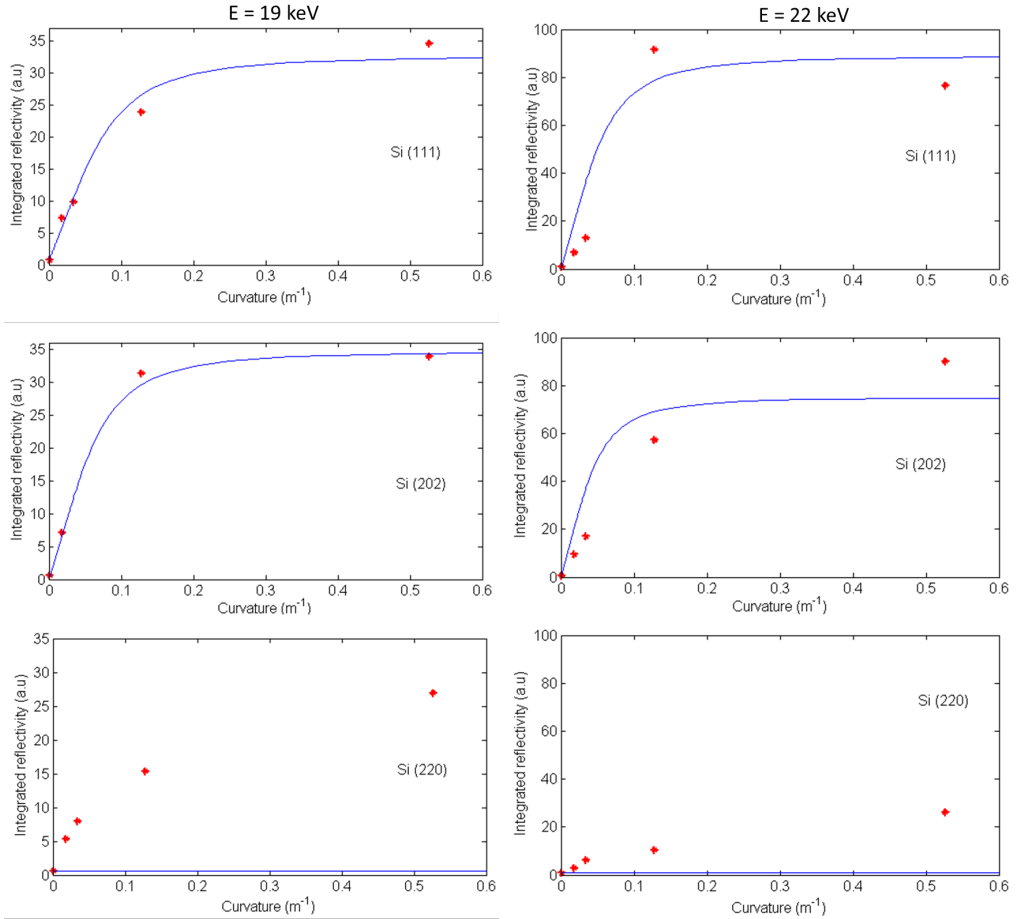


Figure 5.1.6: Integrated intensity of flat and bent crystals (red dots) as a function of curvature at 19 and 22 keV. Theoretical profiles (blue lines) calculated on the basis of eq. 3.1.8 are added for comparison.

A possibility to overcome such limitations is stacking CDP crystals to obtain thicker crystal elements. This method was already proposed for neutron monochromators (Frey, 1974; Alianelli et al., 2004 and references therein), but in this case the difficulty to achieve a good alignment among crystal elements can induce a limitation in the performance of the monochromators. Indeed, a little misalignment may cause different Bragg conditions on the selected diffracting planes producing multiple diffraction peaks and a broadening of the image in the focal plane of the Laue lens.

A fine control of the value of the curvature, the stability of the curvature of the tesserae under stress and the uniformity of the thickness  $h$  are mandatory. To achieve an accurate lattice plane alignment, the stack was realized with

crystals coming from the same wafer and having exactly the same orientation. Moreover, it is extremely important to get a very uniform surface grinding, since an error in the thickness  $h$  of only 1.5% over the entire area may induce a misalignment of hundreds of arc seconds. A stack of two Si (001) CDP tiles with dimension  $28 \times 8 \times 0.5 \text{ mm}^3$  and radius of curvature  $R = 2 \text{ m}$  was realized. The high curvature value is necessary to reach the strongly bent regime even at the low X ray energies available for the characterization measurements. The alignment of the elements was investigated with an incident beam  $0.5 \times 0.5 \text{ mm}^2$  of 19 keV at the PDIFF beamline of the ANKA Synchrotron Radiation Facility (Karlsruhe, Germany) in two different reflections, (111) and (220), and different positions on the tile. Figure 5.1.8 shows a single and well-defined peak under X ray diffraction, underlining that the plates are sufficiently aligned to behave like a single crystal.

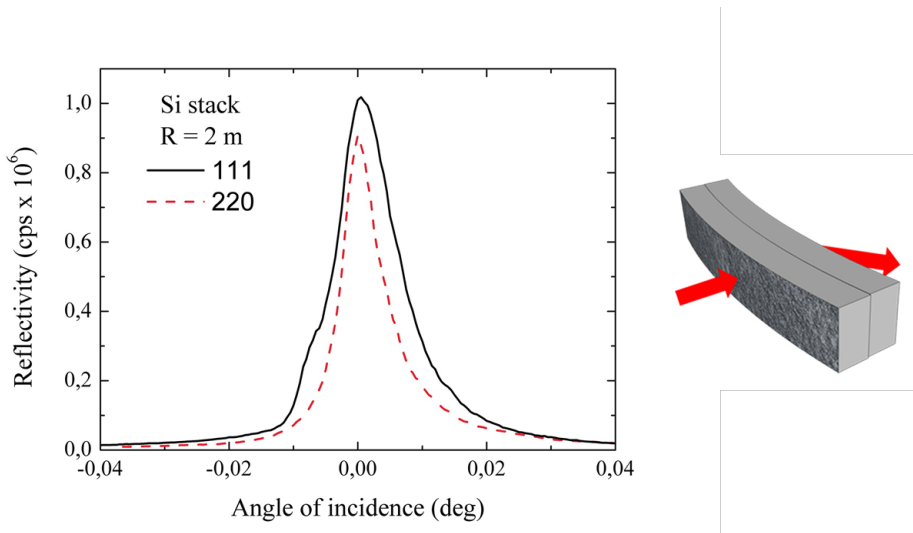


Figure 5.1.8: *Left*: Diffraction profiles of a stack of curved (001) Si crystals measured at 19 keV at the ANKA synchrotron for the 111 and 220 reflections (black and red lines, respectively). *Right*: The geometry of the diffraction experiment.

A similar result was obtained by (Neri et al., 2013) with indented Si crystals but with lower curvature values; unfortunately in that case during the indentation bending technique a large part of the crystal was removed, reducing the hardness and the real thickness of the crystal. It is possible to conclude that the surface damage bending technique is the most suitable to realize stacked optical elements.

## 5.2 High energy

A detailed study of the integrated intensity as a function of energy in the energy range of interest ( $100 \div 350$  keV) was performed at ILL in the hard X ray facility. Flat and bent Si (100) crystals with dimensions  $10 \times 10 \times 0.75$  mm<sup>3</sup>, realized with damaging and resin deposition technique, are analyzed. The experimental set-up is designed in order to focalize on the detector all the diffracted beam coming from a flat perfect crystals (see Appendix C).

The integrated intensity is calculated by evaluation of the integral under the diffraction profile obtained by the diffracted image. Due to some experimental limitations it was not possible to measure the incident beam intensity, so the  $I_{\text{int}}$  values are not absolute, but their trend is a significant result. The study of the trend of  $I_{\text{int}}$  as a function of energy for curved crystals obtained with lapping technique, in symmetrical (220) and asymmetrical (111) geometry is shown in Fig. 5.2.1 Up and Bottom respectively. Three samples: 1 flat and 2 bent with radius of curvature 54 m and 29 m are measured. The unexpected increase in diffraction efficiency of bent crystals with respect to the flat one in symmetrical geometry of more than 3 times is evident and underlined by the green vector. This result is already observed in measurement performed at low energy (previous sec.), confirming again that this effect is not due to the set-up but it is an intrinsic property of the samples. A gain in diffraction efficiency of about 12 time is calculated for bent crystals in asymmetrical 111 geometry, verifying that in this geometry bent crystal are much more efficient than flat crystals due to the bending of diffracting planes, as expected from the theory.

It must be noted that the  $I_{\text{int}}$  decreases increasing the energy, as expected from the eq. (3.1.4) where it is evident that  $I_{\text{int}}$  is proportional to  $\lambda^3$ . Moreover in 111 geometry, above a 200 keV bent crystals with different curvature tend to have the same value of efficiency, and above 300 keV bent crystals tend to have the same diffraction efficiency of flat crystal. A similar behaviour was measured in imperfect copper crystals measured at different  $\gamma$  rays energies [Authier and Malgrange, 1998], Fig. 5.2.2.

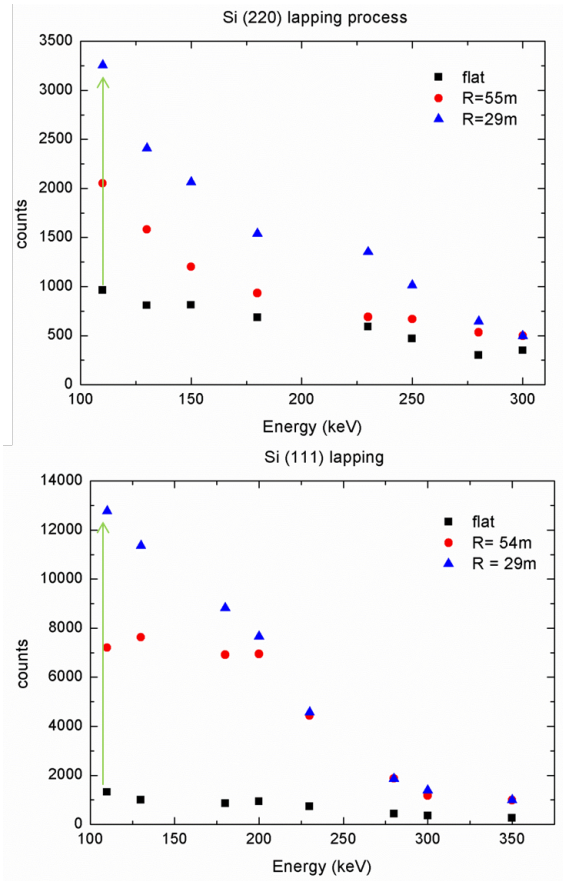


Figure 5.2.1: Trend of the integrated intensity as a function of energy in a flat and two bent ( $R = 54$  ,  $29$  m) Si crystals, realized with the damaging technique. Up: the symmetrical diffracting geometry 220; Bottom: the asymmetrical diffracting geometry 111.

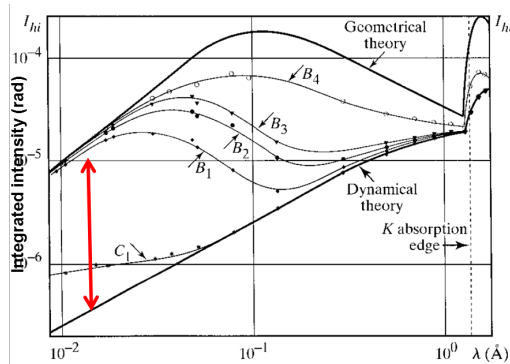


Figure 5.2.2: Integrated intensities of diffraction profiles for 5 copper crystals with X ray wavelength from 0.01 to 3 Å (From [Authier and Malgrange, 1998]).

This result can be understood considering the study of integrated reflectivity reported in Chap. 2. Indeed crystals with radius of curvature above the critical radius  $R_{c\pi^2}$  can be described as ideally mosaic crystal (par. 3.1.4) and the  $I_{\text{int}}$  is reported in eq. (3.1.4). As Fig. (3.1.6) shows, for very high energies, the value  $R_{c\pi^2}$  became very big, so also nearly flat crystals or with very weak curvature can be considered by the X and  $\gamma$  ray as strongly bent, and they reach the value of the  $I_{\text{int}}$  of ideal mosaic crystals.

To verify these considerations, the same study of integrated intensity as a function of energy in the range (100 ÷ 350 keV) is performed in bent crystals realized with resin deposition technique at symmetrical and asymmetrical geometry, Fig. 5.2.3 Up and Bottom. It is evident the same unexpected increase of integrated intensity for bent crystals for the 220 reflection and, at the same time, also the expected increasing in the 111 reflection is evident. The decrease of the diffracted intensity increasing the energy occurs also in this case. Finally, it is possible to observe the same behavior of bent and flat crystal above 200 keV and 300 keV described before for the lapping curved crystals. Because CDP crystals realized with resin deposition technique can be considered as ideally curved crystals, and because the damaging bent crystals behave as resins bent crystals, it is possible to conclude that also CDP damaged crystals behave as ideally curved crystals.

## 5.3 Conclusion

Several GaAs and Si flat and CDP crystals realized with damaging technique were measured in Laue geometry in symmetrical (220) and asymmetrical (202) and (111) geometries at low energies of 17 and 59 keV. The diffracted and transmitted X ray diffraction profiles are also calculated, for comparison, on the basis of the dynamical theory (Hirsch, 1952). An expected increase of diffraction efficiency in CDP crystals with respect to the flat ones is observed in asymmetrical diffraction geometry. Also an increase of the integrated intensity of curved crystals in symmetrical geometry is observed, not predicted by the theory.

To better understand the trend of the diffraction efficiency of CDP crystals in the region of weakly and strongly bending, a detailed study was realized at low energy (19 and 22 keV) at beamline PDIFF in ANKA synchrotron facility. Five Si (100) samples flat and bent, obtained with lapping process with different radius of curvature, are analyzed in 220 symmetrical geometry and 202, 111 asymmetrical geometry. The experimental trend of  $I_{\text{int}}$  is in a good agreement with that predicted by the theory, so it is possible to conclude that the damaging bent crystals can be described as ideally bent. The increase of the integrated intensity in the 220 geometry is evident also in these measurements, confirming

that this effect does not depend on the experimental set up, but is an intrinsic property of surface damaged bent crystals.

A study of the integrated intensity as a function of the energy in the energy range of interest ( $100 \div 350$  keV) is performed at ILL in bent crystals realized with damaging and resin deposition technique at symmetrical and asymmetrical geometry. A gain in diffraction efficiency of about 12 times is observed for bent crystals in asymmetrical 111 geometry, confirming that in this geometry bent crystals are much more efficient than flat crystals due to the bending of diffracting planes, as expected from the theory. The value of the diffraction efficiency of curved crystals realized with both techniques tends to coincide with that for flat crystals at very high energy ( $> 200$  keV). These results suggest that at very high energy, nearly flat crystals have a curvature larger than the critical value and are seen by the radiation as strongly deformed.



### 5.3. Conclusion

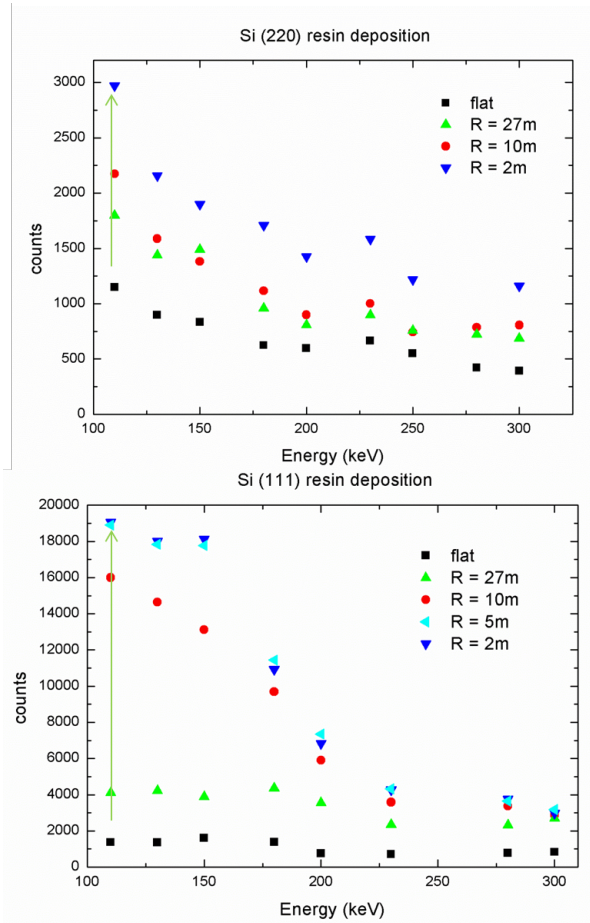


Figure 5.2.3: Trend of the integrated intensity as a function of energy in a flat and two bent ( $R = 54, 29$  m) Si crystals, realized with the resin deposition technique. Up: the symmetrical diffracting geometry 220; Bottom: the asymmetrical diffracting geometry 111.



# Chapter 6

## LAUE Project

A relevant part of the thesis work was dedicated to The LAUE project, supported by the Italian Space Agency (ASI). The project is devoted to create a technology to build a Laue lens with long focal length ( $f = 20$  m) able to focus photons in the  $70 \div 300$  keV energy range. The lens is assumed to be made of petals constituted by a large number of crystals tiles disposed in concentric rings and properly oriented in order to diffract an incident beam parallel to the lens axis in the focal point of the lens. The lens is a spherical cup covered with crystal tiles with diffracting planes perpendicular to the sphere (see Fig. 6.0.1 *Right*). The focal spot is on the symmetry axis at a distance  $f = R/2$  from the cup, with  $R$  the radius of the sphere.

A single petal is developed as a result of the LAUE project, as as Fig. 6.0.1 *Left* reports. The tunnel with the working instruments and motorizations are officially inaugurated in October 2014, demonstrating the possibility to realize the whole Laue lens.

In Table 6.1, the properties of the lens petal prototype are reported. The energy passband ( $70 \div 300$  keV) is defined by the inner and outer radius of the lens (Chap. 1).

|                                   |                                |
|-----------------------------------|--------------------------------|
| Energy passband                   | $80 \div 300$ keV              |
| Focal length                      | 20 m                           |
| Petal inner/outer radius          | 20/80 cm                       |
| Petal dimension (lens diameter)   | $60 \div 150$ cm               |
| No of rings                       | 18                             |
| No of crystals per petal          | 274                            |
| Crystal cross section             | $30 \times 10$ mm <sup>2</sup> |
| Weight of the petal (entire lens) | 27.2 kg                        |

Table 6.1: Main properties of the petal that is being built in the framework of the Laue project.

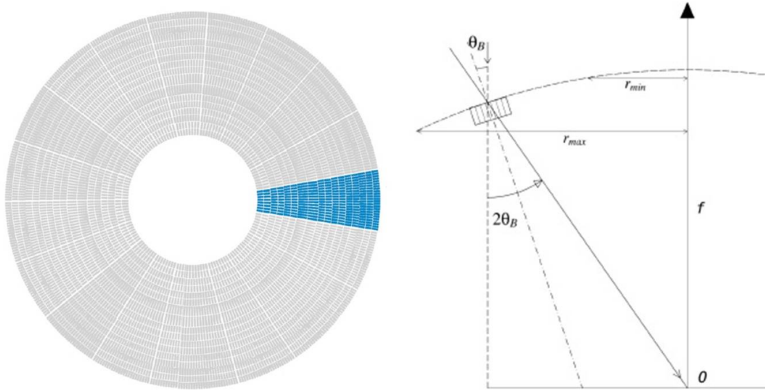


Figure 6.0.1: *Left*: sketch of a Laue lens made of crystals placed in concentric rings. In the LAUE project, a petal as part of a whole lens will be built and test (blue part) [Liccardo et al., 2014]. *Right*: geometry of a Laue lens (Frontera and von Ballmoos, 2010)

The optical focusing elements used to realize the petal prototype are bent crystals. The focusing properties take advantage of the external curvature for geometrical reasons. Bent crystals have important advantages with respect to flat and mosaic ones, as already explained in Chap.2. Moreover due to their focusing effect the angular resolution can be 20 arcsec, significantly increasing the lens sensitivity with respect to that formed by flat crystals (Frontera et al., 2012). Crystals are aligned under control of a  $\gamma$  ray and then glued upon the lens frame, that is fixed during the entire assembling process, while the  $\gamma$  ray source and a mechanical collimator are moved together along the Y and Z axes to simulate a parallel beam. Each diffracting crystal is correctly translated and oriented in order to focus the beam photons on the lens focal plane. This method allows to minimize errors in the orientation of crystals and increases the crystal assembling rate in the lens. I report in this chapter a detailed description of the whole facility in particular the results of the focusing effect from the (220) diffracting planes of GaAs curved crystals with lapping technique. The experimental results are compared with the Monte Carlo simulations, realized by the group of research of LARIX facility. These results are also reported in [Virgili et al., 2015]

## 6.1 Crystal selection

The lens petal will be constituted by bent crystals with a radius of curvature of  $40 \pm 2$  m. In order to efficiently diffract the whole energy range, Germanium (111), and Gallium Arsenide (220) were selected and conveniently disposed on

## 6.1. Crystal selection

the petal as Fig. . 6.1.1 *Left* shows; the main characteristics of tiles are reported in tab. A.2. The GaAs crystals are provided by CNR/IMEM, and Ge by the Sensor and Semiconductor Laboratory of the University of Ferrara, Fug. 6.1.1 *Right*.

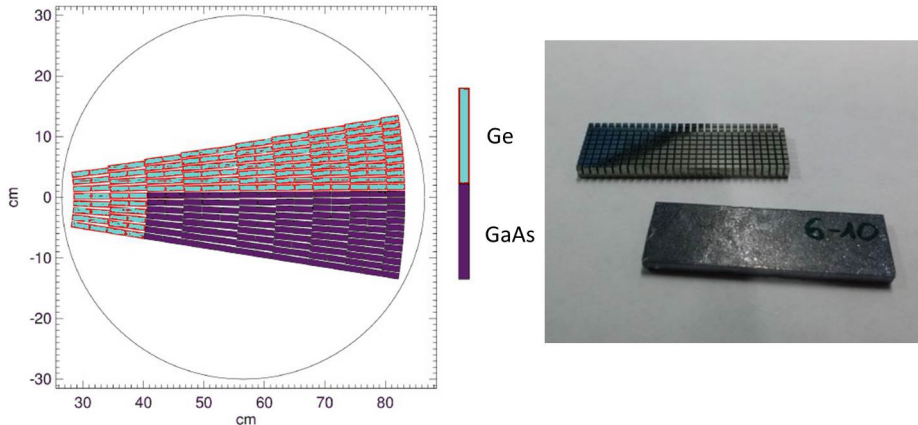


Figure 6.1.1: *Left*: Scheme of the positions of crystals on the lens. The upper part of the petal (blue and red portion) will be filled with Ge (111) while the bottom part will be filled with GaAs (220). *Right*: Two tiles of Ge and GaAs in correspondence of their sector are represented; the two different methods of curvature are evident.

The GaAs (220) crystals are bent by lapping process in which the exact curvature can be obtained selecting the lapping exposure time and the grain of sandpaper as described in Chap. 4. The curvature of the Ge (111) are obtained by grooving the crystal surface (Bellucci et al., 2011; Guidi et al., 2013) in which the curvature is obtained by finely tuning the parameters of the process like the grooves number, width, depth and the speed of the process. Thanks to the focusing capability of each single tile, it was possible to choose the crystal cross section to be  $30 \times 10 \times 2 \text{ mm}^2$ , with the longer size radially placed. The big radial dimension reduces the total number of crystals requested, minimizing the errors due to the misalignment of crystals during the assembling phase. The 2 mm of thickness is chosen because it is a good compromise between high diffraction efficiency and the current limitations in the thickness imposed by the bending technologies. The main characteristics of tiles are reported in tab. 6.2.

The entire set of tiles used for the experiment is provided by two partners of the project: GaAs by our group at CNR/IMEM, and Ge by the Sensor and Semiconductor Laboratory of the University of Ferrara.

|                       | GaAs (220)                 | Ge (111)                   |
|-----------------------|----------------------------|----------------------------|
| Radius of curvature   | 40 m                       | 40 m                       |
| Energy range          | 148 ÷ 304 keV              | 90 ÷ 267 keV               |
| No. of rings          | 14                         | 18                         |
| Radius min ÷ max      | 40.66 ÷ 83.47 cm           | 28.40 ÷ 83.47 cm           |
| No. of crystals tiles | 119                        | 155                        |
| crystals dimension    | 30 × 10 × 2mm <sup>2</sup> | 30 × 10 × 2mm <sup>2</sup> |

Table 6.2: Main characteristic of curved crystals employed in Laue project

## 6.2 The Larix facilities

The entire apparatus for both assembling and testing the lens is installed in the LARIX Italian X ray laboratory (LARIX) located at the Physics and Earth Science Department of the University of Ferrara. The laboratories include an experimental room (LARIX A) with a 12 m long facility and a 100 m long tunnel. The test of crystals for the LAUE project has been performed in LARIX A facility shown in 6.2.1. By means of a motorized crystal holder, it is possible to translate the crystal samples along 2 directions perpendicular to the beam and rotate them around three orthogonal axes. The X ray beam coming from the W-tube crosses two collimators distant each other 580 cm and with adjustable size. The direct and reflected beams are analyzed by means of two detectors, an X ray imager with spatial resolution of 300  $\mu$ m, and a cooled HPGe spectrometer with a 800 eV spectral resolution at 100 keV; both can be moved back and forth along the beam axis.

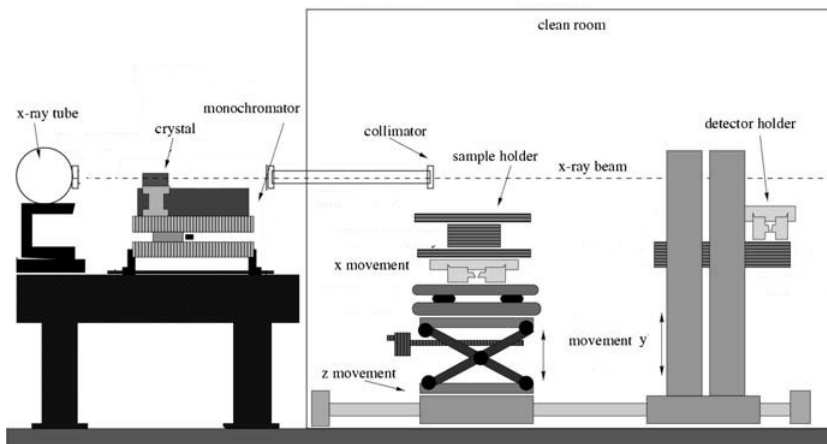


Figure 6.2.1: Sketch (not to scale) of the LARIX A configuration. (Loffredo et al., 2005)

## 6.2. The Larix facilities

The lens assembly apparatus is installed in the 100 m long tunnel. It allows to obtain a small divergence of the beam impinging on each crystal and to build Laue lenses with long focal length. In Figure 6.2.2a sketch of the tunnel and the relative distances between the installed sub-systems is shown.

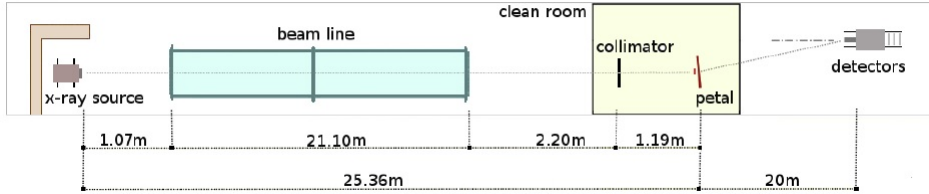


Figure 6.2.2: Scheme of the 100 m tunnel. The relative distances between the elements are reported.

The complete apparatus mounted in the LARIX facility consists of the following elements, that will be described in detail:

- Pipeline with vacuum environment;
- Clean room with thermal and humidity control;
- Adjustable mechanical slit;
- Hexapod positioning device and crystal holder;
- Petal frame;
- Focal plane detectors;
- Translation and rotation systems for the motion of each subsystem (source, collimator slit, crystals);
- Rail for translating the focal plane detectors along the lens axis;
- Hardware and software needed for the remote control (Ground Support Equipment, GSE).

The tunnel of the LARIX facility is equipped with a traditional W tube (provided by Bosello Technology) with a fine focus of  $0.3 \times 0.4 \text{ mm}^2$ , a maximum voltage of 320 kV, and a maximum power of 1800 W (Fig. 6.2.3 *Left*). A 20 mm thick Tungsten shield with a 3 mm diameter hole has been installed in front of the aperture of the X ray tube. To reduce the background at the lens focus, a further collimation is obtained with a drilled (1 mm diameter) 50 mm thick lead collimator. Source and collimators move together on the plane Y-Z (X is the beam axis). After, the collimated beam pass through a 21 m long beam-line under vacuum to avoid absorption and scattering from air of the generated

beam. The beamline is made of 7 modules constituted by a tube of stainless steel 3 m long, Fig. 6.2.3 *Right*. The vacuum environment is guaranteed by three vacuum pumps that keep stable the pressure below 1 mbar. The X ray entrance and exit windows of the beamline are made of carbon fiber 3 mm thick which guarantee a  $\gamma$ /ray transparency  $> 90\%$  at 100 keV.



Figure 6.2.3: *Left*: The X ray source used for assembling and testing the lens petal. *Right*: The 21 m beam line in which is carried out the vacuum for avoiding absorption and scattering.

After the beam-line the beam impinges on a slit with variable aperture. It moves together with the X ray generator along the Y-Z axes to artificially reproduce a source coming from the infinity. The collimator is equipped with motors that can translate it in the X-Y plane and it is provided with three motors to rotate the slit around the X, Y and Z axes. It is constituted by a lead panel with  $200 \times 200\text{mm}^2$  cross section and 50 mm thick. In the center of the panel there is a  $30 \times 30\text{mm}^2$  motorized slit with variable aperture obtained by means of four 20 mm thick blades made of Tungsten Carbide, Fig. 6.2.4 *Left*. The orientation and the positioning of each crystal on the carbon fiber petal frame is performed with a mechanical micro adjusters 6-axis hexapod system controlled by software. The rotation around X, Y and Z axes are possible with an error of 1 arcsecond. The crystal tile holder has been developed in order to strongly hold the tile without introduce deformations on crystals and to leave free the surfaces of the crystal, where the incident beam arrives and the diffracted beam is produced (Fig.6.2.5 *Right*).

The lens petal frame is realized with a superposition of 10 layers of carbon fiber, for a total thickness of 2.3 mm, in order to reduce the absorption of X





Figure 6.2.4: *Left*: Collimator and carriage. *Right*: the hexapod system that is used to tilt and place each crystal in the proper position.

rays. It has little holes in correspondence of the positions of the crystals where the resin is injected for fixing the crystals to the frame (Fig. 6.2.5).

The glue used for fixing the tiles must have a fast curing time and a shrinkage as low as possible, to minimize the building time and maximize the gluing accuracy, which is the most critical part. The elements that influence the gluing process are various. The temperature and the humidity of the building environment play a crucial role in the stability of the crystal/adhesive/support system. For this reason the petal frame is positioned inside a clean room with humidity and temperature stability control was set up ( $20 \pm 1^\circ$ , relative humidity  $\varphi = 50 \pm 5\%$ ). The diffracted beam coming from each crystal is measured by means of two focal plane detectors: an imager flat panel and a cooled HPGc spectrometer (see Fig. 6.2.6). They are placed on a carriage at the focal distance of 20 m from the petal frame and they can move along the lens axis by means of a 15 m long rail.

The imager allows to detect the space distribution of the photons diffracted by each crystal which is irradiated by the incident beam. It is based on a CsI scintillator (0.8 mm thick) that converts the X and  $\gamma$  rays into optical light that is afterwards converted into an electric signal from an array of photodiodes. It has a spatial resolution of 200  $\mu\text{m}$  with an active area of  $28.48 \times 28.48\text{cm}^2$ . By means of an IDL code the Y and Z coordinates of the diffracted beam are converted into two rotation angles in order to properly shift the diffracted image over the reference pixel in the center of the detector. The cooled HPGc

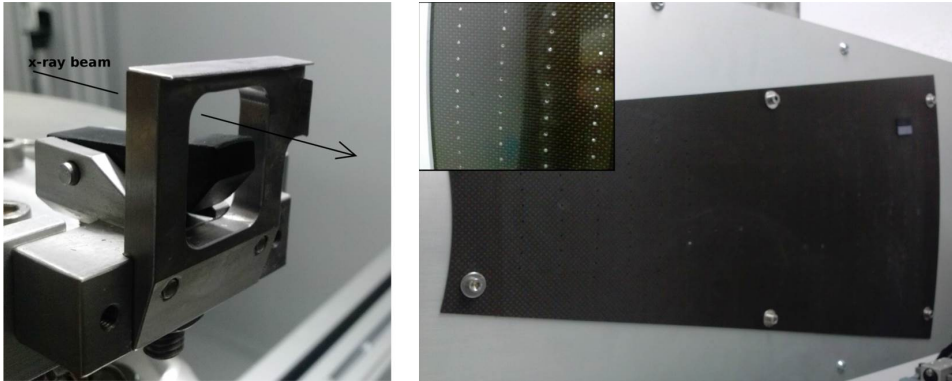


Figure 6.2.5: *Left*: The holder system. *Right*: The petal frame used as a support for the Laue lens. In the small box is visible a small portion of the petal with the holes used to inject the glue from the back side.

spectrometer provides the spectrum of the diffracted photons. The spectrometer allows to establish the well-defined diffracted energy by each crystal, and so to determine the correct positioning of them on the lens.

The entire subset of carriages can be remotely controlled from the control room. For the control of each sub-system a proper LabVIEW code has been developed (Virgilli et al., 2013). The front-end of the remote management suite is shown in Fig. 6.2.7 *Left*. During the assembling procedure as well as in the testing phase a selection of the generic light indicators (indicating the crystal to be placed at the corresponding lens position) make the X ray beam (source and collimator slit) and hexapod/crystal holder automatically moving to the desired position. The control of the hexapod is instead not implemented in the LabVIEW code but is obtained exploiting a dedicated software (Fig. 6.2.7 *Right*).

### 6.2.1 Alignment of the facility

Much time was spent to correctly align all the components of LAUE apparatus in the tunnel. The petal frame has been placed perpendicularly to the direct beam (X-axis direction) and within the beamline cross section (in the Y-Z plane). The detectors were placed along the X-axis at 20 m from the petal frame. The structure holding the detectors was designed in order to get both direct and diffracted beams by a translation along Y axis. The alignment was done by means of a laser that emits a horizontal light beam and it is set between the pipeline and the motorized collimator slit. The beam is reflected by a mirror placed at  $45^\circ$  and sent to a beam-splitter which splits it along opposite directions: one towards the hexapod crystal holder, positioned in a reference position, through the collimator slit and the other toward the  $\gamma$  ray source through



Figure 6.2.6: The two detectors used in the LAUE project: the flat panel detector is positioned below the HPGe detector.

the pipeline (see Fig. 6.2.8 *Left*). Mirrors placed over the source and the crystal holder reflect back the two beams. Their superposition in the laser output ensures the correct zero-position for source, collimator, hexapod holding aperture, and the petal reference position. The optical alignment guarantees an excellent precision in positioning the center of the  $\gamma$  ray imager in correspondence of the lens focus.

The  $\gamma$  ray alignment performs a fine tuning of the previous alignment process. It has been performed using two Tungsten crosses (wire diameter of 200  $\mu$ m) that are placed respectively on the center of the crystal holder, and on the center of the slit. The crystal holder with the tungsten cross was placed in correspondence of the frame hole from which the resin is injected to fix the crystal to the frame.

The right orientation of each crystal on the frame is achieved when the beam diffracted by the crystal has a peak energy corresponding to the energy expected for the selected hole. A Ge (111) tile was first tested. Its orientation was that expected for the hole #24 with nominal centroid energy of 96.14 keV. Fig. 6.2.9 *Left* shows the spectrum of the incident beam. When the spectrometer is translated to the lens focus, the diffracted spectrum occurs, Fig. 6.2.9 *Right*. Similarly, for the GaAs (220) tile placed in the contiguous hole, the spectrum of the diffracted beam is shown in Fig. 6.2.10 *Left*. A systematic monitoring of the diffracted beam was performed during the gluing procedure. The spectrum was acquired every 15 minutes after the adhesive injection. Figure 6.2.10 *Right* shows that the effect of the glue polymerization does not produce any significant deviation of the centroid energy with respect to the nominal energy expected for the GaAs (220) placed in the hole#25.

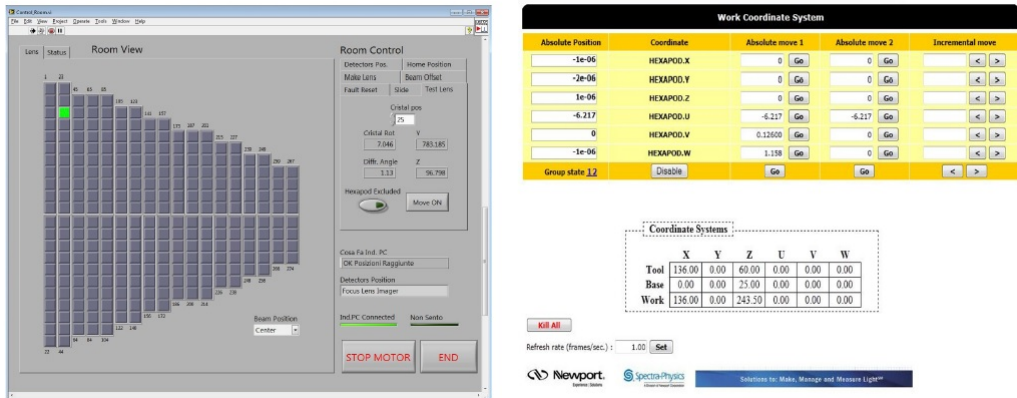


Figure 6.2.7: *Left*: Front-end of the LabVIEW management software for the remote control of each carriage. *Right*: the dedicated software for the hexapod control.

After the glue polymerization, the holder removal is the most critical phase. With the GaAs (220) the centroid energy changed by less than 1 keV, corresponding to less than 20 arcsec. Figure 6.2.11 shows the measured spectra before and after the holding removal. The effect is mainly related to the angular tilt between the petal frame and the glued crystal plane. The tilt produces an asymmetric glue distribution over the crystal, giving origin to the observed energy change. The same effect was also observed during the preliminary resin tests in which the orientation of 20 tiles of  $30 \times 10 \text{ mm}^2$  cross section was monitored during their polymerization phase. A systematic deviation of 20-30 arcseconds was found; this systematic error is taken into account during the assembling phase.

### 6.3 Focusing effect

When X rays from an infinitely far source impinge over a perfect crystal, the diffracted image has the same size of the crystal cross section. In the case of a mosaic crystals, the mosaic spread results in a defocusing effect, so the size of the diffracted image is the convolution between the crystal size itself and the mosaicity. On the other hand the spot dimension of the diffracted beam is strongly reduced by a proper curvature of the crystal in the x direction causing a focusing effect, even if the mosaic defocusing is still present, Fig. 6.3.1. For a bent crystal the spatial distribution of the photons on the focal plane along the x direction is smaller than the crystal length. No focusing effect is expected in the other direction.

The GaAs (220) bent crystals realized with lapping process have been characterized in terms of focusing effect. The curvature radius of  $R = 40 \pm 1.5$

### 6.3. Focusing effect

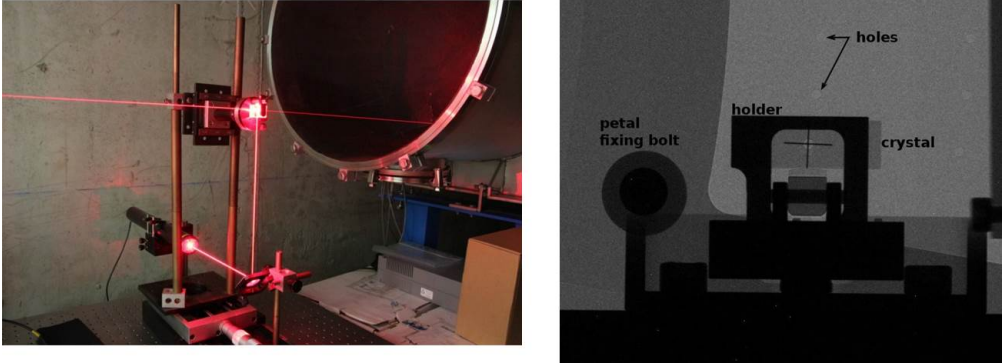


Figure 6.2.8: *Left*: The laser adopted to ensure the optical alignment. *Right*: The radiography of the entire apparatus once the collimator has been shifted out of the X ray beam. Part of the petal, the holder and a dummy crystal with the tungsten cross are visible.

m was estimated with the method already described in sec. (4.1). To test the focusing effect, the beam size on the crystals was set to  $20 \times 10\text{mm}^2$ , the longer size in the x coordinate, in order to better demonstrate the focusing effect along that direction. The image of the diffracted signal was studied with a total exposure time of 510 seconds. The detector was progressively set at the distance of 8.5, 9.5, 10.5, 11.5, 12.5, 13.5 m from the petal frame. The results are shown in Fig. 6.3.2, where it is evident that the different distance between crystal and detector results in a changing of both image shape and dimensions. The analysis of the x profile for each image of the diffracted beam acquired at different distances are also shown. The GaAs crystal mosaicity can be satisfactorily described with a Gaussian function, plus a constant that represents the background counts which have not been subtracted. The function adequately fits the data, mainly at distances close to the distance 11.40 m, while the fit becomes poor far from the nominal position (e.g. at 8.5 m or 13.5 m). This discordance between fit and data is caused by a not uniform curvature of the specific sample along its x axis, which is emphasized particularly out of focus. The FWHM as a function of the distance between the crystal and the detector is shown in Fig. 6.3.3

It is important to note that the focusing effect occurs at 11.40 m instead of 20 m. Indeed a parallel beam coming from a source placed to infinite is focalized at a distance  $f=R/2$  from the lens. In the case of a source positioned at a finite distance, as in the case of laboratory, the focal point position changes.

Let's consider a diffracting plane, reported in green in Fig. 6.3.4, placed at distance x from the axis of the lens and perpendicular to the curved plane of

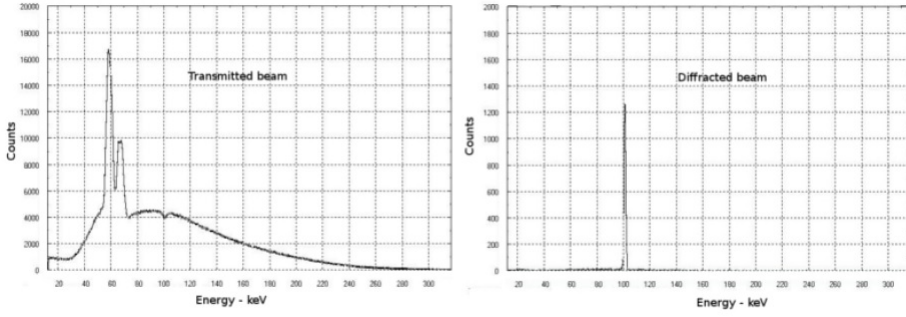


Figure 6.2.9: Spectrum of the beam through a Ge (111) tile, when it is oriented for diffraction. *Left*: transmitted spectrum. *Right*: diffracted spectrum. Exposure time = 300 sec.

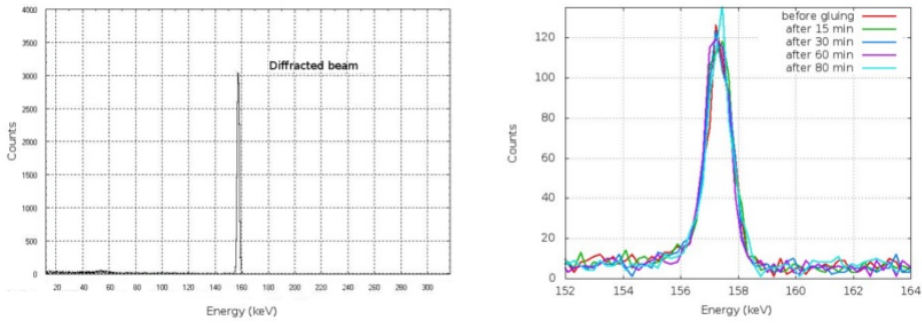


Figure 6.2.10: *Left*: Spectrum of the diffracted photons from the GaAs (220) tile placed in the cell #25. The nominal energy for its position is 157.10 keV. Exposure time = 300 sec. *Right*: After the injection of the adhesive, the GaAs (220) has been systematically monitored during the 80 minutes of the polymerization phase. No significant deviation with respect to the nominal energy was observed.

the lens.

The angle diffracting  $\beta$  with respect to the parallel beam is  $\beta = \frac{x}{2F} = \frac{x}{R}$ . If the source S is placed at a distance s from the lens, the angle that the beam coming from S and incident on the diffracting plane considered creates with the direction parallel to the axis lens is  $x/s$ . The diffracting angle  $\gamma$  will be

$$\gamma = \frac{x}{S} + \beta = \frac{x}{S} + \frac{x}{R} \quad (6.3.1)$$

The angle  $\alpha$  between the diffracted beam and the lens axis is  $\alpha = \frac{x}{S'}$ , so

$$\alpha = \beta + \gamma = \frac{x}{S} + 2\beta = \frac{x}{S} + \frac{x}{F}. \quad (6.3.2)$$

It is possible to obtain the following equation:

$$\frac{1}{S'} = \frac{1}{S} + \frac{1}{F} \quad (6.3.3)$$

That is in agreement with that obtained in (Halloin and Bastie, 2005) In particular in the Larix facility  $F = 20$  m and  $s \sim 26$  m, so the new focal point is at  $F' \sim 11.3$  m. To validate the results obtained, Monte Carlo simulations are realized by the Larix team. All the simulations are made with the LLL (Laue Lens Library) software developed by the Laue project team. The code is developed for a complete description of Laue lenses made of mosaic or perfect crystals, with flat or bent structure, for a source of radiation placed at either a finite distance or infinitely far from the target. The software is based on a ray tracer that takes into account the diffraction law, the absorption caused by crystals of different materials and by the lens frame and allows the spatial distribution of the photons at a given distance from the crystal after the X ray diffraction to be determined. Different geometries of the lens have been implemented depending on the particular case of interest. Single crystals, rings of crystals, sectors (petals) or entire lenses made of tiles set in concentric rings or in spiral configuration can be simulated. A dedicated library also assumes an ideal focal plane X ray imager detector (whose size can be adapted to the particular application) with spectral capability. The detector can be set at an arbitrary distance from the Laue lens. The libraries files are invoked by a main python application that requires a number of input parameters (crystal tiles properties and dimensions, lens focal length, the crystal packaging factor, the lens energy passband) providing the physical configuration of the simulated lens (total weight of the lens, spatial dimensions, total geometric area) and its scientific features (output energy pass-band, photon distribution on the focal plane, effective area, sensitivity). I report here the simulation performed and reported in (Virgilli et al., 2015) in order to study the focusing effect in a curved GaAs (220) crystals, for a source placed at a finite distance 26.4 m. Fig. 6.3.5 reports the simulated diffracting images calculated with a beam size of  $20 \times 10 \text{ mm}^2$  for the detector place at different distance 8.5, 9.5, 10.5, 11.5, 12.5, 13.5 m from the petal (Virgilli et al., 2015). In Fig. 6.3.6 the x profiles of the images acquired at different distances with the red line representing is the best fit function are also shown . A satisfactory function is represented by a convolution between a Gaussian profile with a fixed value of FWHM and a rectangular function with variable width. Within this explanation, the width of the Gaussian function represents the angular spread which is constant along the entire crystal length. In the experimental case the mosaicity of the sample was of  $\sim 15$  arc seconds.

In Tab. 1 the best fit values of the measured FWHM are reported and compared with those obtained from the Monte Carlo calculations.

Along the x direction, where the focusing effect is expected, we found a

| Crystal-detector distance<br>(m) | Experimental data<br>FWHM<br>(x dimension mm) | Monte Carlo<br>FWHM<br>(x dimension mm) |
|----------------------------------|---|---|
| 8.5                              | $4.95 \pm 0.21$                               | $4.45 \pm 0.07$                         |
| 9.5                              | $3.11 \pm 0.25$                               | $3.30 \pm 0.07$                         |
| 10.5                             | $1.85 \pm 0.23$                               | $2.25 \pm 0.07$                         |
| 11.5                             | $1.37 \pm 0.29$                               | $1.35 \pm 0.07$                         |
| 12.5                             | $2.29 \pm 0.24$                               | $2.11 \pm 0.08$                         |
| 13.5                             | $3.12 \pm 0.24$                               | $3.26 \pm 0.07$                         |
| 14.5                             | $4.63 \pm 0.21$                               | $4.75 \pm 0.07$                         |

Table 6.3: Table 1: Comparison between the fwhm of the x and the y profiles for the acquired diffracted images, with the Monte Carlo simulations, at different distances between crystal and detector ( $R_c = 40$  m curvature radius). The FWHM of the rectangular function is taken at half of the peak value of the curve.

good agreement between experimental and Monte Carlo results. Along the y coordinate, no focusing effect is expected and the diffracted beam suffers a lengthening which is mainly due to the divergence of the beam.

## 6.4 Conclusion

In this chapter, a real focusing effect from a bent crystal of GaAs (220) realized with damaging technique has been shown and discussed. For the Laue project a big number of tiles made of GaAs (220) and Ge (111) are being mounted on a lens petal frame, in order to build for the first time a Laue lens petal capable of operating over a broad energy band ( $90 \div 300$  keV). A systematic analysis of the diffracted profiles has been presented, using a Monte Carlo ray tracer with a set of tools capable of describing the focusing effect for both a parallel beam and a diverging beam. A detailed study of the behavior in the case of a finite distance between the radiation source and the crystals is done. The good agreement found between experimental tests and Monte Carlo results give us the confidence needed about the correctness of the Monte Carlo calculations also for the case of a parallel beam from an astrophysical source, that is the final goal of the Laue project.



## 6.4. Conclusion

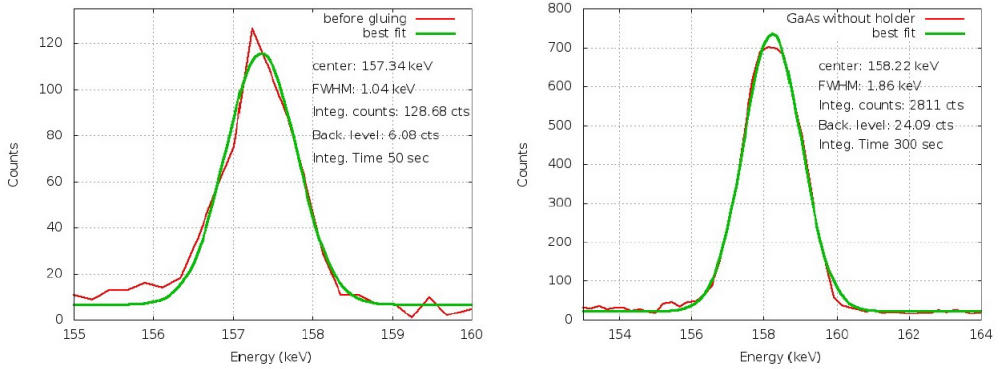


Figure 6.2.11: Diffracted spectra of the GaAs (220) before and after the mechanical release of the holder. The difference is visible in terms of energy deviation from the nominal position. After the holding removal the energy deviation was within 1 keV, corresponding to 20 arcseconds. The effect is known and mainly due to a not uniform glue distribution between the crystal and the carbon fiber support, given the angular tilt applied to the crystal. This effect can be taken into account during the assembling phase.

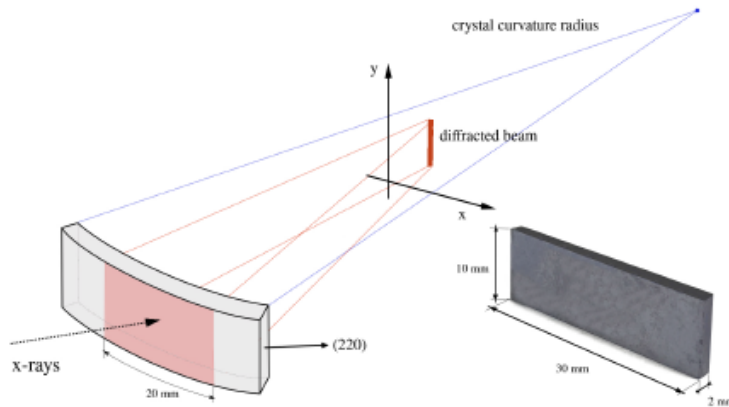


Figure 6.3.1: sketch of a bent GaAs crystal and the principles of the diffraction from the (220) planes. The crystal dimensions and the diffraction planes are also indicated. The curvature radius of 40 meters is also indicated and overstated for sake of clarity. The dimensions of the X ray beam are also drawn over the crystal cross section. *Right:* picture of a bent GaAs mosaic crystal tile used for the experimental run.

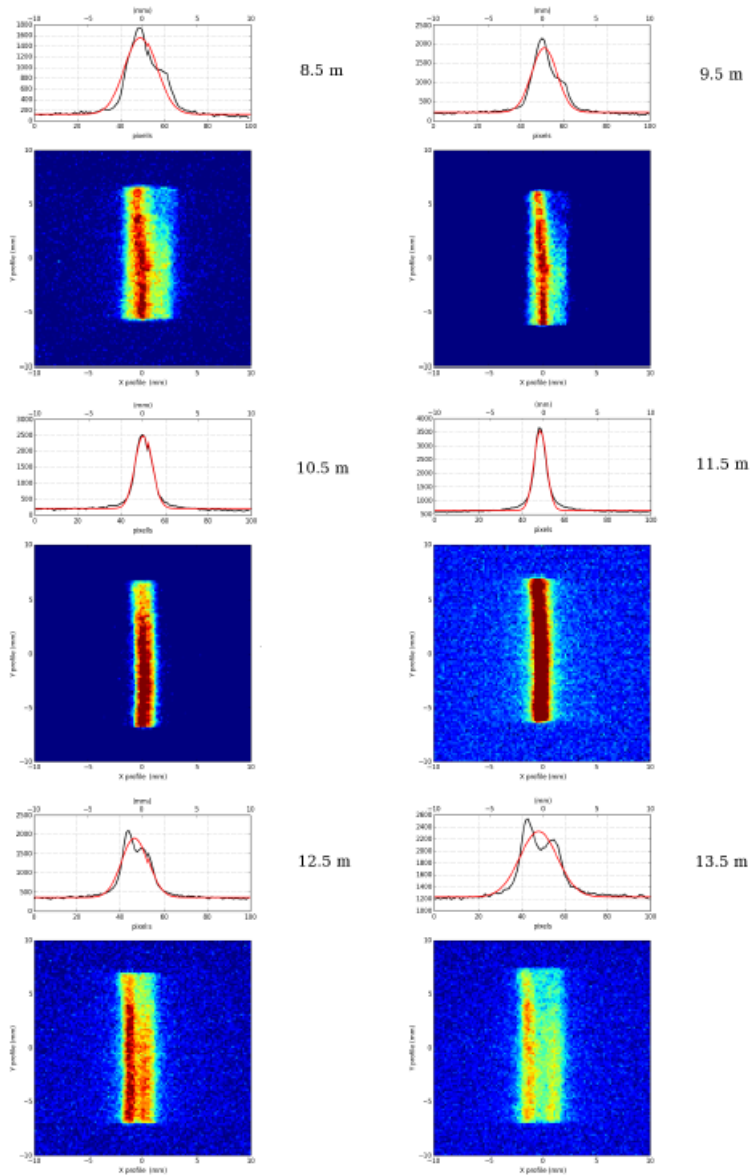


Figure 6.3:2: Diffracted beams measured at different distances crystal/detector, from the top. To the bottom right 8.5, 9.5, 10.5, 11.5, 12.5, 13.5 m, respectively.

## 6.4. Conclusion

---

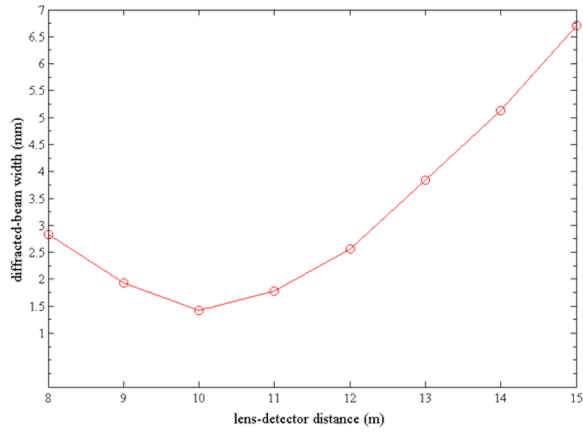


Figure 6.3.3: Fig. Plot of the FWHM of the x profile of the diffracted image as function of the distance between crystal and detector, for a GaAs (220) crystal with  $39.9 \pm 1.5$  m curvature radius and fixed distance source-target of 26.40 m.

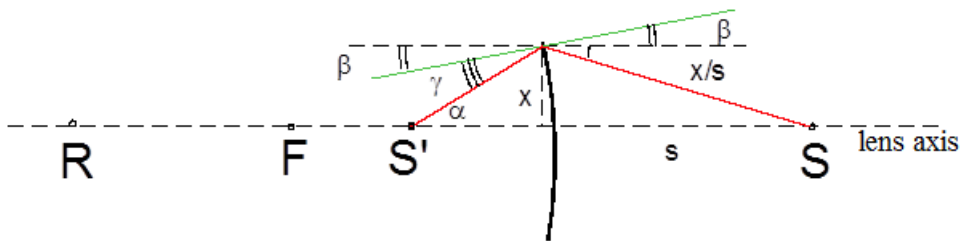


Figure 6.3.4: Sketch of a source S placed at a finite distance s from the lens.

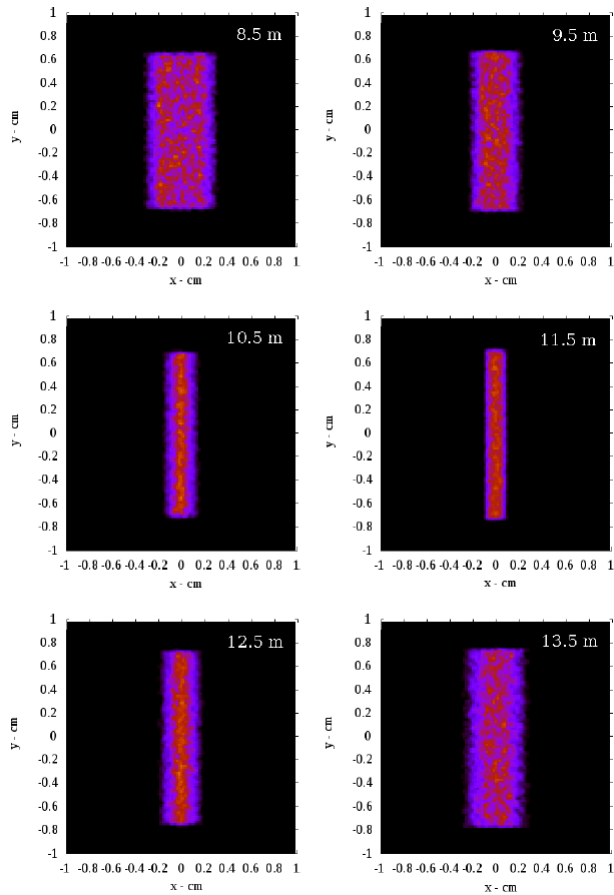


Figure 6.3.5: Simulation of the diffracted image generated by a GaAs bent crystal with a beam size of  $20 \times 10 \text{ mm}^2$ , observed at 8.5, 9.5, 10.5, 11.5, 12.5, 13.5 m from the crystal (respectively from the left top to the right bottom).

## 6.4. Conclusion

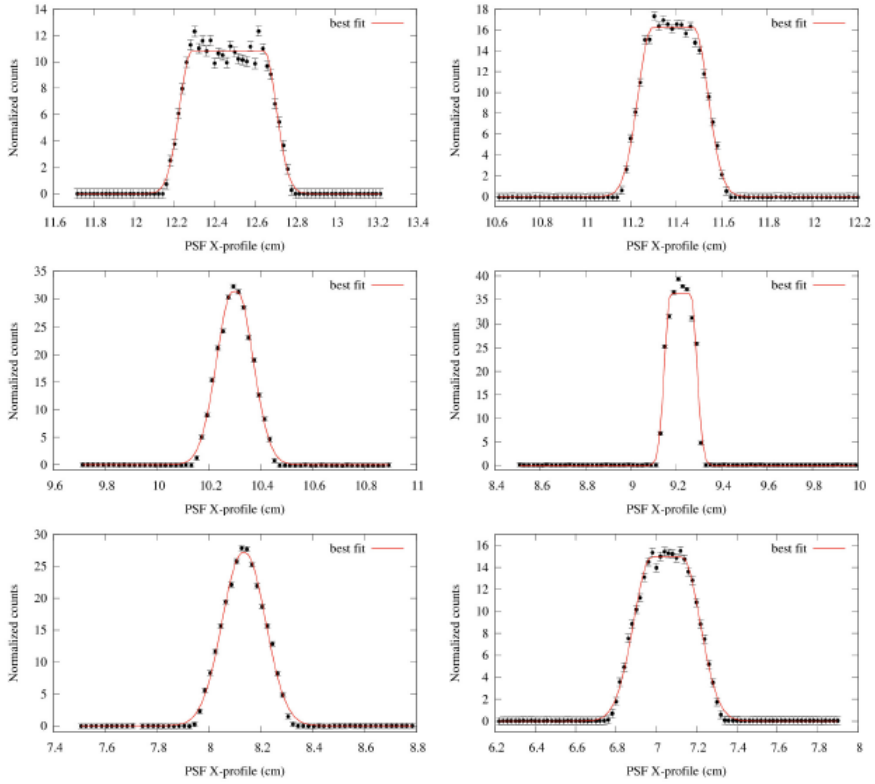


Figure 6.3.6: X-profile of the diffracted image generated by a GaAs bent crystal with a beam size of  $20 \times 10 \text{ mm}^2$  cross section observed at 8.5, 9.5, 10.5, 11.5, 12.5, 13.5 m from the crystal (respectively from the left top to the right bottom).



# Conclusions

The focusing of X and  $\gamma$  rays can be obtained by a Laue lens made of properly oriented crystals. The efficiency in focusing of the lens is closely related to the diffraction efficiency of the single crystals composing the lens. In this thesis crystals to be used for focusing X and  $\gamma$  ray in the energy range  $60 \div 600$  keV have been studied.

An efficient focusing system is crucial for applications like medical imaging and X ray astronomy where wide beams must be focused.

In previous studies mosaic crystals with a high electronic density, such as Cu or Au, were considered for the realization of the lens, owing to their high diffraction efficiency. In this work I studied the diffraction efficiency of Si, Ge and GaAs curved crystals on the basis of the theory of X ray diffraction.

It is found that in crystals with curved diffracting planes (CDP) having radii of curvature of several tens of meters for X ray energies between 60 and 600 keV a simplified approach can be applied for calculating the integrated X ray reflectivity of the crystals, considered as a measure of the diffraction efficiency. Under this approximation, the maximum value of the integrated reflectivity is given by a crystal thickness  $t_{max} = 1/\mu$ , as in the case of ideal mosaic crystals. Then it is found that Si, Ge and GaAs crystals with optimized thicknesses show a comparable or superior diffraction efficiency with respect to the heavier materials previously proposed.

The bending technique mainly used during this work consists in a surface treatment with sandpapers of different grain sizes. This process introduces defects in a superficial layer that induces the convex bending of the whole crystals. The strain introduced by the surface treatment are reproducible, uniform and depend mainly on the type of used paper, i.e. larger grains introduce a larger stress and a lower curvature radius.

Another new bending technique is developed and the main results are shown. The process consists on a film deposition of a selected bi-component epoxy resin on one side of crystal, made uniform in thickness by mean of a spin-coater. During the polymerization, the resin induces a tensile strain that causes the bending of the substrate, with concave curvature on the side of the resin deposition. Choosing the speed of spin-coating, so changing the thickness of the

film, a control of radius of curvature can be obtained. Moreover the possibility to combine the two bending techniques to obtain CDP crystals with a stronger curvature in rather thick crystals was demonstrated.

In order to verify the results of the theory on the crystal diffraction efficiency, detailed characterizations at low and high X ray energies were performed on flat and bent crystals obtained with the damaging and the resin deposition technique. GaAs and Si flat and curved crystals realized with damaging technique were measured in Laue geometry in several geometries at X ray energies of 17, 19, 22.5 and 59 keV. As expected an increase of diffraction efficiency in asymmetrical diffraction geometry in CDP crystals with respect to the flat ones is observed. On the other hand, an unexpected increase of the integrated intensity in symmetrical geometry, not predicted by the theory, is observed in all the measurements performed with different set up. The experimental trend of the integrated reflectivity as a function of the radius of curvature is in good agreement with the prediction of the theory for bent perfect crystals, so it is possible to conclude that the surface damage has a limited effect on the crystal reflectivity.

A study of the integrated reflectivity in the energy range of interest ( $100 \div 350$  keV) was performed at the Institute Laue Langevin in CDP crystals realized with damaging and resin deposition techniques, both at symmetrical and asymmetrical geometries. Also at these energies the diffraction efficiency of bent crystals was much larger (a 12 time increase is observed for bent crystals in asymmetrical 111 geometry) than that measured in flat crystals. The diffraction efficiency of CDP crystals realized with both techniques tends to coincide with that of flat crystals at very high energies ( $> 200$  keV). This suggests that also real flat perfect crystals can be considered as strongly bent or mosaic crystals at very high X ray energies.

In conclusion we found that crystals of relatively light elements, such as Silicon, Germanium and Gallium Arsenide, properly bent by using one of the two methods proposed in this thesis, are completely suitable to realize a lens for focusing wide X and  $\gamma$  rays beams, with applications in the field of X ray astronomy and nuclear medicine.



# Appendix A

## Calculation of the inner lattice plane bending in bent crystals

We assume that the crystals has a thickness  $t$  and a spherical curvature of radius  $R$  given by an applied external stress, such as in the case of surface treated crystals. We want to calculate the variation of the Bragg angle condition of a X ray beam crossing the crystal in the condition of Laue diffraction for a lattice plane with inclination  $\phi$  with respect to the normal to the surface (see Fig. A.0.1). The angle  $\phi$  is positive when is clockwise positioned with respect to the normal to the surface; the angle  $\theta_B$  is positive when the incident beam is clockwise rotated with respect to the lattice plane.

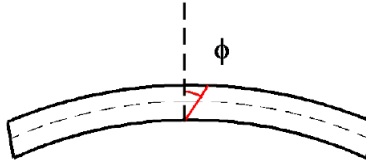


Figure A.0.1: Bent crystal with trace of the lattice plane;  $\phi$  is positive with respect to the surface normal.

Due to the effect of tensile strain introduced by the damaged layer every part of the lamella undergoes a biaxial tensile strain along the crystal surface, varying with crystal depth: in the case of Fig. A.0.1 the strain will be tensile at the upper crystal surface and compressive at the lower crystal surface. The line in the middle of the lamella is at zero strain.

In the case of cubic lattices the relationship between stress  $\sigma$  and strain  $\epsilon$  is given by (Ferrari et al., 2013):

$$\begin{cases} \sigma_{xx} = c_{11}\epsilon_{xx} + c_{12}\epsilon_{yy} + c_{12}\epsilon_{zz} \\ \sigma_{yy} = c_{12}\epsilon_{xx} + c_{11}\epsilon_{yy} + c_{12}\epsilon_{zz} \\ \sigma_{zz} = c_{12}\epsilon_{xx} + c_{12}\epsilon_{yy} + c_{11}\epsilon_{zz} \\ \sigma_{ij} = c_{44}\epsilon_{ij} \quad i \neq j \end{cases} \quad (\text{A.0.1})$$

For the sake of simplicity we now consider the case of cubic crystals having a (001) orientation of the surface, coincident with our z direction. For such biaxial strain  $\sigma_{xx} = 0$ ,  $\sigma_{xx} = \sigma_{yy}$ ,  $\sigma_{ij} \neq 0$  for  $i \neq j$ , so the strain components can be written as:

$$\epsilon_{zz} = -2 \frac{c_{12}}{c_{11}} \epsilon_{yy} \quad (\text{A.0.2})$$

that can be written also as:

$$\epsilon_{\perp} = -2 \frac{c_{12}}{c_{11}} \epsilon_{\parallel} \quad (\text{A.0.3})$$

Assuming  $a$  as the lattice parameter of the crystal considered, due to the strain the local values of the lattice parameters  $a_{\perp}$  and  $a_{\parallel}$ , will differ from the value  $a$  of the unstrained material. Locally there will be a perpendicular  $\epsilon_{\perp}$  and a parallel  $\epsilon_{\parallel}$  strain of opposite sign, related to the local lattice parameters  $a_{\perp}$  and  $a_{\parallel}$  by (Fig. A.0.2):

$$\begin{aligned} \epsilon_{\perp} &= \frac{a_{\perp} - a}{a} = \frac{\Delta a_{\perp}}{a} \\ \epsilon_{\parallel} &= \frac{a_{\parallel} - a}{a} = \frac{\Delta a_{\parallel}}{a} \end{aligned} \quad (\text{A.0.4})$$

Due to the deformation generated by the biaxial strain there are two effects that cause the shift of the Bragg condition:

1. the effect associated to the change in the lattice parameter;
2. the effect associated to the change in the tilt of the reflecting plane.

The first effect can be calculated from the formula (Ferrari et al., 2013 modified modifying  $\phi$  in  $90^\circ - \phi$ ):

$$\Delta\theta_B = -\tan\theta_B \cdot \left( \frac{\Delta a_{\perp}}{a} \sin^2\phi + \frac{\Delta a_{\parallel}}{a} \cos^2\phi \right) = -\tan\theta_B \cdot (\epsilon_{\perp} \sin^2\phi + \epsilon_{\parallel} \cos^2\phi) \quad (\text{A.0.5})$$

so the first contribution becomes:

$$\Delta\theta_B = -\tan\theta_B \cdot \epsilon_{\parallel} \left( \cos^2\phi - 2 \frac{c_{12}}{c_{11}} \sin^2\phi \right) \quad (\text{A.0.6})$$

The lattice rotation is expressed by the formula :

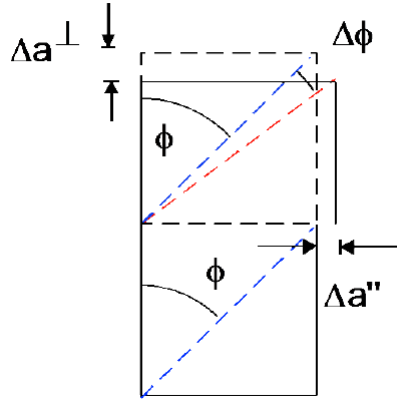


Figure A.0.2: effect of the lattice deformation on the rotation  $\Delta\phi$  of the lattice planes.

$$\Delta\phi = -\frac{\sin 2\phi}{2} \left( \frac{\Delta a_{\perp}}{a} - \frac{\Delta a_{\parallel}}{a} \right) = \frac{\sin 2\phi}{2} \cdot \epsilon_{\parallel} \left( 1 + 2\frac{c_{12}}{c_{11}} \right) \quad (\text{A.0.7})$$

Another contribution comes from the crystal deformation itself. When the incident beam crosses the crystal, the angle of incidence at an inclination  $\phi + \theta_B$  with respect to the surface normal, the angle of incidence on the diffracting plane at a depth  $x$  with respect to the crystal surface is rotated by an amount given by (Fig. A.0.3) :

$$\Delta\alpha = -\frac{x}{R} \cdot \tan(\phi + \theta_B) \quad (\text{A.0.8})$$

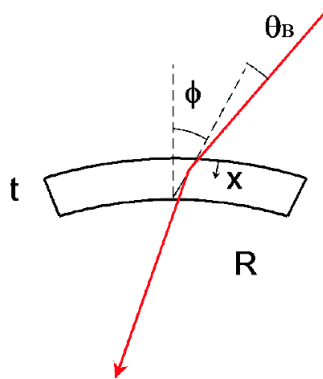


Figure A.0.3: Bragg diffraction with positive  $\phi$  and  $\theta_B$ .

Finally we observe that due to the lattice deformation associated to the spherical curvature (Fig. A.0.1) with biaxial strain we have  $\epsilon_{//} = -\frac{x}{R}$ .

Now, adding all the three contributions  $\Delta\theta_B$ ,  $\Delta\phi$  and  $\Delta\alpha$ , the variation of the bragg condition along lattice plane  $\Delta\theta(x)$  is (Ferrari et al., 2013):

$$\Delta\theta(x) = \frac{x}{R} \left[ -\tan(\phi + \theta_B) - \frac{\sin 2\phi}{2} \cdot \frac{c_{11} + 2c_{12}}{c_{11}} + \tan \theta_B \left( \cos^2 \phi - \frac{2c_{12}}{c_{11}} \sin^2 \phi \right) \right] \quad (\text{A.0.9})$$

We observe that according to the previous formula for symmetric Laue diffraction  $\phi = 0$  and  $\Delta\theta(x) = 0$ , that is no broadening of Laue diffraction peak or increase of the peak integrated intensity should be observed for bent crystals. This is confirmed in elastically bent silicon crystals.

# Appendix B

## Origin of strain in surface damaged bent crystals

### B.1 Line tension characterization

In Chap. 4 a method to produce curved crystals based on a controlled damage of the crystal surface [5,6] is described. Curvatures of several metres, determined by means of high resolution X ray diffraction, were obtained in Si and GaAs crystals up to 2 mm in thickness. The crystal bending is induced by a compressive strained layer of few micrometers in thickness due to the surface damage, but the physical mechanism at the origin of this compressive strain is still unclear. Scratches, inclusions, and dislocations due to the sandpaper treatment introduce defects in a superficial layer of the sample causing an expansion of the crystal lattice. This results in a wafer bending with convex curvature on the side of the damaged surface. We can consider the damaged superficial layer at the same way as a thin film deposited on a substrate: the stress in the film induces a curvature of the substrate that can be described by means of the Stoney formula (Stoney, 1909). This equation can be applied when the film is thin compared to the substrate and the stress is in-plane. For an elastic isotropic substrate the Stoney formula is:

$$\sigma_f t_f = \frac{E_s t_s^2}{6(1 - \nu_s) R} \quad (\text{B.1.1})$$

where  $\sigma_f$  is the in-plane stress component in the film,  $t_f$  is the film thickness,  $E_s$  and  $\nu_s$  are the Young's modulus and the Poisson's ratio for the substrate, respectively,  $t_s$  is the substrate thickness, and  $R$  is the curvature radius. In the case of an elastically anisotropic substrate, as GaAs, the formula in B.1.1 cannot be used. For a (001) substrate the correct formula is:

$$\sigma_f t_f = \frac{t_s^2}{6(s_{11} - s_{12})R} \quad (\text{B.1.2})$$

where  $s_{11}$  and  $s_{12}$  are elements of the compliance tensor of the substrate ([Janssen et al., 2009]). The factor  $1/(s_{11}-s_{12})$  is called the biaxial modulus  $M_{001}$  of the material. In both cases, depending on several features (as substrate shape and intensity of the force per unit width) the predicted deformation of the wafer can be axially symmetric, ellipsoidal, or cylindrical (Janssen et al., 2009; Finot et al., 1997; Fahline et al., 1991).

In the present case our system made of a thin film and a substrate is made of the same material and equation B.1.2 can be simplified and made independent of the elastic constants of the particular material; it becomes:

$$f \cdot t = \frac{T^3}{6R(T-t)} \approx \frac{T^2}{6R} \quad (\text{B.1.3})$$

In which  $f$  is the layer strain,  $t$  is the layer thickness,  $T$  is the substrate thickness and  $R$  is the curvature radius. To study the effect of superficial damaging a GaAs crystal was divided in five pieces, each one underwent a superficial treatment with the same sandpaper P1200 but different time long. Figure B.1.1, panel A shows the x curvature radius  $R_x$  dependence on the squared residual thickness. Since grain dimension of the P1200 sandpaper is only 14  $\mu\text{m}$ , we can approximate the sample residual thickness as the substrate thickness  $T$  of the Stoney formula B.1.3. Since we observe a linear dependence with the squared thickness we conclude that the line tension of the superficial layer is almost constant in the different samples and does not depend on the treatment time. Figure B.1.1, panel B displays the resulting  $\sigma_f t_f$  as a function of the treatment duration: as already observed the term  $\sigma_f$  remains almost constant in the time range between 30 sec up to 5 min. Times shorter than 30 sec are not investigable due to the non-uniformity of the superficial damaging for so brief intervals. Similar results were obtained for the y direction. Thus, the line tension does not change at least after a 30 sec long treatment. On the other hand, the curvature radius changes: this is simply due to the substrate thickness reduction.

Another series of GaAs were treated for 1 min with different sandpapers (from P180 to P4000), corresponding to different grain dimensions. The GaAs piece, damaged for 1 min with P1200, was also considered in this analysis. Figure B.1.2 shows the line tension of the superficial layer, as derived according with equations B.1.2 and B.1.3, and the x curvature radius (inset) as a function of the grain dimension. At variance with the time dependence, the line tension trend is now not constant. The analyses above suggest the possibility to achieve a desired curvature radius by means of a careful combination of crystal thickness and surface damage characteristics.

## B.2. Model of strain formation in surface treated crystals

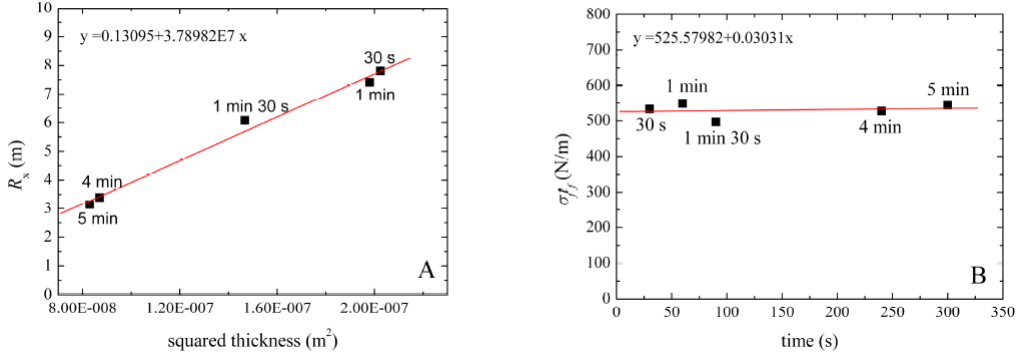


Figure B.1.1: GaAs WT3 pieces undergone to superficial treatment with sandpaper P1200 but different time long. Panel A: x curvature radii as a function of the squared thickness. Panel B: line tension of the superficial layer as a function of the treatment duration. The straight lines and the equations above come out from linear fittings.

## B.2 Model of strain formation in surface treated crystals

In order to understand the physical mechanism at the origin of the compressive strain that causes the bending of crystals in surface damaged treatment, we performed a Transmission Electron Microscopy characterization in cross section mode of several GaAs samples (100) oriented. A GaAs, treated with sandpaper P400 for 10 minutes, with a radius of curvature  $R = 2.8$  m is analyzed by High Angle Annular Dark Field (HAADF) mode and in scanning mode (STEM), Fig. B.2.1: higher contrast correspond to heavier elements in the sample.

TEM images in Fig. B.2.1 show a dense dislocation network with dislocation lines inclined at  $57^\circ$  with respect to the sample (001) surface. The sample orientation and the dislocation line angle demonstrate that the dislocations glide along on (111) type planes perpendicular to the image plane; the dislocation penetrates up to several  $\mu\text{m}$  in the substrate. In face centered cubic crystals, such as GaAs, Ge, Si, an easy glide systems is based on the glide of perfect dislocation with Burgers vector of type  $b = 1/2[110]$  on (111) type plane. In fcc crystals the majority of dislocations are of the type  $b = 1/2[110]$ , since they are perfect (the Burgers vector coincides with a lattice vector) and have the lowest elastic energy among all possible perfect dislocations. From Fig. B.2.1 we can estimate a linear dislocation density  $\rho \sim 15 \cdot 10^6 \text{m}^{-1}$  and a penetration depth  $t = 2\mu\text{m}$ .

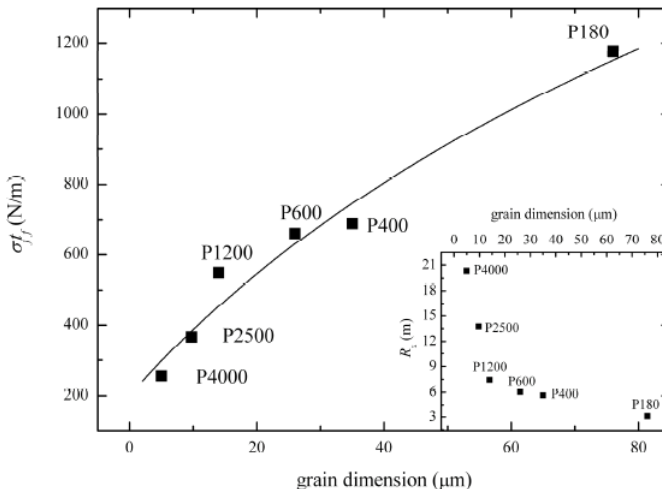


Figure B.1.2: Line tension  $\sigma_f t_f$  of the superficial layer as a function of the grain dimension for GaAs pieces undergone to superficial treatments 1 min long with different sandpapers. The line is a guide for the eyes. Inset: x curvature radii as a function of the sandpaper grain dimension.

### B.3 Mechanism of dislocation formation

We propose here a possible mechanism of the strain formation due to the surface damage of the crystal. We assume that the effect of sand paper grain is similar to the indentation of a tip in the material, as sketched in Fig. B.3.1 .

The effect of the tip is to introduce dislocation loops of perfect  $a/2[110]$  dislocations gliding on the (111) and  $(-1 -1 1)$  planes perpendicular to the plane of the image. Due to the dislocation movement the part of the crystal between the (111) and  $(-1 -1 1)$  planes moves one lattice step downward. Note that the components of the Burgers vectors perpendicular to the surface at the (111) and  $(-1 -1 1)$  plane are of opposite sign. The dislocation loops move up to a depth  $t_f$  below the surface leaving a network of dislocations lines perpendicular to the plane of the figure at a depth  $t_f$ . The resulting Burgers vector  $\mathbf{b}$  coincides with a vector of the direct space:

$$\mathbf{b} = \frac{a}{2}[011] \quad (\text{B.3.1})$$

With  $a$  the lattice parameter. The component of the Burgers vector  $\mathbf{b}$  parallel to the sample surface is given by:

$$b^\perp = \frac{a}{2} \quad (\text{B.3.2})$$



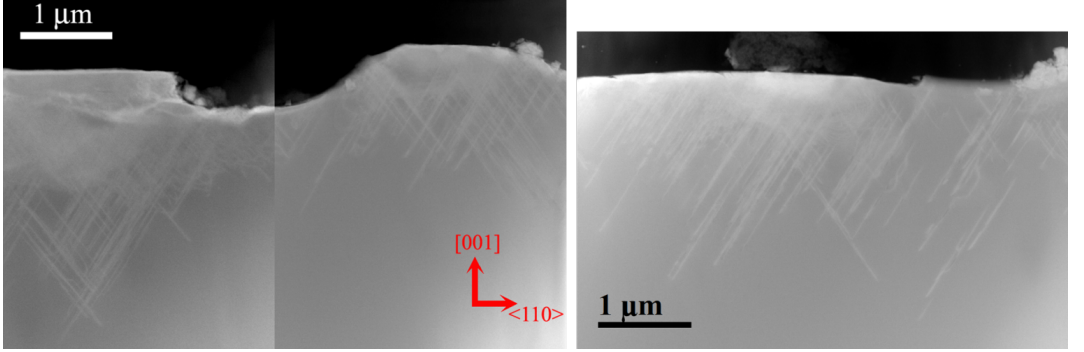


Figure B.2.1: High angle annular dark field (HAADF) images in STEM mode.

where  $a = 5.6535\text{\AA}$  for GaAs. We now have a network of dislocation with linear density  $\rho \sim 15 \cdot 10^6 \text{m}^{-1}$  placed at a depth  $t = 2\mu\text{m}$  between the damaged surface and the bulk of the GaAs crystal, all having the same value of the perpendicular component  $b^\perp$ . We may conclude that the damaged surface layer is under a compressive strain  $f$  given by the lattice mismatch induced by the dislocation network:

$$strain = f = \rho \cdot b^\perp = \rho \cdot \frac{a}{2} \quad (\text{B.3.3})$$

If we consider a dislocation density (from TEM)  $\rho = 2 \cdot 10^7 \text{m}^{-1}$ ,  $a = 5.6535\text{\AA}$  we obtain a strain value of  $5.6 \cdot 10^{-3}$ . We may compare this value with that obtained from the crystal curvature. From equation B.1.3 for a biaxial stress, with  $T = 0.36\text{mm}$  and  $R = 2.8 \text{m}$ , we obtain  $f \cdot t = 7.71e^{-9}$ . Considering a penetration measured from TEM images, we obtain a strain value  $f = 3.9 \cdot 10^{-3}$  in reasonable agreement with observations and therefore validating our preliminary model.

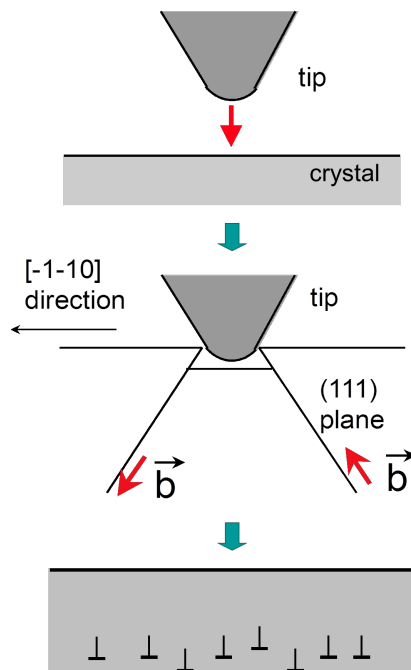


Figure B.3.1: Mechanism of dislocation introduction by means of indentation by a tip.

# Appendix C

## Experimental set up

### C.1 ANKA Synchrotron radiation facility

During the measurements at ANKA Synchrotron Radiation Facility at beamline PDIFF it was possible to characterize the Integrated intensity  $I_{\text{int}}$  of some Si and GaAs flat and bent crystals, realized with the lapping process, in Laue diffraction geometry.

The PDIFF beamline is dedicated to diffraction experiments on bulk polycrystalline materials, with the emphasis on in-situ investigations. Additional experimental facilities enable high-resolution powder diffraction, residual stress and texture measurements. The overall layout of the beamline is shown in the Figure C.1.1 .

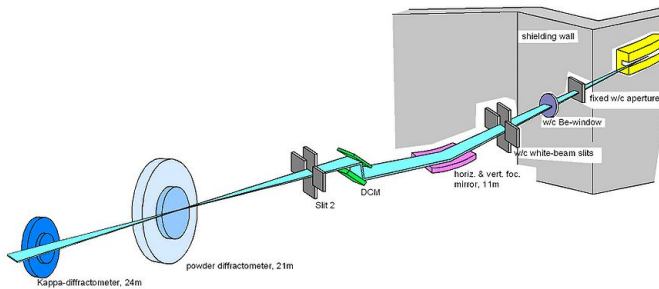


Figure C.1.1: Schematic layout of the beamline PDIFF showing the main components.

It consists of two main functional parts: the beam optics and a small 4-circle Kappa diffractometer for high angular resolution studies.

The main parameters of the beamline optics are summarized:

Energy/ Wavelength range:  $6 \div 20\text{keV}$  /  $2.1 \div 0.62\text{\AA}$

Energy resolution  $[\Delta E/E] \approx 2E-4$  (at 10 keV)

Source: 1.5 T Bending magnet ( $EC = 6 \text{ keV}$ )

Optics: • Upward reflecting Rh-coated cylindrical mirror (fixed horiz. focus, variable vert. focus), • Si111 double-crystal monochromator

Flux at 1st sample position  $\approx 10E+9$  photons/(s x 0.1%bw) in  $1 \text{ mm}^2$  @ 10 keV

Typical beam cross section (fwhm): • 0.6mm (H) x 0.3mm (V) (focused) at the 3-circle instrument, • 2mm (H) x 0.3mm (V) (focused) at the 4-circle instrument

Experimental setup/ sample environment: • 3-circle Powder Diffractometer with 2D and 1D detectors; • 4-circle Kappa Diffractometer with 3 sample orientation circles ( $\Omega$ ,  $K$ ,  $\Phi$ ) and detector circle ( $2\theta$ ) equipped with Ge111-analyser

Experimental setup / detectors: • Princeton Instruments 4Mpx CCD-camera, • INEL  $90^\circ$  linear detector, • scintillation detectors with optionally analyser, • slits or Soller collimators for variable resolution/throughput.

Data Acquisition Software/ Data treatment/ Databases /Evaluation: • SPEC instrument control, • ImageJ, • Area Diffraction Machine, • FIT2D, ICSD, PDF-2-search-match, TOPAS, FullProf, • Crystallographica

The smaller of the two diffractometers on PDIFF is a 4-circle Kappa-geometry instrument with an additional 2-circle stage for an analyser/detector combination (Fig. C.1.2).

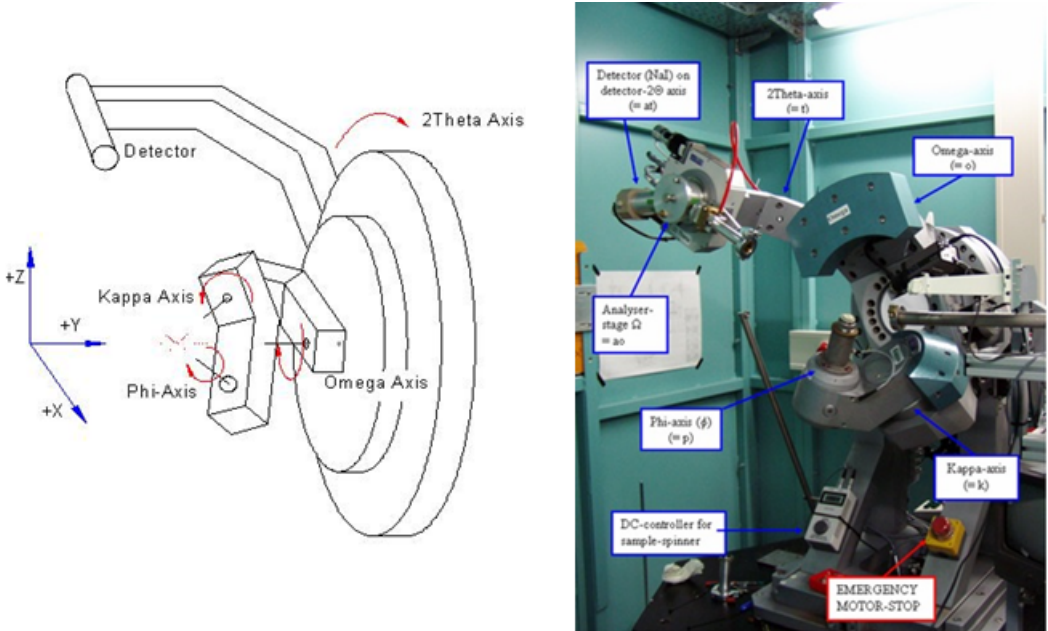


Figure C.1.2: Schematic of a 4-circle diffractometer.

The experiment consists in the measurement of the rocking curves in Laue

transmission geometry of several Si and GaAs (100) flat and bent crystals at energies 19 and 22.5 keV. Is possible to set the energy changing the optics.

## C.2 Hard X ray Facility, ILL

The experimental set-up is designed in order to focalize on the detector all the diffracted beam coming from a flat perfect crystals. This is a geometrical effect realized where the distance sample-source is the same that distance of sample-detector ( $L$  in Fig. C.2.1). Two different line are available: the first called *Low resolution line* where the distance  $2L$  is 7.2 m with a standard resolution of about 0.17 arcsec and the other called *High resolution line*, where  $2L$  is 12 meters and the standard resolution is 6 arcsec. All the measurements reported in this work are performed in the high resolution line.

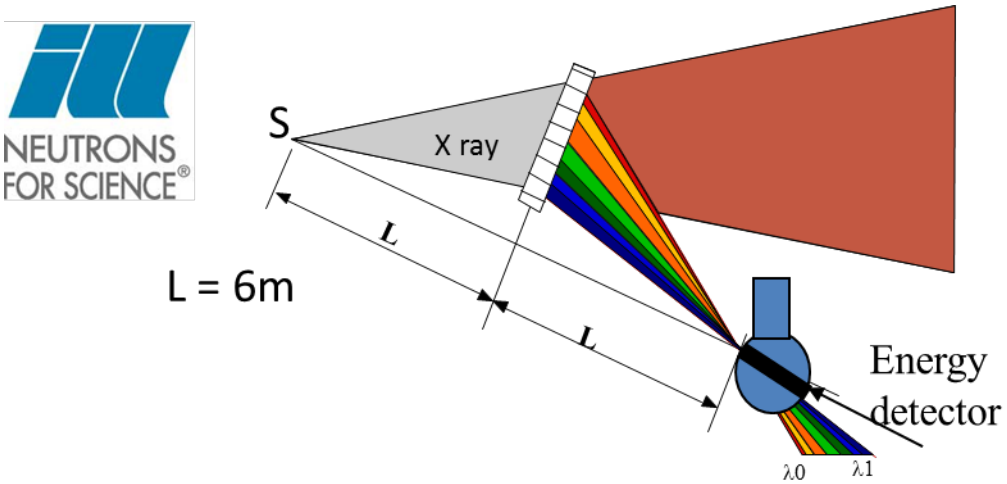


Figure C.2.1: Scheme of the diffraction measurement. The distance between source and the sample is the same distance between sample and detector. In this configuration all the diffracted beam are focalized on the detector.

The main characteristic of the facility are summarized here:

Energy range : from 80 keV to 450 keV (0.15 to 0.03 Å)

Maximum intensity : 1.5 mA (at 450 keV)

Source: W tube

Generator focus :  $1 \times 1 \text{ mm}^2$

Focus collimation : down to 0.5 mm diameter

Max beam size (at sample position) :  $80 \times 40 \text{ mm}^2$

Bragg angles :  $< 3$  degrees (0.5 ÷ 1 degree typically)

Lattice tilt max sensitivity : 6 arcsec ( $2 L = 12 \text{ m}$ )

XRII (X-Ray Image Intensifier) + cooled CCD camera (16 or 32 bits):

- Spatial resolution : about 0.35 mm;
- Time acquisition : typically few seconds

As an example Fig. C.2.2 panel A shows the image of a flat perfect Si (100) crystal; it appears as a very narrow line. The sum for column of pixel give the diffraction profile as in Fig. C.2.2 panel B the diffraction profile of perfect crystal is reported. The FWHM is calculated and for a perfect crystals it can be compared with the experimental resolution of 18 arcsec, so the value of FWHM is a directly estimation of the crystal perfection. In this configuration, a slightly deformation of the crystals lattice as mosaicity, bending ecc.. can be immediately see in the changing of the diffracting images. Moreover, studying the diffracted images also topographic information can be obtained, for example is possible to evaluate if the bending is uniform in the whole crystals, Fig. C.2.2 panel C. The integrated intensity  $I_{int}$  is the integral under the calculated diffraction profile.

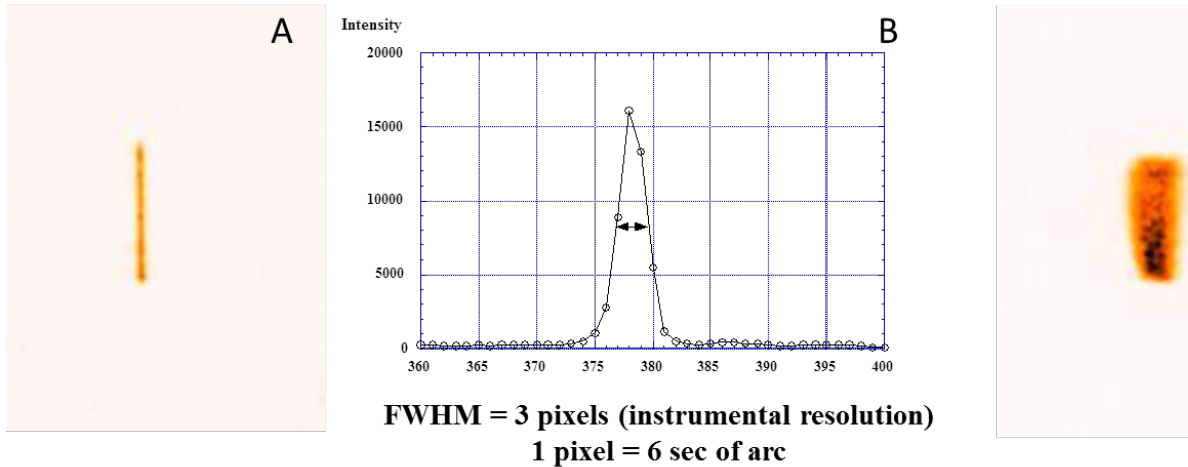


Figure C.2.2: panel A: image of a flat perfect Si crystal. Panel B: diffraction profile given by the sum for column of the pixels of the diffracting image. The FWHM is about 18 arcsec that correspond to the instrumental resolution. Panel C: image of a bent lapped Si crystal.

The energy of the diffracted beam is calculated by geometrical considerations.

# Bibliography

- Abrosimov, N. V. (2005). *Exp. Astron.* **20**,1,185-194.
- Adler, L. P., Weinberg, I. N., Bradbury, M. S., Levine, E. A., Lesko, N. M., Geisinger, K. R., Berg, W. A. & Freimanis, R. I. (2003). *The Breast J.* **9**, 163–166. doi: 10.1046/j.
- Alianelli, L., del Rio, M. S. & Felici, R. (2004). *J. App. Cryst.* **37**, 732–742.
- Authier A. (2001). *Dynamical theory of X-ray diffraction*. IUCr 11.
- Authier A., Balibar F. & Epelboin Y. (1970). *Phis. Stat. Sol.* **41**, 225.
- Authier, A., Lagomarsino, S. & Tanner, B. K. (1996). *X- ray and neutron Dynamical diffraction. Theory and Applications*. Plenum Press, NATO ASI Series, New York and London.
- Authier, A. & Malgrange, C. (1998). *Acta Cryst.* **A54**, 806-819.
- Barrière, N., Guidi, V., Bellucci, V., Camattari, R., Buslaps, T., Rousselle, J., Roudil, G., Arnaud, F. X., Bastie P. & Natalucci, L., (2010). *J. of App. Cryst.* **43**, 1519–1521.
- Barrière, N., Rousselle, J., von Ballmoos, P., Abrosimov, N. V., Courtois, P., Bastie, P., Camus, T., Jentschel, M., Kurlov, N. V., Natalucci, L., Roudil, G., Brejnholt, N. F. & Serre, D. (2009). *J. Appl. Cryst.* **42**, 834-845.
- Bellucci, V., Camattari, R., Guidi, V., Neri, N. & Barriere, N. (2011). *Exp. Astron.* **31**, 45-58.
- Bonnini, E. (2012). *X-ray diffraction in Laue geometry in bent crystals*. Master Degree, University of Parma, Italy.
- Bonnini, E., Buffagni, E., Zappettini, A., Ferrari, C. & Doyle, S. (2015). *J. of Appl. Cryst.* **48**, 666-671.
- Borrmann, G. (1950). *Z. Phys.* **127**, 297-323.

- Bragg, W. H. & Bragg, W. L. (1913). *Proc. of the Royal Society of London.* **88**, 428-438.
- Buffagni E., Ferrari C., Rossi F., Marchini L. & Zappettini A. (2011). *Proc. SPIE 8147*. 81471H-1-9.
- Buffagni, E., Ferrari, C., Rossi, F., Marchini, L. & Zappettini, A. (2012). *Opt. Eng.* **51**, 056501.
- Buffagni, E., Bonnini, E., Zappettini, A., Guadalupi, G. M., Rossi, F. & Ferrari, C., (2013). *Proc. SPIE 8861*, 88610E.
- Camattari, R., Paternò, G., Battelli, A., Bellucci, V., Bastie B. & Guidi, V. (2014). *J. Appl. Cryst.* **47**, 799-802.
- Carassiti, V., Dalpiaz, P., Guidi, V., Mazzolari, A. & Melchiorri, M. (2010). *Rev. Sci. Instrum.* **81**, 066106.
- Chandra, R. (1999). *Introductory physics of nuclear medicine*. Third Edition, Lea and Febinger Press, Philadelphia.
- Courtois, P., Amati, L., Caroli, E., Franceschini, T., Landini, G., Silvestri, S. & Stephen, J. (2005). *Exp. Astron.* **20**, 241-251.
- Darwin, C. G. (1914). *Philos. Mag. Series.* **27**,158.
- Erola, E., Eteläniemi, V., Suortti, P., Pattison, P. & Thomlinson, W. (1990). *J. Appl. Cryst.* **23**, 35-42.
- Ewald, P.P., (1921). *Ann. Phys.*
- Fahnlne, D. E., Masters, C. B. & Salamon, N. J. (1991). *J. Vac. Sci. Technol.* **A9**, 2483-2487.
- Ferrari, C., Zanotti, L., Zappettini, A. & Arumainathan, S.(2008). *Proc. of SPIE 7077*, 70770O-1-11.
- Ferrari, C., Buffagni, E., Bonnini, E. & Korytar, D. (2013). *J. App. Cryst.* **46**, 1576-1581.
- Ferrari, C., Buffagni, E., Marchini, L. & Zappettini, A. (2012). *Optical Eng.* **51**, doi:046501-1-046501-5.
- Ferrari, C., Buffagni, E., Bonnini, E. & Zappettini, A. (2014). *Opt. Eng.* **53**, 047104.



## Bibliography

---

- Ferrari, C., Buffagni, E. & Rossi, F. (2013). *Strain and composition determination in semiconducting heterostructures by high resolution X-ray diffraction*. Edited Lamberti, C. ISBN: 978-0-444-53099-8
- Finot, M., Blech, I. A., Suresh, S. & Fujimoto, H. (1997). *J. Appl. Phys.* **81**, 3457.
- Frey, F. (1974). *Nucl. Instrum. Methods* **125**, 9–17.
- Frontera, F., Pisa, A., de Chiara, P., Loffredo, G., Pellicciotta, D., Carassiti, V., Evangelisti, F., Andersen, K., Courtois, P., Hamelin, B., Amati, L., Landini, G., Franceschini, T. & Silvestri, S. (2005). *Proc. SPIE 5900*. doi:10.1117/12.621116.
- Frontera, F., Virgilli, E., Liccardo, V., Valsan, V., Carassiti, V., Evangelisti, F., Squerzanti, S., Risaliti, G. (2012). *J. Phys.: Conf. Ser.* **355**, 012005.
- Frontera, F. & von Ballmoos, P. (2010). *X-Ray Opt. and Instr.* **2010**, ID 215375.
- Guidi, V., Barrière, N., Bellucci, V., Camattari, R. & Neri, I. (2011). *Proc. SPIE 8147*. doi:10.1117/12.895334.
- Guidi, V., Bellucci, V., Camattari, R. & Neri, I. (2013). *Nucl. Instr. and Meth. in Phys. Res. Se. B.* **309**, 249-253.
- Halloin, H. & Bastie, P. (2005). *Exp. Astron.* **20**, 151-170.
- Hirsch, P. B. (1951). *Acta Cryst.* **5**, 176.
- Janáček, Z., Kubéna, J. & Holý, V. (1978). *Phys. Stat. Sol.* **A50**, 285-291.
- Janssen, G. C. A. M., Abdalla, M. M., Van Keulen, F., Pujada, B. R. & van Venrooy, B. (2009). *Thin Solid Films* 517, 1858-1867.
- Kalman, Z. H. & Weissmann, S. (1979). *J. Appl. Cryst.* **12**, 209-220.
- Kalman, Z. H. & Weissmann, S. (1983). *J. Appl. Cryst.* **16**, 295-303.
- Kato N. (1964). *J. Phys. Soc. Jpn.* **19**, 67-71, 971-985.
- Keitel, S., Malgrange, C., Niemöller, T. & Schneider, J. R. (1999). *Acta Cryst. A.* **55**,5, 855–863.
- Knödlseeder, J., von Ballmoos, P., Frontera, F., Bazzano, A., Christensen, F., Hernanz, M. & Wunderer, C. (2009). *Exp. Astron.* **23**, 121-128.
- Knödlseeder, J. (2006). *Proc. SPIE 6266*. doi:10.1117/12.671451.

- Liccardo, V., Virgilli, E., Frontera, F., Valsan, V., Buffagni, E., Ferrari, C., Bonnini, E., Zappettini, A., Guidi, V., Bellucci, V. & Camattari, R. (2014). *Exp. Astron.*, 10.1007/s10686-014-9425-y.
- Loffredo, G., Frontera, Pellicciotta, D., Pisa, A., Carassiti, V., Chiozzi, S., Evangelisti, F., Landi, L., Melchiorri, M. & Squerzanti, S. (2005). *Exp. Astron.* **20**, 413–430.
- Lund, N. (1992). *Exp. Astron.* **2**, 259–273.
- Lund, N. (2005). *Exp. Astron.* **20**, 211–217.
- Malgrange, C. (2002). *Cryst. Res. Technol.* **37**, 654.
- Neri, I., Camattari, R., Bellucci, V., Guidi, V. & Bastie, P. (2013). *J. Appl. Cryst.* **46**, 953–959.
- Penning & Polder (1961). *Philips Res. Rep.* **16**, 419–440.
- Roa, D. E., Smither, R. K., Zhang, X., Nie, K., Shieh, Y. Y., Ramsinghani, N. S., Milne, N., Kuo, J. V., Redpath, J. L., Al-Ghazi, M. S. A. L. & Caligiuri, P. (2005) *Exp. Astron.* **20**, 229–239.
- Smither, R. K., Abu Saleem, K., Roa, D. E., Beno, M. A., von Ballmoos, P. & Skinner, G. K. (2005). *Exp. Astron.* **20**, 201–210.
- Smither, R. K., Abu Saleem, K., Beno, M. A., Kurtz, M., Khounsary, A. & Abrosimov, N. (2005). *Rev. Sci. Instrum.* **76**, 123107-1-19.
- Stoney, G. G. (1990). *Proc. R. Soc. Lond.* **A82**, 172-175.
- Warren, B. E. (1969). *X-ray diffraction*. Dover Publication, New York.
- Virgilli, E., Frontera, F., Rosati, P., Bonnini, E., Buffagni, E., Ferrari, C., Stephen, J.B., Caroli, E., Auricchio, N., Basili, A. & Silvestri, S. (2015). *Exp. Astron.* 10.1007/s10686-015-9490-x.
- Virgilli, V., Frontera, F., Valsan, V., Liccardo, V., Carassiti, V., Squerzanti, S., Statera, M., Chiozzi, S., Evangelisti, F., Caroli, E., Stephen, J., Auricchio, N., Silvestri, S., Basili, A., Cassese, F., Recanatesi, L., Guidi, V., Bellucci, V., Camattari, R., Ferrari, C., Zappettini, A., Buffagni, E., Bonnini, E., Pecora, M., Mottini, S. & Negri, B. (2013). *Proc. SPIE 8861*, 886107.
- Zachariasen, W. H. (1945). *Theory of x-ray diffraction in crystals*. New York: Wiley.